An Analysis of the Inorganic Perovskite, CsPbBr$_3$, as an X-ray Detecting Material

Logan Forth

A dissertation submitted in partial fulfillment

of the requirements for the degree of

Doctor of Philosophy

of

University College London.

Department of Medical Physics and Biomedical Engineering

University College London

August 12, 2021

I, Logan Forth, confirm that the work presented in this thesis is my own. Where information has been derived from other sources, I confirm that this has been indicated in the thesis.

Signed:

Abstract

CsPbBr$_3$ is one perovskite among several that have drawn a large degree of interest for their semi-conductive properties and when twinned with their relatively high atomic number, these make for ideal high energy radiation detectors. Here CsPbBr$_3$ and CsPb(Br:I)$_3$ are synthesised through solution growth methods, then ground and pressed into pellets for the first time, where active device layers are 1 mm thick and pixel contacts of silver or gold are deposited. Furnace melt formation of single crystals is also investigated. Photoluminescence measurements of CsPbBr$_3$ give a bandgap ranging between 2.33–2.40 eV. Perovskite samples are left in an air environment for 300 days before being tested. Radiation sensitivity is measured by exposure to a tungsten target X-ray source operating in a range of 20–100 kV p, and measuring photocurrent generation with a focus on pixel and channel contacts of varying architecture, determining the charge collection efficiency and charge sharing between pixels. X-ray Monte Carlo simulation is developed in tandem to model the energy absorption of the Perovskite, in order to determine optimum operating conditions and assist in device design. Devices are found to exhibit sensitivities in the range of 23–170 μC Gy^{-1} cm^{-2} but low $\mu\tau$ values of $(3.3$–$23) \times 10^{-6}$ cm^2 V^{-1}. A novel lateral pixel design is demonstrated to show indirect X-ray energy contrast. X-ray images are acquired through lateral translation

of perovskite pixels, where sub-mm details are resolved through the employment of contact guarding.

Impact Statement

The direct detection of X-rays through semiconducting materials is a field of rapidly increasing study with application to the sector of radiation detection for fields such as radiation imaging, radiation protection and nuclear security. Current direct detectors are limited by their low interaction rate with X-rays, while new perovskite materials such as $CsPbBr_3$ offer impressive high absorption rates without sacrificing electronic properties. Properly exploiting the advantages of these materials requires optimisation for multiple factors; the synthesis methodology, mixtures with dopants or alternative crystal structures, the material processing into functional devices, such as the architecture and electronic contact materials, and finally the operating conditions such as the bias voltage and type of radiation dose and energy.

Presented in this thesis are results pertaining to these factors, striving to find useful combinations of synthesis, contacts and readout methods. In particular, the use of pressed powder perovskite, moving entirely away from the popular concept of a single crystal, to search for a cheap but effective method of synthesis. In contrast, single crystal devices are found to be difficult to reliably produce in as cheap or scalable of a method through furnace melting and cooling. The pressed pellet design offers the advantage of low cost and highly scalable production methods, and results

in this thesis indicate the sensitivity is on par with other perovskite materials under research. However, it is also shown that there is much to be done in optimising the connectivity between local structures within the material. Sensitivity testing is performed for general radiation detection, while X-ray imaging is also achieved with singular pixels translated over objects. The devices perform even under long term air exposure, which is a frequent problem with these devices, and with a non-ideal testing apparatus.

Acknowledgements

Firstly and foremost, I would like to thank my supervisors, Professor Robert Speller and Doctor Robert Moss, for their guidance, support and wisdom in helping me to steer this project to finalisation. I would never have been able to muster the commitment and devotion to finishing this project without their continued and never faltering encouragement. I would also like to thank the collaborative efforts from Professor Kwang Leong Choy, and Doctor Mingqing Wang, without which much of this project would not have been possible. In addition, I must acknowledge the assistance provided by Professor Paul Sellin for further collaboration and also his research group for providing camaraderie at multiple long distance conferences. Furthermore, I would like to wholeheartedly thank the friends in my department I made over coffee mornings, in particular Ian and Savanna, who have helped quell my constant fears and worries over every little detail of my work.

I am eternally grateful to my girlfriend, Cristina, who's constant care and kindness for the final years of my PhD have kept my spirits buoyed above the ocean of failure. Without your love I would never have come to this point. I am also humbly indebted to the support and companionship from my close circle of friends, Ardavan, Dylan, Savannah and Hannah, through whom I've found unending support

and familiarity. Without you I never would have come back. In addition I must give thanks to the UCL SFFS society, of whom I was a committed member, without which my time studying at UCL would have been entirely uneventful, gifting me memories that I shall retain for life, and many of you have become long term friends. Without SFFS I never would have come to meet any of the aforementioned.

Contents

7 Discussion and Conclusions   **188**

Bibliography   **203**

8 Appendix   **217**

List of Figures

Abbreviations

$\mu\tau$ $\mu\tau$-product

AOR Area of Response

CCD Charge Coupled Device

CCE Charge Collection Efficiency

CMOS Complementary Metal Oxide Semiconductor

CS Compton Scatter

CZT Cadmium Zinc Telluride

ESD Electro Static Discharge

FWHM Full Width at Half Maximum

GEANT4 GEometry ANd Tracking 4

LCC Leadless Chip Carriers

MC Monte Carlo

PL Photoluminescence Spectroscopy

PMT Photo-multiplier Tube

SEM Scanning Electron Microscopy

TEM Transmission Electron Microscopy

TL Thermoluminescent

TLD Thermoluminescence Dosimeter

XRD X-ray Diffraction

XRF X-ray Fluorescence

Classifications

ARB1 Altered Ratio Batch 1

BB1 Base Batch 1

BB2 Base Batch 2

BB3 Base Batch 3

IB1 Iodine Batch 1

IB2 Iodine Batch 2

TB1 Test Batch 1

Thesis Outline

In this thesis, the use of perovskite material $CsPbBr_3$ as an X-ray detective medium will be evaluated. This work aims to explore the use of pressed pellets as a novel method for forming the detective layer, in contrast to the usual methods of single crystal growth, and use this as an argument for their cost effectiveness and scalability. The work will take advantage of this unique synthesis method to form proof-of-concept lateral pixel based devices. The performance of devices synthesised in this way will be simulated and evaluated to display their characteristics, after which advantages, disadvantages and further work can be discussed.

This will start with chapter 2, a description of the involved physics processes in this research, and then identify the existing research on perovskite photodetectors and X-ray detectors. Current research will be reviewed in it's application to the current work in order to determine novel methods.

In chapter 3 simulation techniques for X-ray dose and spectrum determination will be initially analysed and developed, for the purpose of application towards understanding X-ray responses for the the perovskite devices developed later. Monte Carlo (MC) techniques will be employed to simulate the X-ray dose and spectro-

scopic output of the X-ray systems. Thermoluminescent dosimeters and ion chamber measurements will be made to validate the simulation dose estimation, and CdTe X-ray spectrometry will be used to validate the spectroscopic simulation.

Chapter 4 will then discuss the synthesis techniques to be used for creating the $CsPbBr_3$ samples, and cover the findings from their practicality. Designs for ideal and opportune perovskite devices designs, and the methods to achieve them, will be proposed, and the advantages and disadvantages discussed.

The simulation work will then be applied to the perovskite devices, in chapter 5, to analyse the radiation induced charge and the charge carrier local spread from ionisation. Further validation of the dose simulation will be made with ion chamber experiments to ensure no divergence from reality is incurred.

In chapter 6, the X-ray responses of these perovskite devices will be presented and analysed, with comparisons made between their photocurrent and anticipated photocurrent from simulations. The methods for this photocurrent analysis will first be explained, followed by examples of it's application. The overall response of devices to varying X-ray spectrum energy, intensity and bias voltage will be tested and discussed. Furthermore, peculiarity in devices responses will be highlighted and causes suggested. A proof-of-concept channelled perovskite device will be demonstrated. X-ray imaging will be conducted through lateral translation of devices behind samples to demonstrate the detective capability of the perovskite samples.

Finally, the research implications of the work will be concluded on in chapter 7. Here, the opportunities for future work to develop this field of investigation will

be proposed and the novel aspects of the work will be emphasised. It will be shown that the devices function to detect X-rays of 20-120 kVp at a large range of bias voltages and radiation dose rate, however that their charge collective efficiency is reduced in comparison with typical single crystal devices.

Introduction and Background

When aiming to detect X-rays and other high energy photons, one's initial concern is the method of detection, whether to use scintillation materials and hence detect the light produced, or to directly measure the X-ray stimulated response in a radiation sensitive material. The former has traditionally been the most convenient methodology employed in the early uses of X-ray detection and imaging. Since their discovery in 1895 by Wilhelm Röentgen[1], X-rays were detected indirectly through a multitude of fluorescence mechanisms. However, from the dawn of the digital revolution, a widespread interest in developing direct detectors of high energy photons has emerged and increased to an equivalent, if not greater, extent than traditional scintillation methods.

Scintillation detection of radiation works through the interaction of high energy photons with a material creating charged particles that then, upon decay of these particles back to the ground state, emits photons in the visible or infrared range. These photons can be captured by a conventional imaging film or photodetector and read out to infer the locations of more or less intense radiation fluence and thus form an image.

A direct radiation detector, on the other hand, functions by measuring the effects of ionisation of atoms within the medium that the radiation is interacting with. This mostly involves the collection and quantification of free charge carriers, electrons and holes, generated in a semiconducting material in response to ionisation and radiation.

Scintillation techniques rely on multiple stringent factors such as conversion efficiencies of the scintillating medium, blurring from the transport of visible photons to the detector and the relatively large thickness of the scintillating medium. Recent advancement in scintillation techniques has mostly ridden off the back of the development of visible light imaging methods such as silicon based Charge Coupled Devices (CCDs), Complementary Metal Oxide Semiconductors (CMOSs) detection devices and Photo-multiplier Tubes (PMTs). However, scintillation techniques continue to suffer from certain disadvantages, such as the loss of photon information, i.e. the energy and direction, positional resolution limits from photon and charge point spread functions, and the radiation damage vulnerability of modern visible photon detectors[2, 3, 4].

In contrast, direct radiation detectors have room for improvement with respect to their scintillator based counterparts. First developed in the 1970s using silicon as the detection medium, spatial resolution and sensitivity were poor, while the possibility of energy resolution became a primary advantage. Recent advances have seen the use of many more heavy element based detectors, starting from Selenium and moving up to Cadmium Telluride and Cadmium Zinc Telluride, all riding off the exploitation of these materials' semi-conductive properties.

This has led to the current era in radiation detection where direct detection materials are attracting a large degree of research interest as their use becomes more widespread and begin to show advantages over conventional scintillation techniques. Among these interesting materials sits the recently popularised perovskite material Caesium Lead Tri-Bromide ($CsPbBr_3$), attracting research initially in the field of photovoltaic cells, its high radiation attenuation properties make it suitable for radiation detection studies.

2.1 Radiation Detection

Photons of energies greater than $1\,keV$ are typically considered to be either an X-ray or γ-ray. These photons interact with matter primarily through three mechanisms;

- Photoelectric Absorption

- Compton Scattering

- Pair Production

The probability of each mechanism depends on the energy of the photons and atomic number of the matter with which it interacts. This is referred to as the cross-section of interaction.

Photoelectric absorption is characterised by the full absorption of a photon by a bound electron in an atomic shell. This will only happen if the absorbed photons energy, $h\nu$, is great enough to free the electron from the atom to which it is bound, or at least to an empty higher energy state, as the Pauli exclusion principle forbids

it from elevating to a higher energy state if that state is already filled by another electron. If the initial photon had energy in excess of the binding energy of the electron to the orbital, that energy is then transferred to the kinetic energy of the emitted electron, also known as a photoelectron. This form of interaction is more prevalent the lower the energy of the X-ray, beginning from as low as 13.6 eV for the binding energy of the singular electron around a hydrogen atom, up to 115 keV for the binding energy of the inner most electron of Uranium (or higher for synthetic elements).

Compton scattering is the process of interaction between an electron and a high energy photon (relative to the binding energy of the electron) where the photon is not completely absorbed. Instead, through the interaction, some energy is transferred to the electron, and some is retained by the photon. The energy retained by the photon, $E_{\gamma'}$, is determined by the scattering angle, θ, and the initial energy of the photon, E_γ.

$$E_{\gamma'} = \frac{E_\gamma}{1 + (E_\gamma/m_e c^2)(1 - cos(\theta)))} \tag{2.1}$$

The energy transferred to the electron is equal to that lost by the photon, or $E_\gamma - E_{\gamma'}$. This form of photon interaction is most prominent at high X-ray energies and over the broad spectrum of γ-ray energies.

Pair production is a process only reachable with photons of much higher energies than typical X-rays. The interaction in this process eliminates the photon entirely and spontaneously creates an electron and positron pair. For this to hap-

pen, the energy of the photon must be greater than the sum of the rest mass of the electron and positron, which are each $511\,\text{keV}$, so $1.022\,\text{MeV}$. Also, the interaction must happen near an atomic nucleus, as this receives a small amount of recoil energy to ensure momentum is conserved. The energy imparted to the nucleus can be considered negligible for most cases, so the energy transferred to the electron positron pair through this interaction is $E_{pp} = (h\nu - 2m_ec^2)$. Since the minimum energy required for this interaction is greater than $1\,\text{MeV}$, it is mostly irrelevant to modern X-ray imaging, however this process is involved when considering γ-ray beams in radiotherapeutic treatment or nuclear engineering.

Due to the nature of their interaction, an X-ray beam will travel through a material and be absorbed following an exponential decay as:

$$I = I_0 e^{-L\mu} \tag{2.2}$$

where I is the final beam intensity, I_0 is the initial beam intensity, L is the length of material through which the beam travels and μ is the mass attenuation coefficient associated with that particular material and density. μ depends upon multiple factors, primarily the atomic number, Z, the density of the material, the energy of the incident photon, and thresholds associated with the energy of ionisation for electrons bound to atoms in the material, particularly the innermost shell, the K-shell. With knowledge of these factors it is possible to calculate the distribution of photon absorption within a material, however, it is often much simpler to utilise Monte Carlo (MC) modelling, which probabilistically calculates the interactions of each

individual photon to create a simulated distribution.

When considering X-ray detectors for modern functions, most are concerned with measuring the effects arising from the photoelectric effect, as this is the dominant interaction at medically and industrially relevant energies, with some consideration being given to Compton scattering.

2.2   Semiconductors

Here, the functionality of a photodetector will be described, where photodetector refers to any device designed to measure the intensity of photons, including X-rays and γ-rays. Figure 2.1 shows a 2D cross-sectional image of the basic functionality of a semiconducting material for radiation detection. In a direct detection device, a detecting material will have a potential difference, V, applied across it leading to an electric field, E, throughout the bulk of the material, through the use of contacts on either edges of the material with a bias voltage, V_B, and a grounding voltage, V_0, nominally $0\,\text{V}$. An X-ray photon of energy $h\nu$ enters the sensitive material and is photoelectrically absorbed or scattered by a bound electron orbiting an atom at depth D from surface of the material. The electron absorbs the imparted energy of the photon and, if it is great enough, is removed from the lattice site through ionisation. Any energy in excess of the ionisation energy, E_I, is added to that electron's kinetic energy, E_e such that

$$E_e = h\nu - E_I \tag{2.3}$$
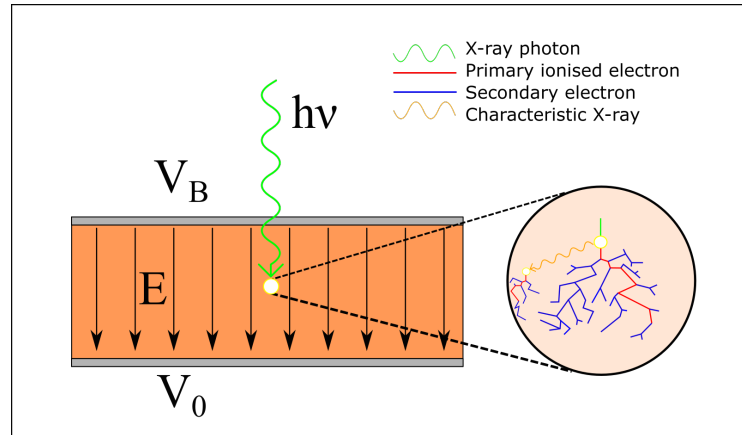
Figure 2.1: A cross-sectional diagram of X-ray ionisation and direct detection in a semi conductor

Through collision amongst the surrounding lattice sites and electron orbitals this ionisation electron will impart its energy onto other neighbouring electrons, either resulting in the further secondary ionisation of electron shells or, failing that, excitation of electrons into higher energy states. The difference is determined by the energy of the primary electron, i.e. if is great enough to ionise or not. This will continue until all of the energy from the primary and secondary ionisation electrons has been dispersed amongst the surrounding material, of the order of $\sim 1\,\text{ps}$. If the kinetic energy imparted by an electron collision is not enough to remove it from the atom site through further ionisation but greater than the bandgap energy E_{BG}, the electron will be moved to the conduction band. This process results in a 'cloud' of electrons elevated to the conduction band with a number of electrons proportional to $\frac{h\nu}{E_{BG}}$.

It is also worth noting, as shown in fig 2.1, that through the ionisation of electron sites, nearby electrons in higher energy states can fill those empty states and in the process emit a photon. The energy of this photon is equivalent to the difference

in energy of the two electron states and is referred to as a characteristic X-ray pho-
ton. Since the electron states surrounding an atomic site each maintain an energy
level set by the properties of the atom, these photons are of a definite energy for
each periodic element, and so can be used to identify elements present in a material.
Furthermore, these characteristic X-ray photons can also work to delocalise the de-
position of charge by transporting some portion of the original X-ray photon energy
relatively far from the initial interaction site, or even out of the material. Hence this
can lead to a blurring or loss of information.

Shown in figure 2.2 is an energy level diagram for a semiconducting material,
the bottom and top showing two bands, the valence band and conduction band, of
electrons respectively with the Fermi energy sitting somewhere between, in what
is known as the bandgap. The Fermi energy can be defined as the level at which,
when a material is at $0\,\text{K}$, all possible electron states below this energy are filled with
electrons, and is referred to as the valence band, and all above are empty, which is
the conduction band. As the temperature increases above $0\,\text{K}$, local excitations of
particles will elevate random electrons to energy levels above this line, though still
in a very low concentration compared with the bulk.

In a conducting material, since an electron excited into a higher state is sur-
rounded by empty states of the same energy it can move freely between these states,
and so move throughout the material unbound to the atomic site it originated from.
Since these energy states are directly above the Fermi level and so energetically
close to the filled lower energy states, there is a relatively large concentration of
electrons filling these energy states at room temperature ($300\,\text{K}$). Connecting a
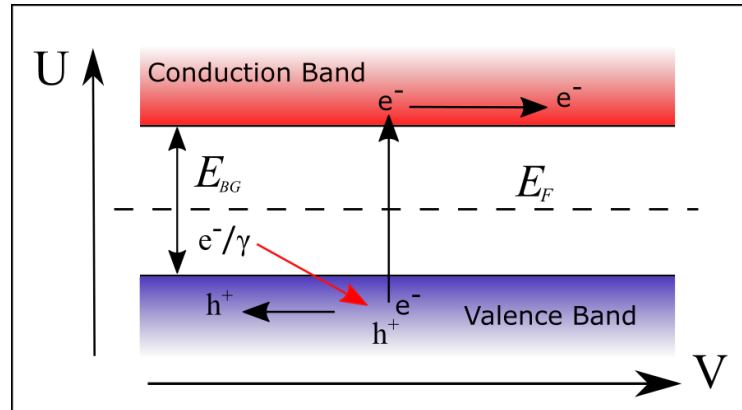
Figure 2.2: A diagram of bandgap energy, E_{BG}, and electron elevation in a semi-conducting material where an electron of energy E is elevated from the valence band (blue) to the conduction band (red) and the separation of the electron hole pair by the potential difference $V^+ - V^-$ applied across the material. The Fermi energy, E_F, is marked with a dashed line.

potential difference to either end of the material can be used to observe a flow of charge that is conducted through the interaction of these free moving higher energy state electrons.

However, in a semiconductor, as shown in figure 2.2, there aren't any electron states available to move into that are close to the Fermi energy. Thus, only a small fraction of electrons manage to thermally elevate themselves into electron states above the bandgap and hence contribute a small conductive current. This, in a photodetecting semiconductor, is the primary contributor to what is known as the dark current.

The dark current of a photodetector, and the reduction of which, is of major interest in the study of photodetection materials. It can be seen that a larger bandgap leads to a lower dark current, as more energy would be needed to be imparted to electrons to bridge the gap before they can be transmitted in a circuit. Also, at lower temperatures, a reduced dark current is observed, as there is less stochastic energy

within the lattice to push electrons into the conduction band.

Thermal energy is not the only mechanism to elevate an electron into a higher energy state. Photoelectric absorption and electron-electron interaction can directly elevate an electron from a state near the top of the valence band, up into the conduction band. For this, the energy of the absorbed photon must be equivalent to or greater than the band gap of the material. As this mechanism elevates a number of electrons proportional to the energy and number of photons interacting with the material, the resultant conduction electrons can be measured in the form of a photocurrent to determine the intensity of incoming photons. The conventional photodetector is based upon this principle.

With promotion to a higher energy level, an electron leaves behind an empty energy state, which is referred to as an electron hole. A hole represents the lack of an electron in an electron rich environment, in such a way that surrounding electrons can move into this hole which in turn leaves a new hole. In this way, the hole can move through the material by the movement of surrounding valence band electrons. This movement of a hole can be modelled as if it were an actual particle, with a positive electronic charge to represent the lack of negative charge that an electron would exert. If a potential difference is applied across the material, not only do the electrodes attract electrons to the positive end, but the holes are also attracted to the negative electrode. In this way, both electrons and holes can contribute to the current through a semiconductor.

Electrons elevated to the conduction band are not permanently promoted to this energy. If, during their transport through the material, they encounter another

electron hole, the electron can drop back down from the conduction band to fill the energy state that the hole occupies. For this to happen, the electron must lose energy equivalent to the band gap, which is emitted in the form of either a new electromagnetic photon or a lattice phonon, vibrational waves in the lattice. This process is referred to as recombination and the frequency of which is directly proportional to the number of holes and free electrons in the material, so a steady state of promotion and demotion is achieved in the lattice. The average time for an electron to exist in the conduction band in a semiconductor before recombination is named the charge carrier lifetime, τ.

It is worth noting that, as in figure 2.2, the Fermi level essentially defaults to the centre of the bandgap. However, with the doping of a semiconductor, the Fermi level can be moved up and down, by creating an uneven balance of holes and electrons in the material. This leads to there existing a dominant charge carrier in the material that outnumbers the other and conducts most of the charge, which can help to suppress recombination effects.

For the duration of an electrons occupation of a state in the conduction band, it can travel through the material in random directions through scattering off of other electrons or lattice sites, and travel linearly with a linear electric field, E. The distance this electron travels under a set electric field is referred to as the electron mobility, μ_e, or in the case of holes, the hole mobility μ_h and more generally for carriers of either type as carrier mobility, μ. The value of μ is variable between all semiconductors and even each instance of a semiconducting material. This is because the electron may be scattered or otherwise find resistance to its movement

from many properties such as the material temperature, the concentration of impurities, lattice defects, grain boundaries and other electrons and holes. This value is typically measured in $\mathrm{cm^2\,V^{-1}\,s^{-1}}$, which is the result of the velocity, $\mathrm{cm\,s^{-1}}$, per electric field, $\mathrm{V\,cm^{-1}}$.

In order for the charge carrier to be extracted it either needs to exist in the conduction band long enough or move fast enough for it to reach the extraction contact before it recombines. A charge carrier that undergoes recombination before it can be extracted represents lost information and a decrease in overall sensitivity of a detector. Because increases in both the average charge carrier lifetime and the mobility of charge carriers within a material are beneficial to the measurement of photocurrent, the product of these two values, the $\mu\tau$-product, is considered a figure of merit in the field of photodetectors as it can be directly related to the quantum efficiency of a detector. The quantum efficiency of a detector is a measure of the ratio of the photons travelling into a detector to the electrons extracted.

To otherwise increase the quantum efficiency, a detection channel can be made thinner to achieve a shorter distance to be crossed before extraction, though this has the downside of thinning the active volume of collection of the semiconductor, absorbing less of the incoming radiation. The electric field can also be increased to push carriers through the material faster, though this can be significantly energy consuming and in complex electronics, lead to circuit breakdown and damage to the components.

2.3 Perovskites for X-ray Detection

The perovskite structure of solids was first recorded through discovery of the mineral $CaTiO_3$ in 1839 [5] in the Ural Mountains of Russia. The label of perovskite, named after the Russian mineralogist Lev Perovski, continued as a classification for any crystal following the same structure as was observed in $CaTiO_3$. $CsPbBr_3$ was first synthesised by Christian Møller in 1958 [6], where he determined it to be of Perovskite structure, and also noted the photoconductivity of it and the related compounds of $CsPbCl_3$ and $CsPbI_3$.

The perovskite structure is explicitly $^{XII}A^{2+}\ ^{VI}B^{4+}\ X_3^{2-}$ [7], where X_3^{2-} is a divalent anion, $^{XII}A^{2+}$ is a divalent cation coordinated by 12 surrounding X^{2-} sites in a cuboctahedral geometry, $^{VI}B^{4+}$ is a tetravalent cation coordinated between 6 X^{2-} sites in an octahedral geometry. Diagrams of the $CsPbBr_3$ lattice structure are shown in Figure 2.3.

The structure of X anions in this arrangement leaves a relatively large opening in every other layer, allowing heavier elements to occupy those sites ($^{XII}A^{2+}$). In $CaTiO_3$, Ca and Ti are relatively large atoms compared to the lighter O atoms [8]. Similarly, in $CsPbBr_3$, the increased atomic radii of the Br atoms allows for even larger and heavier elements to fit into this structure in a stable configuration, such as Pb and Cs.

Notably Cs is the element with the largest known stable atomic radii and Pb is the heaviest stable element which could be selected for the B cation site, which both make for greatly assistive properties to X-ray detection. The large radii of
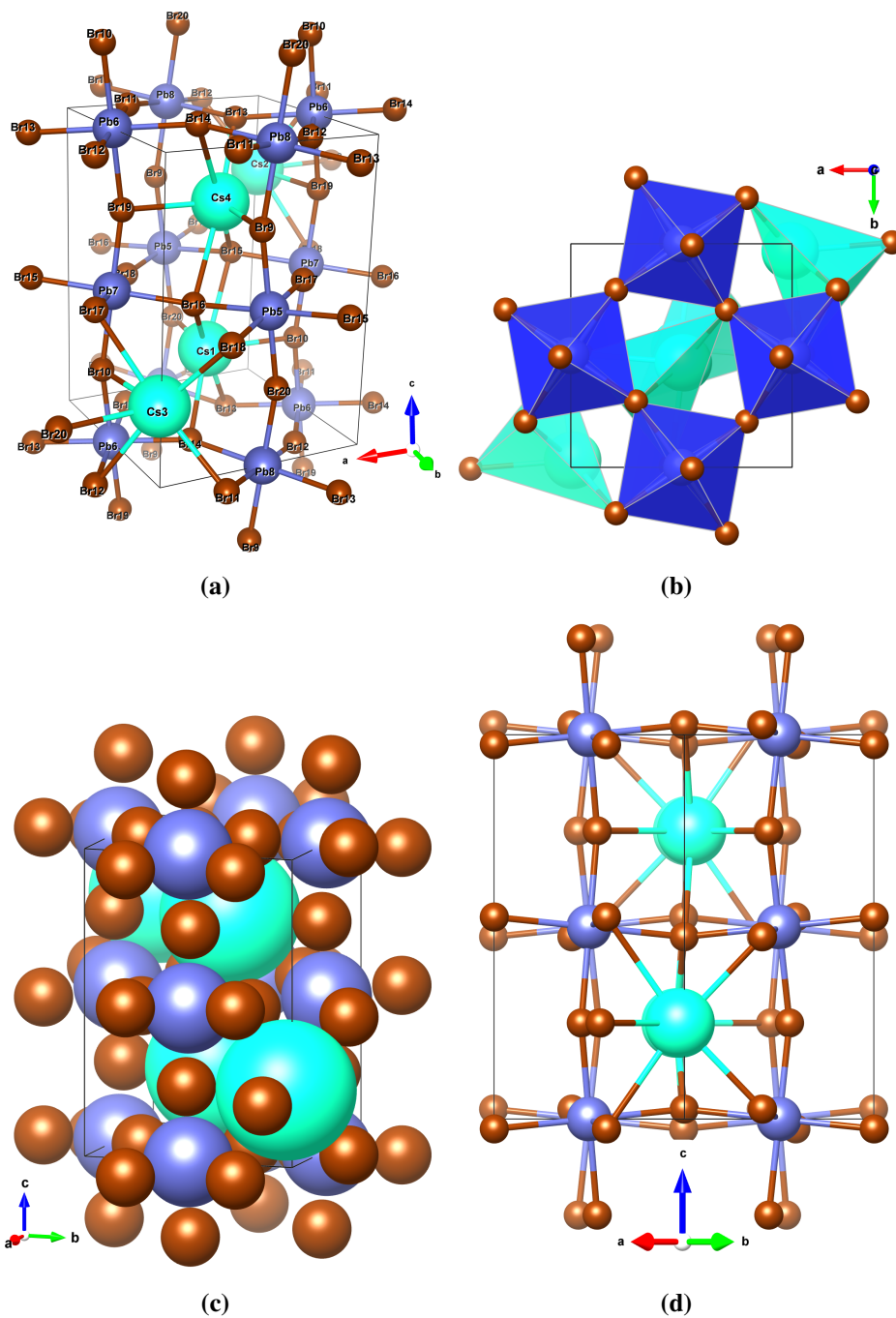
Figure 2.3: Diagrams of the lattice structure of CsPbBr$_3$ drawn in the VESTA software, from various angles and modes of interpretation. Atomic colouring are as follows: Brown - Bromine, Blue - Lead, Cyan - Caesium (a) The unit cell with each atom site labelled and numbered (b) From the bottom, with visible lattice polyhedra of cation sites, showing the rotated bond structure of the anions (c) Space filled spheres of electron bond influence (d) Looking diagonally on to the unit cell, showing the symmetry and deviations within the cell

these elements also leads to a larger unit cell of $0.847\,\text{nm}^3$ [9], about 4 times larger than $CaTiO_3$ at $0.229\,\text{nm}^3$ [8].

$CsPbBr_3$ is an ideal material for X-ray detection due to numerous advantages. Firstly, it is composed of heavy elements, Pb, Cs and even Br, which all have a greater atomic weight than common detection materials such as α-Se and Si. The elements are also well distributed in atomic number Z, with Br at 35, Cs at 55 and Pb at 82. The K-edge energy of X-ray absorption of a material increases with the Z of the atom, as the central electrons are more tightly bound to larger atoms of more protons. Because of this, $CsPbBr_3$ has absorption peaks at $13.3\,\text{keV}$, $35.0\,\text{keV}$ and $84.9\,\text{keV}$[10], which would make a detector built from this material sensitive to absorption spikes that are evenly spread in photon energy across the full range of diagnostic X-ray energies. Along with the high atomic number, the density is $4.55\,\text{g}\,\text{cm}^{-3}$ [9], which is comparable to other materials in the field as α-Se, $(4.39\,\text{g}\,\text{cm}^{-3})$ and Cadmium Zinc Telluride (CZT) $5.81\,\text{g}\,\text{cm}^{-3}$. In addition, $CsPbBr_3$ has been shown to exhibit strong electronic tolerance to defects originating in the lattice[11], which can be a result of improper synthesis methods and through radiation damage. This essentially means that the transport of charge carriers does not suffer greatly from a high concentrations of defects.

The recent interest in Perovskite materials for X-ray detection specifically was aroused in 2015 by Yakunin et al. [12] by synthesising and experimenting with an organic Perovskite, Methyl Ammonium Lead Tri-Iodide ($CH_3NH_3PbI_3$ or $MAPbI_3$). This was building on the already mounting interest garnered from their use in photodetectors and solar energy conversion [13, 14, 15]. This material

showed promise in its high responsivity (1.9×10^4 carriers/Photon at 37 keV) and was even able to capture test X-ray images using xy-translation. Yakunin's group has since shown MAPbI$_3$ to function as an X-ray spectroscopy detector [16], detecting photons at 60 keV with a Full Width at Half Maximum (FWHM) of 21 keV.

Further research in the following years has yielded MAPbI$_3$ detectors with high radiation responses of up to 2.53 µC/Gy$_{air}$/cm^2 [17], further use in X-ray photon counting detection [18, 19] and even fully functional imaging systems[20]. MAPbI$_3$/Br$_3$ has also been shown to function as an X-ray scintillator at cryogenic temperatures [21] with about a 12 % X-ray to photon conversion efficiency.

Though a major drawback has been observed to be the instability, either in air or hermetically sealed. It has been noted to be highly hygroscopic with water vapour in the air and degrades over the course of a few months[12, 22, 23]. Due to this, devices maintained operation for between a few days and several months. Even when hermetically sealed, it was observed to degrade into precursors relatively quickly, making it unsuitable for its desired uses as a solar cell and radiation detecting material. Currently work is proceeding on synthesis with alternate methods [24, 25, 26, 27] or to alter the mixing ratio with other valid elements to Pb that approximate and retain the same composition but alleviates the reactivity with air, such as hybrid perovskites[20].

Amongst the various achievements, MAPbI$_3$ has found use through formation in a pressed pellet device [17] through sintering and hydraulic pressing. Here, hole and electron transport layers were used to improve charge extraction and suppress the dark current. This method, where a pressing pressure of 0.3 GPa was used,

showed remarkable material hardness in comparison with the single crystal MAPbI$_3$ and also good packing density, with only a 9.5 % decrease in material density.

This research shed light upon alternative materials that follow similar compositions and charge transport mechanisms. Organic perovskites such as Methyl-Ammonium Lead Bromide (MAPbBr$_3$) and Formamindium Lead Bromide/Iodide (FAPbBr$_3$/I$_3$) along with inorganic perovskites such as CsPbBr$_3$, CsPbI$_3$ and CsPbCl$_3$[28] and mixtures of the three, have since been investigated for their use in radiation physics.

CsPbBr$_3$ has in particular received attention for exhibiting a much more stable state under air exposure, with less degradation observed than in those containing Methyl-Ammonia [29, 30]. It has also been shown to have a high defect tolerance during formation processes[31], leading to higher quality crystal growth under less stringent conditions. These two advantages together work to enable more reliable cheap synthesis methods such as solution processing.

The research so far into the use of CsPbBr$_3$ as an X-ray detective material has been performed by He et al. and focused on its use as a single crystal, mostly being synthesised through the Bridgman growth method[32]. There are clear advantages to the use of single crystal detections, such as higher carrier mobility and greater structural integrity that increases the response of the material as a radiation detector. However, sintered and pressed CsPbBr$_3$ has advantages in its ease of production and scalability over direct single crystal growth. As shown by Shreshtha et al. [17], devices constructed through this method manage to create strong inter-grain connections and have a packing density close enough to compare with the single

crystal.

Chapter 3: Simulation of X-rays for Device Prediction

3.1   Radiation Absorption

Prior to consideration of the design, functionality and implementation of Perovskite materials into an X-ray imaging device, the radiation absorption properties of a perovskite material along with the surrounding materials in a detector must first be evaluated. This would ensure that it is possible to quantify the performance of the material in converting X-ray photons into measurable charge. Dosimetry and spectroscopy are the fields into which X-ray emission and absorption quantification falls and the methods of which are useful in the consideration of testing a new material for X-ray detective use.

Carrying out the dosimetry of thin and relatively complex devices, however, can be a task highly susceptible to errors, as it requires accurate knowledge of both the incident X-ray photon flux and the spectral distribution of such photons, along with the interaction probabilities this spectrum experiences with the materials in the devices under dosimetric interest.

X-ray energy flux or total dose can be determined via various methods, such as measurement of the ionization in air by the X-ray beam with an ionisation chamber

or a calorimeter. X-ray energy spectra can be measured through approaches such as direct spectrometry or Compton scatter techniques, though not without their inherent difficulties. Interaction probabilities that ultimately lead to energy deposition, or dose, can be worked out through knowledge of the atomic composition of any medium through which the radiation passes. These conditions are difficult to calculate manually, where small deviations of the model from reality lead to large discrepancies in prediction, and thus necessitates the use of computed simulation, most reliably through the Monte Carlo (MC) method of radiation transport modelling.

MC simulation is the most rigorous modern procedure for determining the dose delivered to materials in a radiation dosage environment, as this offers the only way to track and determine the many complex variables that are so much more difficult to observe in experiment[33][34][35].

In order to begin correctly simulating dose deposition to a Perovskite sample, the prediction ability of the model should be validated by comparison with results obtained through use of practical experimentation. For this purpose, Thermoluminescence Dosimeters (TLDs) were used to compare and validate the ability of a predictive MC model to simulate X-ray transport through small volumes of the order of 1 mm.

3.2 Theory

3.2.1 Metrology

In the pursuit of accurate estimations of radiation dose deposition, standardisation of the measurement methods are required to ensure consistency and gen-

eralisation of the data acquired. Metrology refers to the this standardisation and the methods required to achieve it, where taking measurements of radiation dose must first be validated against an agreed calibration standard. Dose deposition of a radiation beam can be observed in many ways through the photoelectric effect, however, the proportionality of the response between radiation energies and intensities is inherently tied to the material used to measure it, and in many cases the specific instrument used.

To account for this, prior to formal experimentation, an instrument must be calibrated against a known and understood radiation beam in order to translate the measurements obtained, for example photocurrent, into well known dose measurements, in Gy. This must be done also with focus on the radiation energies of interest to be later measured, e.g. for diagnostic radiography energies of 10–150 keV or radiotherapeutic energies of 1–25 MeV.

Therefore, if one wishes to make meaningful measurements of radiation dose that can be generalised to arbitrary experimental and clinical conditions, it is best practice to follow standardised codes of practice, such as those described by Eaton et al [36]. For diagnostic X-ray ranges, as are the primary concern in this work, ionisation chambers are considered the gold standard for the numerous advantages they hold within this energy range [37]. But further control is required than particular instrument, such as control of the X-ray output filtration and consistency in surrounding materials to account for back scattered radiation. Upon fulfilling these requirements, a radiation dose measurements made can be used for reference and repeatability studies, as long as the conditions are stated.
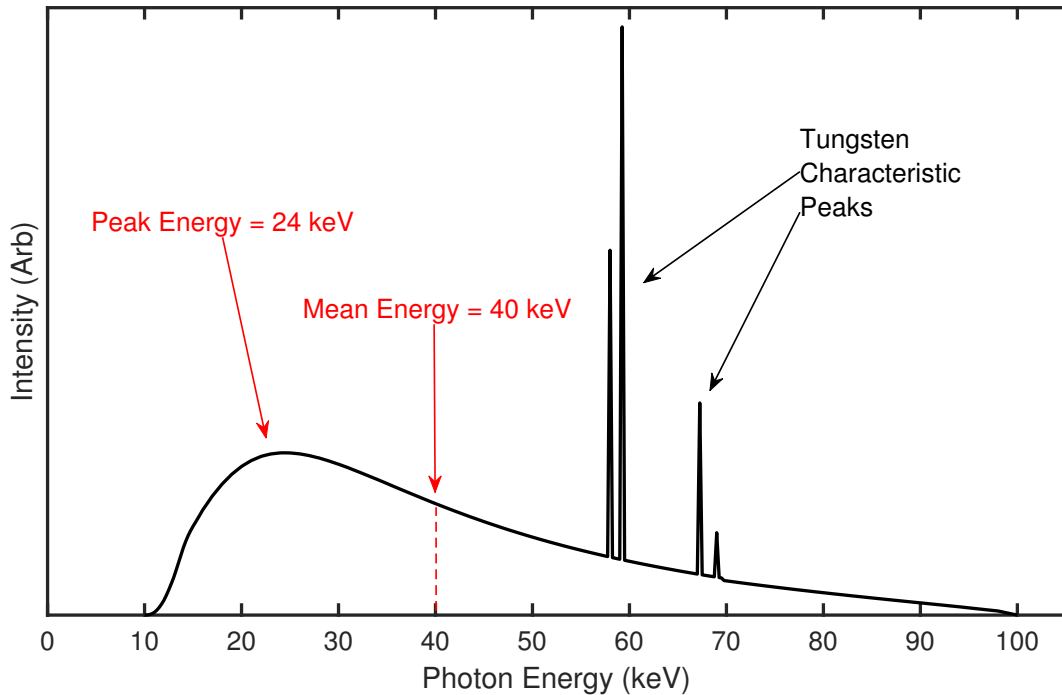
Figure 3.1: An example of a bremsstrahlung X-ray Spectrum for a tungsten target X-ray tube operating at $100\,\mathrm{kVp}$, showing the characteristic X-ray peaks and mean energy of the spectrum

3.2.2 X-Ray Spectrometry

Determining the spectrum of a continuous X-ray source can be a difficult task that requires complex equipment and accurate knowledge of the material geometry inside the X-ray tube and generator apparatus. This task is nevertheless essential in performing dosimetry calculations.

The physics of an X-ray tube are based on the conversion of electron kinetic energy into either heat or photon energy. To produce X-rays a beam of electrons, accelerated by a strong electric field between an anode and a cathode, is focused upon a small area on a heavy metal material, typically Tungsten or Molybdenum, and experiences deceleration upon impact with the atoms of the material. The vast majority of electrons that decelerate through this process transfer their energy as

heat. However, a small percentage of these generate X-rays of energies equal to the instantaneous energy exchange of each electron during their interactions with the atoms of the material. The highest energy photons will be generated by electrons that lose all of their kinetic energy in a single interaction with the target atoms, whereas lower energy photons are generated by multiple interactions between one electron and the material. This exchange leads to many more photons of a lower energy to be produced than of the higher and maximal energies.

A standard Tungsten target X-ray tube will produce a broad spectrum of X-ray energies, typically between 10–150 keV, the upper limit of which is given by the kV voltage potential that the anode of the tube is held at and the lower limit determined through beam filtration from materials that separate the Tungsten target from the external world. Between these two limits sit a variety of intensity weightings for each energy level, affected by the filtration materials, the kV potential, tube geometry and characteristic radiation peaks specific to the target material, the interdependence of which cause standard X-ray spectra to be difficult to accurately determine through theoretical calculations.

3.2.3 Thermoluminescence Dosimetry

A reliable and widely adopted method for determining radiation dose experienced through a small volume is with the use of Thermoluminescent (TL) materials as Thermoluminescence Dosimeters (TLDs), which absorb high energy photons and store their energy in excited electron states. Figure 3.2 shows the process of X-ray absorption and energy storage in a TL material. Through interaction with incident
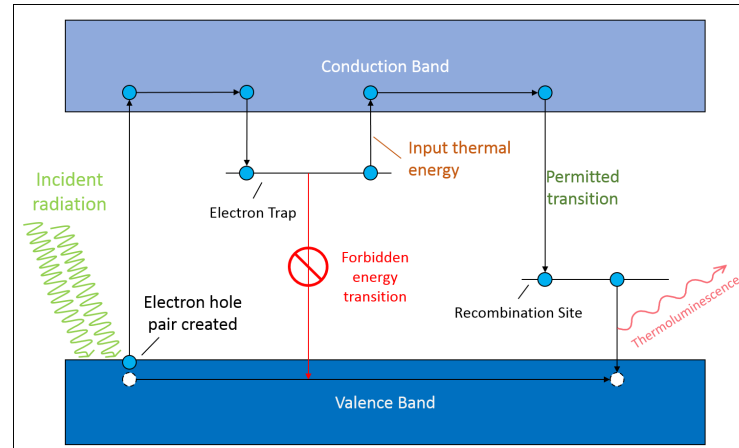
Figure 3.2: Energy level diagram of the Thermoluminescence process describing the energy transitions an electron exhibits

X-ray photons, an electron is promoted to the conduction band whereupon there is a certain probability for that electron to fall into an Electron trap, where it will remain for an extended period of time (minutes–years). Since moving from the trap states back to the valence band are forbidden transitions, the electron can only de-excite down to the valence band if it is once again promoted in energy to the conduction band. This is most easily achieved through heating of the material, directly adding energy to all electrons in the lattice.

There is then a second probability that the electron will fall through to a recombination site at a specific energy, and upon de-excitation from this new level, a visible or infrared photon is emitted. These photons can be counted by a photomultiplier tube and will thus correspond directly to the the photon energy fluence or dose of radiation. Given a well characterised X-ray source for initial calibration, the dose from a similar X-ray spectrum can be determined by the thermoluminescent light output of the TLDs.

There are multiple electron traps at different energies in a TL material, deter-

mined by the dopants used in manufacture, and therefore an array of TL emission peaks, each released at temperatures respective to the energy depth below the conduction band of the electron trap. Due to the chaotic nature of thermal vibration, these electron traps will decay at a rate proportional to the temperature of their surroundings, with low temperature traps lasting only a few minutes and higher temperature traps lasting up to a few years[38]. This leads to another consideration that must be taken into account with TL Dosimetry, in that all dose information in dosimeters will decay with time. Thus the highest temperature traps are the most reliable for use in dosimetry, and the decay time scale for the useful peak in LiF:(Mg,Ti) is around 10% of the TL intensity per month or a half life of around 200 days. [38, 39].

It is useful to be cautious with exposure however, as TLDs exhibit both supra-linearity and radiation weakening. Supra-linearity occurs upon receiving a dose above a certain threshold in each TL material, which causes the photoresponse to dose to increase at a greater gradient than initially determined from calibration. In LiF:(Mg,Ti) for example supralinearity begins at around 10^3 Gy [39]. TLDs are also susceptible to permanent radiation dose effects, as when reaching larger doses ($\sim 10^5$ Gy) a TL material will suffer radiation damage and lose sensitivity, which is required to remain constant for dose measurement purposes. Therefore, radiation dosage testing should avoid the use of large extended period doses and limits the experiments to short exposure timescales.

3.2.4 Simulation

Various methods through software exist to provide a general approach to predicting X-ray spectra [40, 41], but these lack the bespoke application for the use in precision dosimetry, since each X-ray system has itself a unique design for the geometry such as inherent filtration, beam distances, anode material and angle along with experimental details specific to each setup.

In order to adequately asses the energy distribution and deposition within a radiation field a virtual model must be built in order to accommodate the vast complexities of the evolution of radiation propagation. Monte Carlo (MC) analysis is the most appropriate type of radiation model, as this approach approximates the micro level physics interactions as probability distributions to dictate the behaviour of various physical processes on the macro level. This vastly decreases the time it takes to simulate the propagation of any one photon while preserving micro-level accuracy by utilising statistical knowledge of the physicals processes involved.

The MC code GEometry ANd Tracking 4 (GEANT4)[42, 35] was used to simulate the radiation environment of the lab based experiments, due to its comprehensive consideration of physical processes and the flexibility of its C++ language base. The QGSP_BERT_HP (Quark Gluon String Physics with Bertini cascade and High Precision) physics list was used to dictate the involved physics processes, as it contained all of the relevant physical phenomena for low energy X-ray interaction and the knock-on electron effects, however most models are still correct as low energy physics processes tend not to vary between separate considerations of standard

models of particle interaction.

3.3 Methodology

3.3.1 Spectrum Simulation

Initially, an approximation of the spectrum of the X-ray sources in use was sought through use of an empirical X-ray spectrum prediction program, SpekCalc [40]. This program uses empirical studies of X-ray spectra to predict new spectra based on user specified filtration and employing mathematical models to predict how this filtration will affect the spectrum. This however did not provide an adequately accurate X-ray spectrum for the simulation of X-ray dose, as the inherent filtration in the X-ray tube was not considered by the program, and only similar materials were able to be substituted. The application of SpekCalc is aimed towards clinical use, where environments are much less variable.
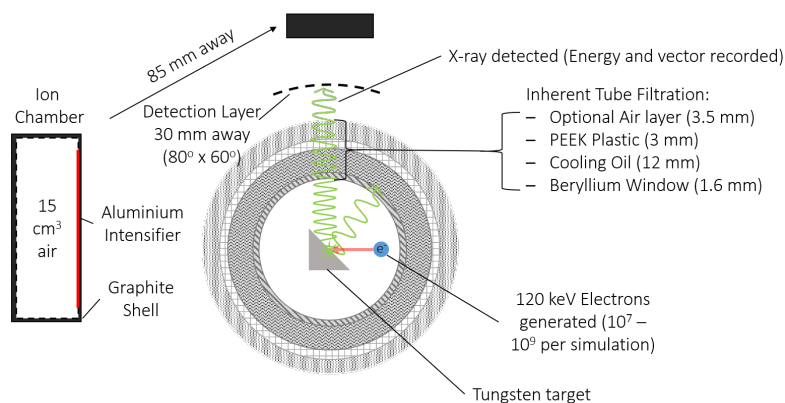
Figure 3.3: A cross sectional diagram of the geometry used in GEANT4 to simulate the generation of X-ray photons and subsequent recording

To determine more accurately the energy spectrum and intensity of the source, the principle components of the X-ray generator were modelled in simulation, a

cross section of which is shown in Figure 3.3. The simulation was modelled off of the engineering drawing and inherent filtration statement of the X-ray generator model, a Metrix SAXG 1701 Cone Beam Generator[43]. This model was composed of a tungsten target volume angled at 50.2^o to the incident electron beam, encapsulated within multiple hollow spheres of material with thicknesses representative of the inherent filtration of the source, which was quoted as 1.6 mm of Borosilicate Glass, 12 mm of Cooling Oil and 3.5 mm of PEEK plastic. Also in use was a further 3.5 mm thick air layer with adjustable density to account for different levels of air attenuation that may be experienced by the X-ray beam. For example, this air layer was set to a density 1000 times greater than air to correspond to 3.5 m of air, which was then used for recreating the spectrum measurement collected with the CdTe spectrometer without sacrificing spatial sensitivity. Effects of this simplification are considered to not contribute undesired counts in the detection layer during the simulation as the counting method was not heavily affected by spatial geometry, and this simplification was a necessary requirement to decrease processing time to a realistic standard.

The photons in this simulation were detected as they crossed the surface of an empty spherical volume that enveloped the system. X-rays considered to be contributing to the spectrum were photons which were within the angles of exit as specified by SAXG X-ray source's fan beam dimensions, $(80^o \times 60^o)$ and, after recording their energy, were added to a histogram with 0.25 keV bins. This spectrum was then exported to be used as the input to the GEANT4 General Particle Source class, which supports user input weighted energy histogram distributions.

This model also included a volume built to replicate the Ionisation chamber that was used in the lab, also shown in figure 3.3, to then compare dose measured by the ion chamber with the dose deposited in this virtual volume. This was done with all materials of the ion chamber taken into account, including the outer 1 mm graphite walls, the 0.15 mm aluminium electrode and 15 cm^3 air volume within which dose deposition is measured. However, because of the low interaction probability with air, along with a small solid angle and large distance from the target, dose detected by this volume was low, but provided reasonable agreement with reality when compiling the doses recorded from 40 simulation runs.

The current in the generator was typically 1.2 mA, which corresponded to an electron flux of $7.49 \cdot 10^{15} \mathrm{s}^{-1}$, so in order to determine the flux of X-ray photons, a simulation of $2 \cdot 10^9$ electrons at 120 keV were directed at the target anode and then the number of photons produced was divided by the amount of time real time that this accounted for at a current of 1.2 mA, 2.67×10^{-7}s, to find the photon flux emerging from the X-ray source.

3.3.2 X-ray Spectrometry of the SAXG Tube

For the purposes of validation, it is imperative to provide alternative sources to confirm the simulation and allow generalisation. Thus the X-ray source spectrum was directly measured via X-ray spectrometry.

To make a direct measurement of the spectrum of the SAXG 1701 source an AmpTek X123 Cadmium Telluride spectrometer was used. A diagram of the set-up for this measurement is shown in Figure 3.4. The spectrometer was placed 3.5 m
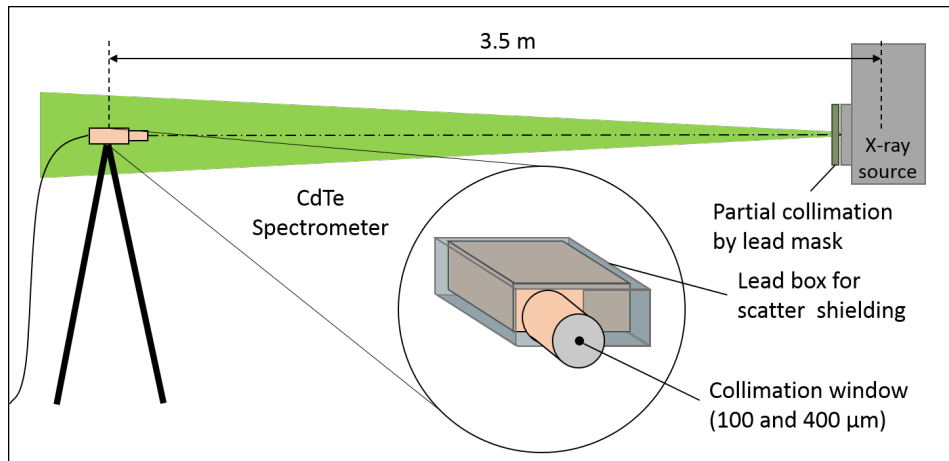
Figure 3.4: A diagram of the experimental set up for the CdTe Spectrometer as it was placed in front of the X-ray source. The X-ray tube operated at 120 kVp and 0.6 mA

away from the SAXG source and set on a tripod to adjust the detector direction and aligned using a laser level to point directly towards and perpendicular to the focal spot of the tube. The tube current was reduced to its lowest setting of 0.6 mA and the spectrometer used a 400 μm pinhole in order to reduce the photon flux incident upon the detector. The spectrometer was set to accumulate for 30 minutes under constant exposure from the X-ray beam at 120 kV, as this was the energy of interest for the TLD measurements. This was then repeated with a 10 mm plate of Aluminium used to harden the beam. The dead time of the detector was observed to be between 45-55% of the live time, and during a 20 minute exposure 6×10^{10} counts were recorded for an unfiltered beam, while 2.8×10^{10} were recorded for 1 cm.

Pulse pile-up effects of photons were observed, where the detector counts the energy from multiple photons as a single photon event, due to the detector readout frequency being lower than the incident photon count. Further beam restriction was achieved by tighter collimation using a 100 μm pinhole just behind the 400 μm pin-

hole, to collimate the beam and reduce the total number of X-rays incident upon the CdTe sensor. It was also found that the spectrometer would detect many high energy photons between 40 and 80 keV while the collimation window was covered, which led to the conclusion that the inside of the detector was not adequately shielded from scattered and background X-rays. This was amended by assembling a box of 1.2 mm thick lead to house the spectrometer in, which removed any signal produced when the window was covered.
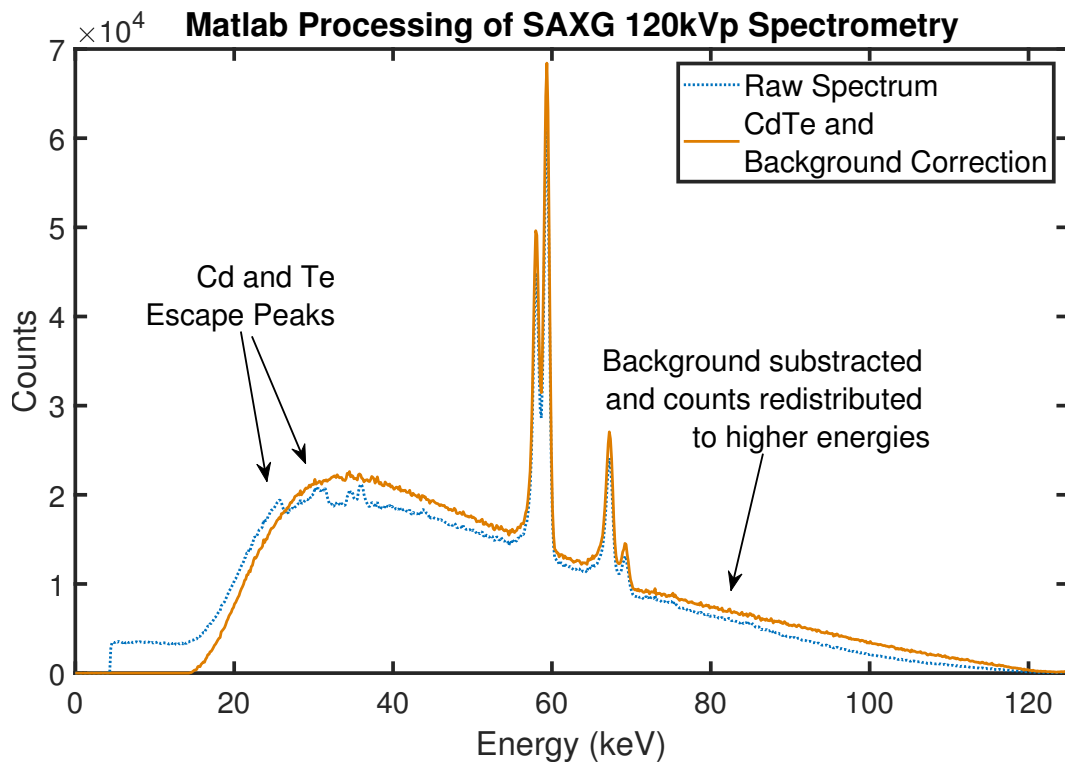
Figure 3.5: An example of the correction for Cadmium and Tellurium escape peaks, where some photon counts of energies below 24 keV (Cd) and 35 keV (Te) are redistributed to higher energies based on the excess predicted to be generated from CdTe escape peaks.

A correction was performed for CdTe based escape photons that contribute to erroneous counts in the spectrometry. This was achieved through MC simulation of the spectrometers sensitive element, a 3.2x3.2x1.0 mm, and drawing a compari-

son between the energies of photons being delivered to the element and the energy actually deposited by photons or energy from subsequent characteristic photons. Through using this, a correction could be made for the true energies and counts of photons according to the observed energies and counts due to the Cadmium Telluride absorption. Based on the intensity of the Cd and Te peaks in the spectrum, these counts were removed and redistributed to higher energies in accordance with the simulated value of average energy information lost per keV.

Shown in figure 3.5 is a spectrum containing the undesired contribution and compared alongside a spectrum corrected for this contribution. Figure 3.5 also features the subtraction of the background scattered radiation, however this was already small as the spectrometer was fully surrounded by lead shielding. A correction for this background removal is described by Redus et al. [44].

The spectrometry measurements were taken at a distance of 3.5 m from the source in order to reduce the flux to a manageable rate for readout, which featured the consequence of subjecting the observed spectra to 3.5 m worth of air attenuation, so the result obtained could not be directly applied to the spectra used in simulation. In order to account for this, a reverse attenuation multiplication was run on the spectrum using the rearranged attenuation equation:

$$I_0 = I e^{L \cdot \mu_{e,air}} \tag{3.1}$$

Where I_0 and I are the initial and observed intensity respectively, $\mu_{e,air}$ is the attenuation coefficient for air for each energy level and L is the thickness of material

through which the beam traverses. The intensity of this correction is shown later in figure 3.9.

3.3.3 Dose Simulation

The second stage of simulation was to determine the radiation dose deposited in various volumes of interest in order to validate this simulation against reality. In this stage both the ion chamber and the TLDs were modelled to try to replicate the dose measurements made during experiment.

A diagram of the experimental and simulation geometry of the TLD are shown in Figure 3.6, where the TLDs were measured to be, and hence modelled as, 3.22x3.22x0.9 mm volumes of LiF with Mg and Ti in concentrations of 200 ppm and 10 ppm respectively[45]. These were situated inside of TLD sized cavities in a 100x100x3 mm perspex volume which modelled the TLD case and then were arranged in various configurations to match the cavities that the TLDs fit into and to make efficient use of the TLDs.

X-rays were modelled as a point source at a distance of 186 mm from the TLDs placement and their directions were randomly distributed across an $80^o \times 60^o$ beam spread, which corresponded to the SAXG 1701 quoted beam geometry. Each simulation processed $2 \cdot 10^9$ photons emerging from the point source, the maximum allowed per run, taking approximately 20 minutes to run and recorded the total energy absorbed through either photon or electron interactions with the material volumes of the environment. This energy deposition was then divided by the mass of the volume in which it was deposited to find the dose delivered in Gy to each
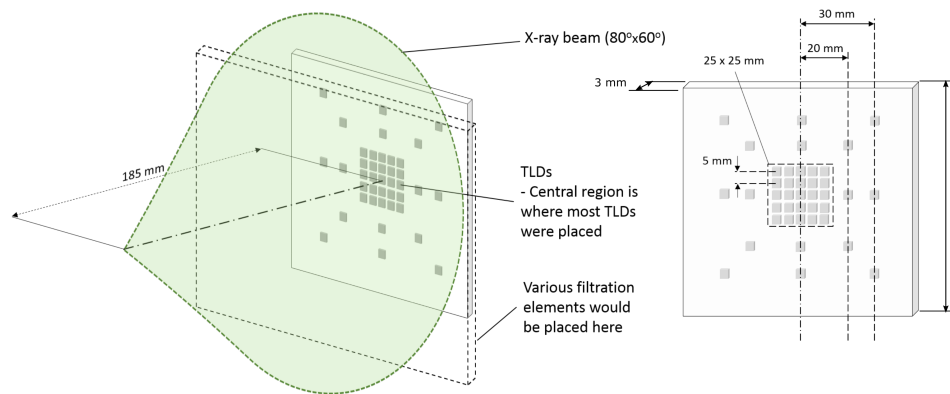
Figure 3.6: A diagram of the experimental and simulation geometry for exposure of the TLDs, where all measurements were taken during experimentation and later reconstructed in simulation

volume.

3.3.4 TLD Dose Measurements

The experimental work was carried out using a Metrix SAXG 1701 industrial X-ray unit, controlled by a General User Interface constructed in Matlab for timed exposures. TLDs were held in a 10x10x3 mm Perspex case, shown in Figure 3.6, which was mounted above the X-ray source by a fixed positioning frame.

Dose measurements were performed using 45 TLD-100 (LiF:MgTi). A variety of geometric and material environments were used, evolving to increase complexity with each iteration or aiming to investigate discrepancies in earlier experiments when compared with simulation. For example, when using a filtration of Aluminium and Steel there was a stark difference between the dose observed and dose predicted in simulation, so then proceeding to expose only with Steel filtration to understand if either the steel is not composed as initially understood or if the

simulation is failing elsewhere. This particular instance was resolved through more accurate modelling of the steel compound used.

In order to not affect the long term radiation response of the TLDs, the approximate dose during each exposure was initially limited to not exceed 100 mGy, and later no more than 1 Gy. This set the time of exposure of the experiment to 12.27 seconds, which introduced the following problem. The off-on voltage ramp-up period for the X-ray source took up a significant portion of this time ($\sim 1.5\,\mathrm{s}$), while also being uncontrollable and the precise nature unknown. To account for this uncertainty, a lead shutter placed upon a lateral transport stage was used as a control for the exposure duration of the TLDs, as this method could be controlled remotely through serial commands and the shutter transfer time calculated or recorded. The lead shutter was found to decrease the dose rate in the beam by a factor of 1000, and since the tube warming up period was only a few seconds, this was assumed to be a negligible contribution compared with the error in the TLDs reading ($\pm \sim 1\,\%$).

For use with the SAXG 1701 X-ray source, the batch of TLDs were calibrated by exposure to a known dose of 10 mGy delivered by a clinical Carestream DRX Evolution Dual Bucky X-ray system (Carestream Health Inc., United States), using a tungsten target X-ray source (Rad-60, Varian Medical Systems Inc., United States), at the Royal London Hospital. The source was operated at 120 kVp and 500 mA for exposures lasting 160 ms. To deliver this dose, an ion chamber was placed on a phantom block and exposed many times to find the correct setting. The ion chamber was then removed and the TLDs were positioned in place for a single 10 mGy exposure, after which the TLDs were removed and the ion chamber used

for several more exposures to validate the TLD dose. The TLDs were subsequently read out several days later, to simulate day long breaks between exposure and read-out. Once their response was logged they were subsequently annealed to remove the radiation history of each chip. This was repeated 3 times to find the overall variance in the response of each TLD, in order to advise against the use of any that were unreliable. Only one TLD was found to be above 5% of the standard deviation of the previously recorded calibration measurements of the batch, which was then left out of experimental use. For each experiment a set of 3-5 randomly selected TLDs were kept out of any radiation exposure, but still kept present in the lab, as control measures, but none showed any dose larger than 0.1 mGy, which is within the error of the TLD reader.

TLDs were read out 1-4 days after exposure, using a Toledo TLD reader. Following readout each batch was annealed at 400$^{\text{o}}$C and then 100$^{\text{o}}$C during a 5.5 hour cycle to reset the 'radiation history' of the chips.

There were multiple experimental geometries arranged for the TLD experiments (Steel was composed of 70% Fe, 18% Cr, 10% Ni and 2% Mn):

- Bare exposure, shielded only by the basic 1 mm of Perspex from the TLD case

- Filtered by 1 mm of Al

- Filtered by 1 mm of Graphite

- Filtered by 0.914 mm of Steel, 0.1 mm of Al and backed with 2.0 mm of Pb

- Half covered by 0.914 mm of Steel only

- Filtered by 0.1 mm Al and backed by 2.0 mm of Pb

- Filtered by 10 incremental layers of 0.1 mm of Cu

- Filtered by 10 incremental layers of 0.1 mm of Al

- Filtered by 5 incremental layers of 1 mm of Al

- Filtered by 10 mm of Aluminium and 5 incremental layers of 0.2 mm of Cu

- Filtered by 10 mm of Aluminium and 5 incremental layers of 1.0 mm of Al

These geometries were chosen with the aim of creating a non-trivial environment for the dose deposition model to calculate, while remaining simple enough to measure and model accurately. Incremental layer exposures were primarily to investigate aspects of the spectral distribution of the beam through the cumulative effect of material filtering on the dose. This was deemed a crucial part of the dosimetry investigation, primarily in prediction of the effects of additional metallic layers to X-ray detective devices.

3.3.5 Consideration of Errors

The errors in the dose predicted through simulation were produced through taking the statistical error of measurement, i.e. a root mean square of the energy of each energy deposition event in GEANT4, so that every time dose was added to a volume an uncertainty proportional to the energy of that event was added to the total uncertainty. This led to very small error considerations for the simulations as each dealt with many millions of events, however, this error was the only significant cause of uncertainty in the simulation, and error in the geometry was considered only in the experiments divergence from the simulation. Errors in TLD experimental dose values were determined using the variance of each individual TLD taken from the calibration tests, which nominally subjected each TLD to the same dose 3 times so that all deviations were deduced to be inherent in the TLDs. The error in ion chamber measurements was given by the operating manual[46] as $\pm 1\%$ for X-ray energies between 30–150 kVp.

3.4 Results and Discussion

3.4.1 X-ray Spectrometry
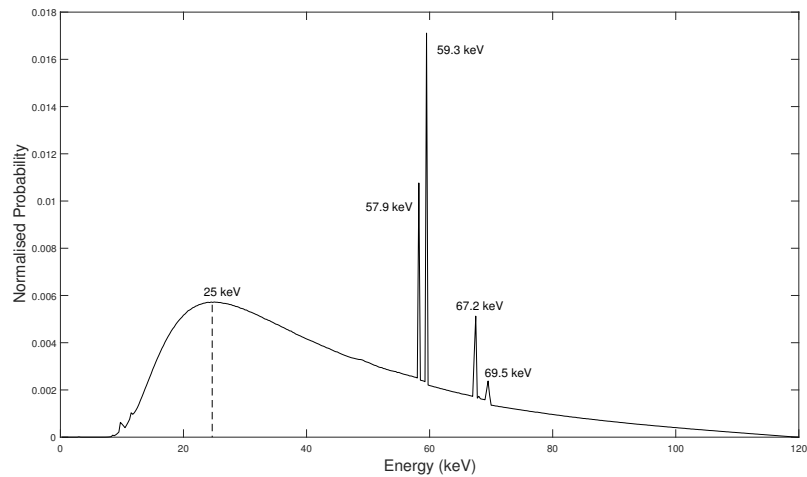
Figure 3.7: A histogram of the MC simulated X-ray spectrum obtained through GEANT4, using energy bins of 0.25 keV and totalling 2.8e8 counts

The initial X-ray spectrum obtained through GEANT4 simulation is shown in Figure 3.7, where the histogram has bins 0.25 keV wide. The simulation for this spectrum used inherent filtration materials and thicknesses specified by the manufacturer. The characteristic K_α and K_β lines of tungsten are clearly visible, their height enhanced by the resolution of the simulation, along with a few small L lines at ~ 10 keV. This spectrum was obtained through the simulation of $7 \cdot 10^{10}$ electrons, and is comprised of the contributions from $\sim 10^8$ photons. The peak bremsstrahlung energy is situated at 25 keV and the maximum at 120 keV.

The CdTe measured and GEANT4 simulated spectra are shown in Figure 3.8. Most clearly, the energy resolution of the simulation is much better than that of the experiment, as this was only limited by binning photons by their absolute energy
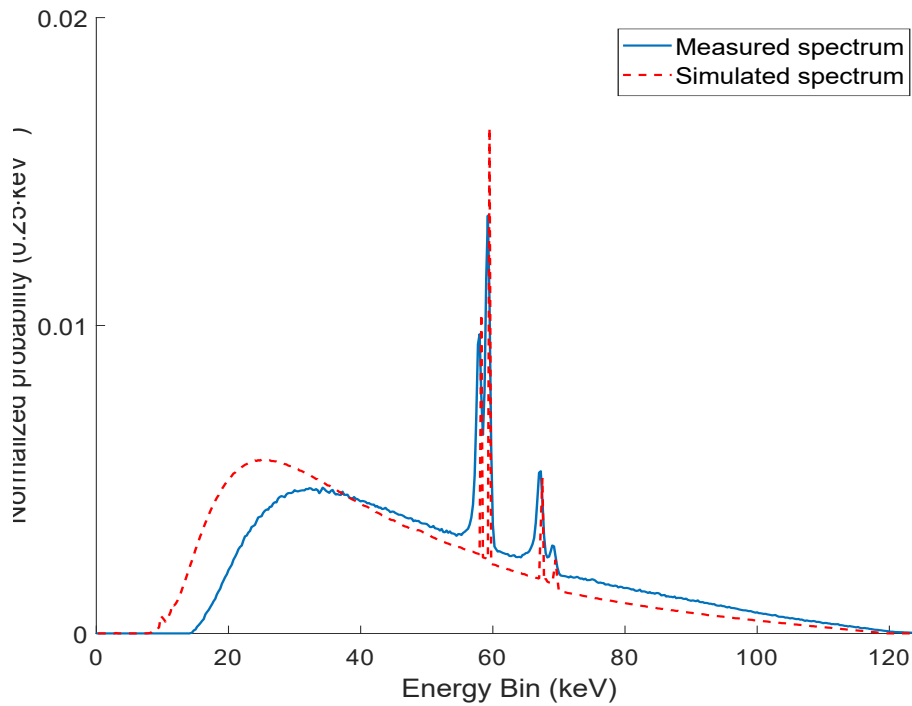
Figure 3.8: Two histograms of the MC simulated X-ray spectrum compared with the spectrum obtained through X-ray spectrometry with the X123 CdTe spectrometer

level, while the spectrometry involves blurring effects, as discussed earlier in 3.3.2. The simulation clearly produced many more low energy photons than were detected through measurement, thus some unknown level of filtration must be acting upon the measured spectrum that is not included in the simulation or quoted by the manufacturer. It is possible that this could originate from ablation based evaporation of the tungsten anode element resulting from long term use and then deposition on the inside wall of the X-ray tube, acting as a thin layer of high-Z filtration. The X-ray unit could not be disassembled to analyse this however. It is also possible that, through misalignment of the spectrometer with the focal spot, that the measured spectrum is filtered through a small element on the edge of the tungsten collimator.

The spectrum simulated using the quoted material thicknesses for filtration also
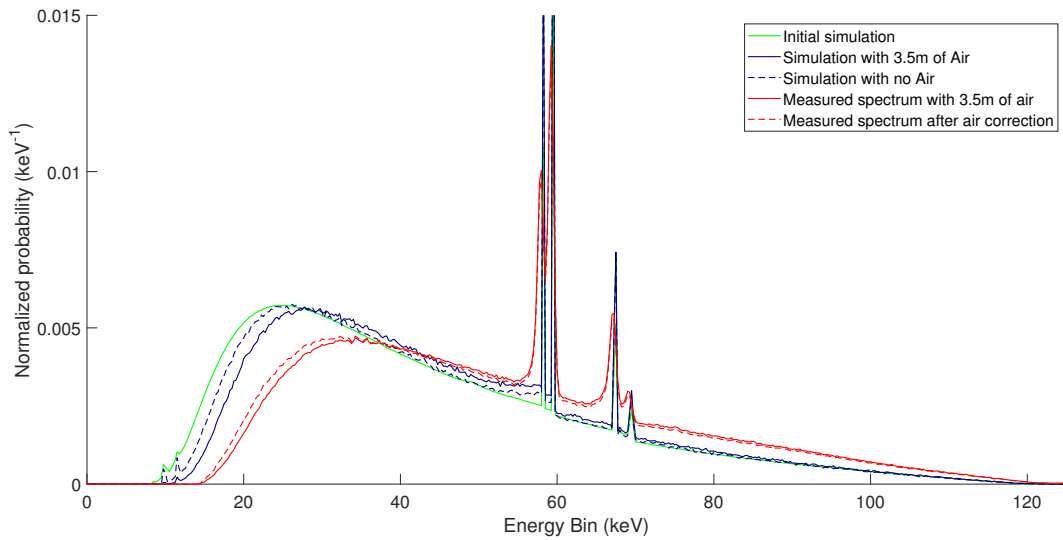
Figure 3.9: X-ray spectra: Green solid line - Initial spectrum simulated in GEANT using filtration from the user manual of the generator, Solid blue line - Simulated spectrum after increasing the inherent filtration to specifications in the CAD model and also with 3.5 m of air attenuation, Solid red line - the CdTe measured spectrum, Dashed blue line - Simulation without air attenuation, Dashed red line - Measured spectrum after an applied air attenuation correction

did not provide very accurate results when compared with TLD dose measurements. It was not possible to take the X-ray generation unit apart to examine the true filtration in use, so access to the CAD file of the SAXG X-ray generator was sought out. After analysis of the CAD file, it was observed that the inherent filtration of oil should be ~ 3 times larger than quoted, and so a new simulated spectrum resultant from this knowledge was generated, which is shown by the dark blue dashed line in Figure 3.9 alongside the initial spectrum in green.

The dashed red line in Figure 3.9 shows the effect of the air correction on the measured spectrum, where the bremsstrahlung peak has been shifted by $\sim -2\,\text{keV}$, while higher energies remain unaffected. This was performed through calculating a reverse attenuation approximation based on rearranging equation 2.2 to find the initial intensity. The blue lines show simulated spectra with and without 3.5 m worth

of air attenuation, which shows a similar difference and validates the use of this attenuation correction. This is not a faultless correction however, as the attenuation causes losses in the data at the lowest of energies where the counts are reduced to 0 and since these values cannot be multiplied back to their original count their contribution to the spectra cannot be accounted for.

3.4.2 Dose Rate

Once a spectrum had been determined by measurement the photon fluence was still unknown. Given that the tube operated at $1.2\,\text{mA}$, a photon fluence rate was established by considering the electrons in the simulation as a small portion of the total number of electrons per second ($7.49 \times 10^{15}\text{e}^-\text{s}^{-1}$) and scaling the photons recorded in simulation to a value for photons per second. However, this method produced a photon flux which incurred a dose rate too high in comparison to doses recorded with the Ion Chamber. Figure 3.10 shows a comparison between the dose rate measured by the ion chamber at distances up to $420\,\text{mm}$ from the X-ray focal spot and a dose rate measured by a virtual ion chamber placed at the same distances in simulation, where the dose rate follows an inverse square law with distance.

The X-ray fluences acquired for each spectrum through this method are shown in Table 3.1. The initial photon fluence was 4.36×10^{12} photons per second over the $80 \times 60°$ beam spread. The scaled dose rate was arrived at by increasing the photon fluence in simulation by the average ratio between the observed and simulated dose rates, which was ~ 1.8 times larger to a new value of $6.78 \times 10^{12}\text{s}^{-1}$. This method was also repeated for each spectrum used in experiment, so that each one produced
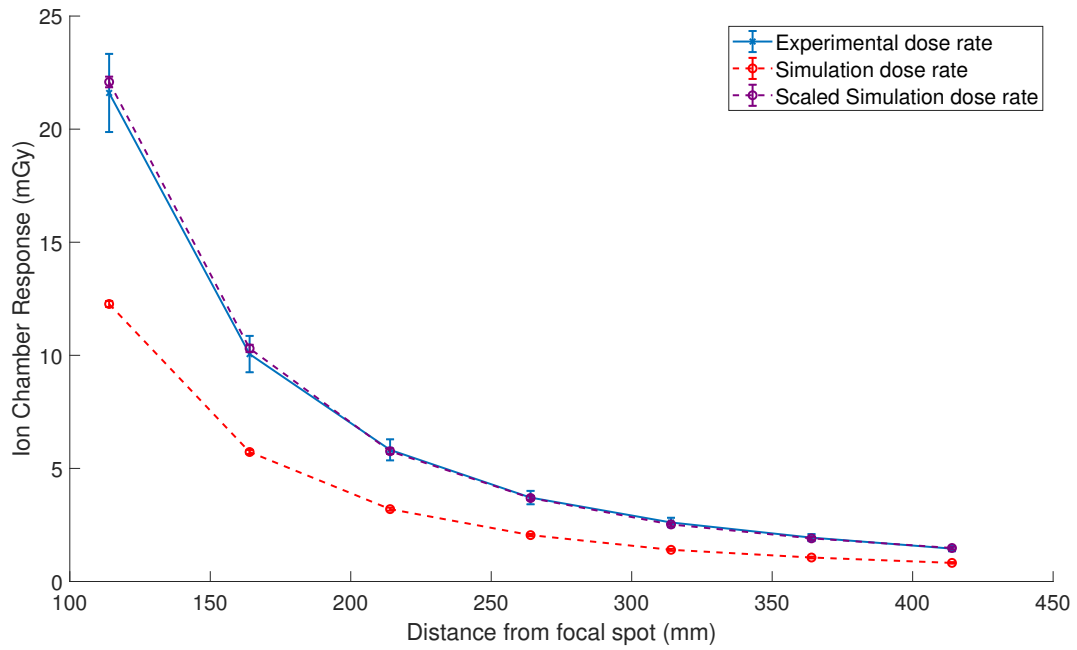
Figure 3.10: The dose per second measured by the ion chamber placed at incremental distances from the focal spot of the X-ray tube. The experimentally measured values are shown in blue, the simulation values are shown in red and the simulation values after the fluence is scaled by the average difference between the experiment and simulation is shown in purple.

the same dose rate for the ion chamber at those set distances, setting a standardised level of exposure from which deviations could be considered as a result of an inaccurate energy spectrum.

Spectrum Specification	Photon Fluence (s^{-1})
Fluence Predicted by simulation	$(8.18 \pm 0.08) \times 10^{12}$
Simulated Spectrum with inherent filtration according to SAXG manufacturer specifications	$(4.45 \pm 0.15) \times 10^{12}$
Simulated Spectrum with filtration defined by CAD model	$(4.88 \pm 0.16) \times 10^{12}$
CdTe Spectrometry produced Spectrum	$(6.78 \pm 0.22) \times 10^{12}$

Table 3.1: The number of photons considered to be emerging from the SAXG X-ray source per second in simulation

3.4.3 TL Dosimetry

Filtration (exposure time)	Mean Experimental Dose (mGy)	Mean Simulation Dose (mGy)	
		CdTe Spectrum	Simulated Spectrum
No Filtration (13s)	95.1 ± 1.0	108.0 ± 0.2	96.6 ± 0.1
1 mm of Aluminium (13s)	76.4 ± 0.8	84.4 ± 0.2	61.0 ± 0.2
0.1 mm Aluminium, 2 mm Lead back (61s)	442 ± 4	491 ± 2	432 ± 4
0.914 mm of Steel 0.1 mm Aluminium, 2 mm Lead back (61s)	84.6 ± 0.8	96.9 ± 0.4	46.6 ± 0.5
0.914 mm of Steel (61s)	95 ± 1	97.2 ± 0.3	47.0 ± 0.3
10 mm of Aluminium (61s)	138 ± 1	136.0 ± 0.4	72.7 ± 0.3

Table 3.2: A table of the mean dose recorded by TLDs in experiment and simulations where the filtration and exposure was uniform, for either times of 13 or 61 seconds.

For simulation of the dose experienced by the TLDs, two spectra were consid-

ered for the X-rays, the measured CdTe spectrum and the simulated spectrum with adjusted filtration, which are both shown in Figure 3.9. For most exposures, where only the central region of the TLD holder was used, there was only very small lateral displacement from the centre of the beam (up to 4.4°), and because of the spherically symmetric filtration of the beam, it can be assumed that the dose received by these TLDs was fairly uniform and can be averaged for higher precision. Table 3.2 shows the mean dose recorded by such TLDs in experiment and in simulation with the two considered spectra.

The CdTe spectrum provides much more accurate dosimetry when the X-ray source is subjected to strong filtration, such as the steel and the 10 mm of Aluminium, but is somewhat deviated from the measured values at low filtration. On the contrary, the simulation based spectrum was accurate in determining the dose only when small amounts of filtration were used, such as with the bare and the 0.1 mm of Aluminium exposures. While the 1 mm of Aluminium exposure sits in between both of these predictions. This interchange from one spectrum to the other over increasing filtration indicates that the low energy weightings of the simulated spectrum play a greater role in dose deposition than the CdTe spectrum, but when filtered, the real spectrum approaches something more similar to the weightings dictated by the CdTe spectrum.

It is possible this discrepancy is a result of scattered radiation, which would have been present in the TLD measurements but filtered out during the spectrometry. Scattered radiation from the surrounding room would be much more prolific in low filtration exposures, while the simulation was not able to model the full environment

of exposure such as room boundaries, tables and metallic structures.

As such, the preference for the CdTe spectrum at higher filtration is a result of the reduction in back scatter and also from overriding the unknown nuances of the inherent filtration of the source, as the low energy end of the spectrum is removed. Accurate dosimetry with this source is thus much easier to achieve when using a strong filter to remove low energy photons from the beam, however, when aiming to reach high dose levels this is a hindrance and decreases the reasonably achievable dose.
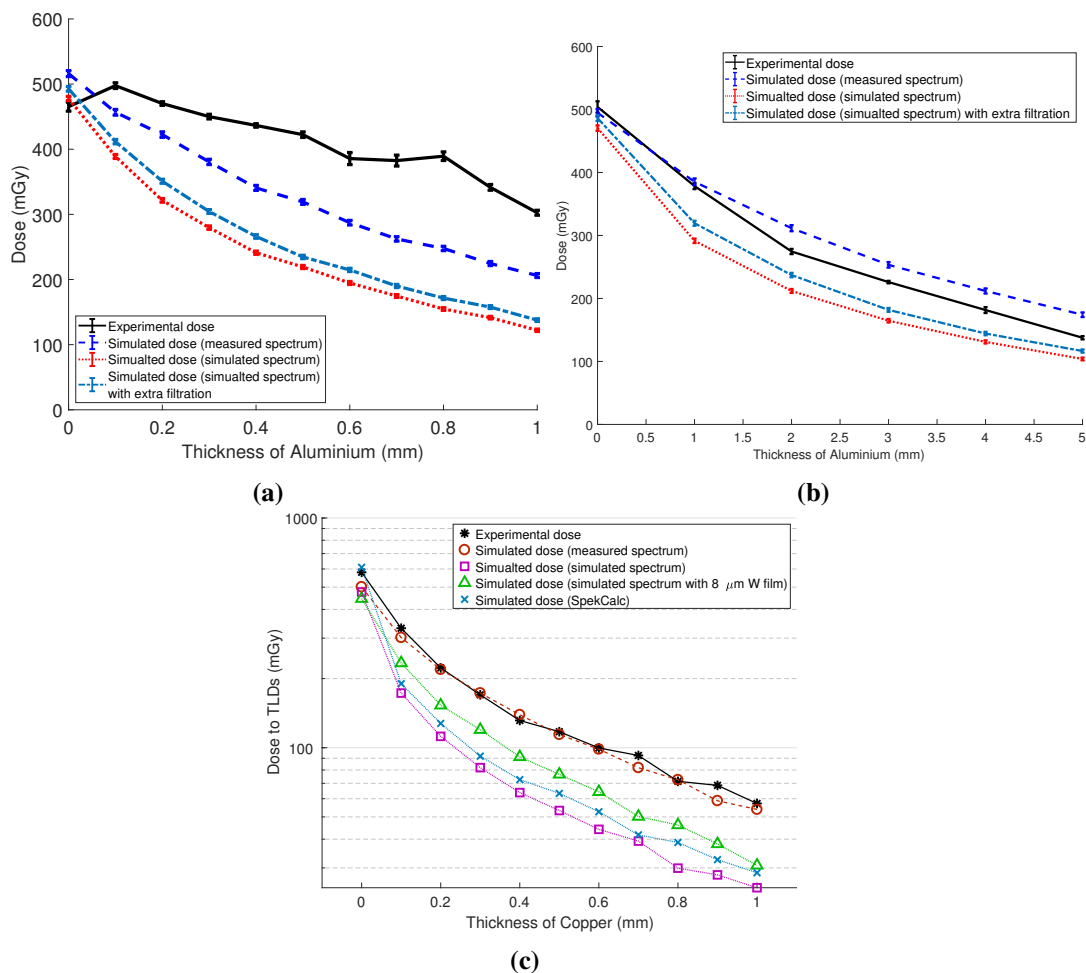
Figure 3.11: Dose recorded by TLDs in experiment (black solid lines), and simulations using various spectra (blue dashed -CdTe measured spectrum, pink dot-dashed - simulated spectrum, red dashed - simulated spectrum with adjusted inherent filtration) for thicknesses of filter materials (a,b: Aluminium, c: Copper)

To investigate this further, the TLDs were exposed using cumulative layers of filtration with Aluminium or Copper, which are shown in Figure 3.11. Shown in Figure 3.11a & 3.11b are the doses recorded by the TLDs and the doses determined through simulation using several spectra after the source was filtered by cumulative layers of Aluminium. Figure 3.11c shows the same but with Copper filtration layers. The strongest agreement with experimental results was from the CdTe spectrum, whereas the weakest was consistently from the simulated spectra (pink and red), cementing the CdTe measurement as the prevailing representation of reality.

The strongest departure from reality is the experiment vs. simulation of the 0-1 mm of Aluminium, where none of the simulations line up very well with the dose recorded by the TLDs. This is in contrast with the other two experiments, which had much closer agreements, which casts some concern on to the performance of this 0-1mm Al experiment in the lab.

(a)   **(b)**
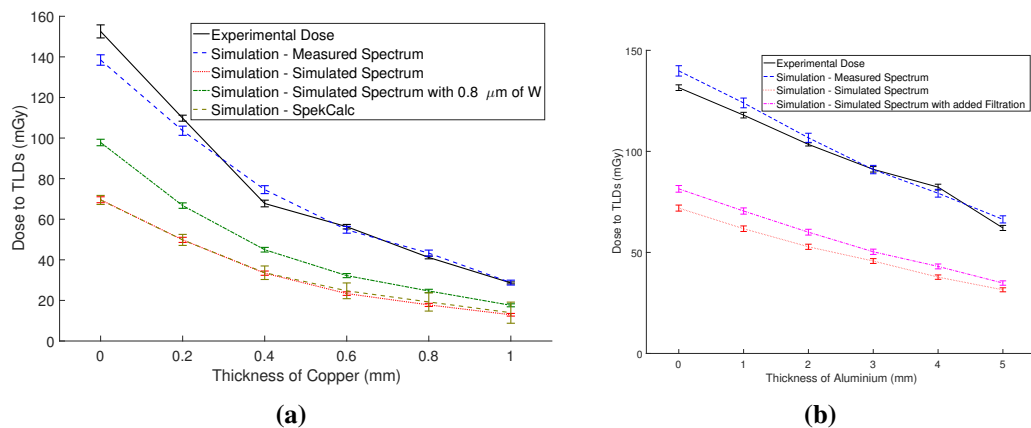
Figure 3.12: Dose recorded for various thicknesses of (a) Copper and (b) Aluminium fil-
tration, after both are initially filtered by 10 mm of Aluminium, in experiment
(black solid lines) and simulation using various spectra (blue dashed - CdTe
measured spectrum, pink dot-dashed - simulated spectrum, red dashed - sim-
ulated spectrum with adjusted inherent filtration). Error bars are plotted but
are small for the sources of error considered

One last exposure was considered for the TLDs, using a filtration of 10 mm of Aluminium, and 5 subsequent layers of filtration by either 0.2 mm of Copper or 1.0 mm of Aluminium, the results of which are shown in figure 3.12. This was to investigate the ability to predict the dose by using the various spectra and their associated photon fluences through much greater filtration than earlier exposures. In both Figure 3.12a & 3.12b the dose predicted by the simulation using the CdTe measured spectrum closely matches the dose measured by the TLDs, whereas the dose from the simulated spectra is much decreased by the level of filtration, similar to in Figure 3.11.

This high level of filtration through 10 mm of Al removes the majority of the lower energies from the spectrum, leaving a much harder spectrum of energies to interact with the TLDs. Since the majority of the discrepancies between the spectra used in simulations were in the 10–40 keV range, these low energy differences become obsolete after significant filtration, and the energy spectra the TLDs are subject to in simulation become fairly indistinguishable. The major difference in the dose here is now due to a difference in predicted photon fluence, since the values used for photons per second was lower in the simulated spectra while higher for the measured spectrum. The simulated spectrum had a much lower fluence set by the ion chamber experiment, as there were many more low energy photons which incur the majority of the observed dose, whereas less low energy photons in the measured spectrum led to a higher fluence to achieve the same dose. This measured simulation provides dose predictions that are within $\pm 10\%$ of the aluminium and $\pm 7\%$ of the copper filtered experiments.
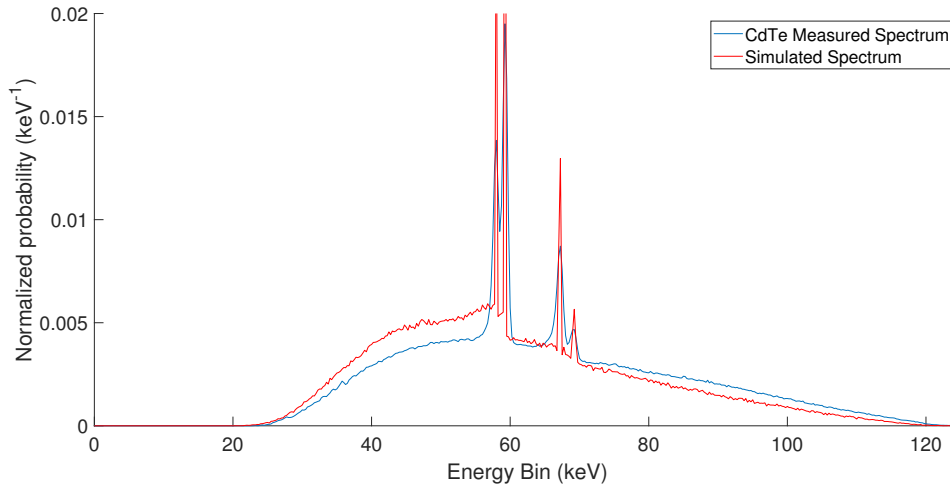
Figure 3.13: The X-ray source spectrum measured by the CdTe spectrometer and the standard simulation, both following a beam filtration of 10 mm of Aluminium

To help validate this, Figure 3.13 shows the spectrum of the spectroscopically measured and the simulated source after being filtered by 10 mm of Aluminium. Although these two spectra do not agree completely, there is much less disparity between these two and the original unfiltered spectra that were used for most simulations and experiments. The sum of the squares of the differences between these two spectra is 76% less than for the original unfiltered spectra. Once again, the main difference between the two distributions is that the intensity of the low energies is reduced in the measured spectrum while it is increased in the higher energies. These spectra effectively visualise the similarity in energy spectra that the experimental and the simulated TLDs are exposed to, and explains the agreement in dose values produced through simulation.

Based on these experimental results, at least for this particular source, strong filtration is required for accurate dosimetry, as the inherent filtration as stated did not provide a satisfactory prediction of the beam output and so is required to be over filtered by further materials. Of course, this filtration sacrifices a large portion of

X-ray flux and as a result, the dose rate is much reduced (around 70%), which, if one is aiming to produce a large dose in a target material, increases the time scale of the experiment.

3.5   Generalising Spectrum Measurements

The results found here are useful not just for the specific source under inspection, but possible to be generalised to other Bremsstrahlung X-ray sources. This is useful for making tests using multiple sources on samples under tests, and being able to predict energy absorption.

A second source was considered for the testing of X-ray energy absorption and deposition of dose. The source was a Thales THX 160 1055, operating in the range from 20–120 kV p and 1.0–10.0 mA. The anode was a Tungsten Target angled at 21°, with both a large and fine focal spot. The diameter of the large focal spot was of 5.5 mm and limited to 4 kW of total power to prevent overheating. The fine focus alternatively had a 1.0 mm diameter focal spot and 0.9 kW limit.

3.5.1   Spectrometry of the Thales Tube

As previously discussed, spectrometry is a powerful tool for dose determination simulations. However, there are drawbacks to the procedure.

A high rate of input photons leads to too many events per second for the spectrometer to count out simultaneously and charge pile up occurs, which generated an improper energy distribution through mislabelling of events. The SAXG source measurement initially suffered from this effect, but with tighter collimation and large separation from the tube output, it could be reduced to a negligible level.

However, the Thales tube was too tightly confined spatially to increase distance in order to reduce the count rate below the maximum measurable count rate. In addition to this, the minimum power output of the tube was not low enough to avoid charge pile up on the detector. Tighter collimation could have improved this, but this led to higher uncertainty in beam quality as it entered the detector, since small angular deviations of the collimator from 90° could filter the beam an unknown amount.
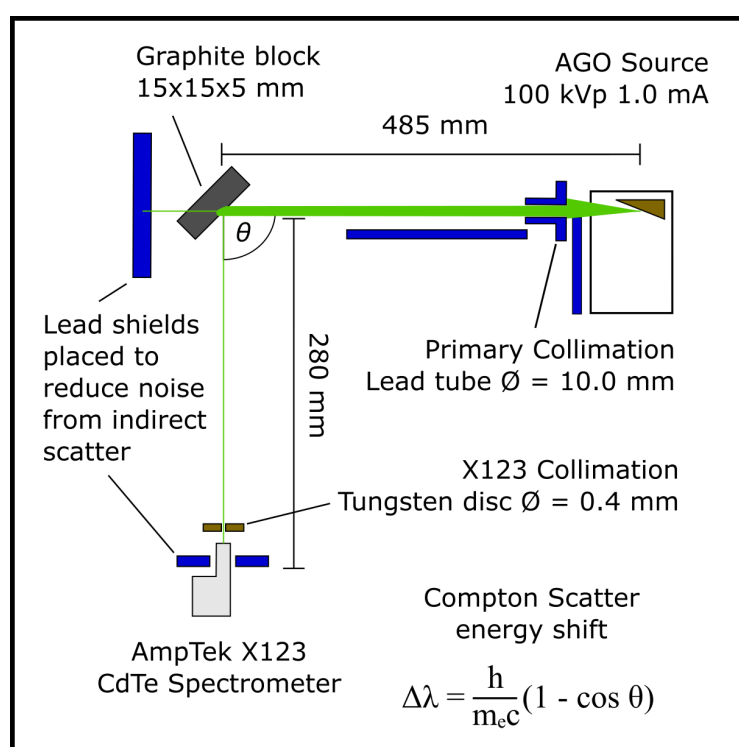
Figure 3.14: The setup used for measuring the spectrum of the Thales THX 160 1055 X-ray source. Blue blocks represent lead sheets used to avoid accepting unwanted backscatter.

In order to reduce the count rate effectively without compromising the X-ray spectrum, it was decided to use a Compton Scatter based spectrum measurement. Figure 3.14 shows a diagram of the setup for this measurement. A thick block of graphite was employed to produce the scattered spectrum, as a homogenous mate-

rial of minimal attenuation, and the spectrum was measured from an angle, θ, of $(90 \pm 1)°$ of Compton Scatter.

Compton Scattering of an X-ray photon does modify the energy of a photon by a certain amount, but it is known and controllable, depending only on the incident energy and angle of scatter. This is seen in equation 3.2, where $\Delta\lambda$ refers to the shift in energy of the X-ray photon by scatter through an angle of θ.

$$\Delta\lambda = \frac{h}{m_e c}(1 - \cos\theta) \tag{3.2}$$

This can be rearranged to obtain the energy shift between the incident photon and the scattered photon, as show in equation 3.3.

$$\frac{E_\gamma}{E_{\gamma'}} = 1 + (E_\gamma/m_e c^2)(1 - cos(\theta)) \tag{3.3}$$

If the angle of Compton scatter is known to be $90°$ $(\pm 1°)$ and the collimation filters any other photons out of the Spectrometer, then equation 3.3 can be used to obtain a Compton Scatter correction factor for each energy bin of the spectrum. Applying this correction, after firstly running the detector correction for Cd and Te escape peaks, to the measured spectrum will obtain the raw spectrum of the tube to a good approximation. This technique has been used with good success before [47], reinforcing the Compton Scatter spectrometry as valid application in this instance.

Shown in figure 3.15 is a demonstration of using a 1 mm 65 kBq [241]Am source as a calibration method to validate the Compton Scatter correction. The Americium was first directly observed by the spectrometer, then placed in line with the colli-
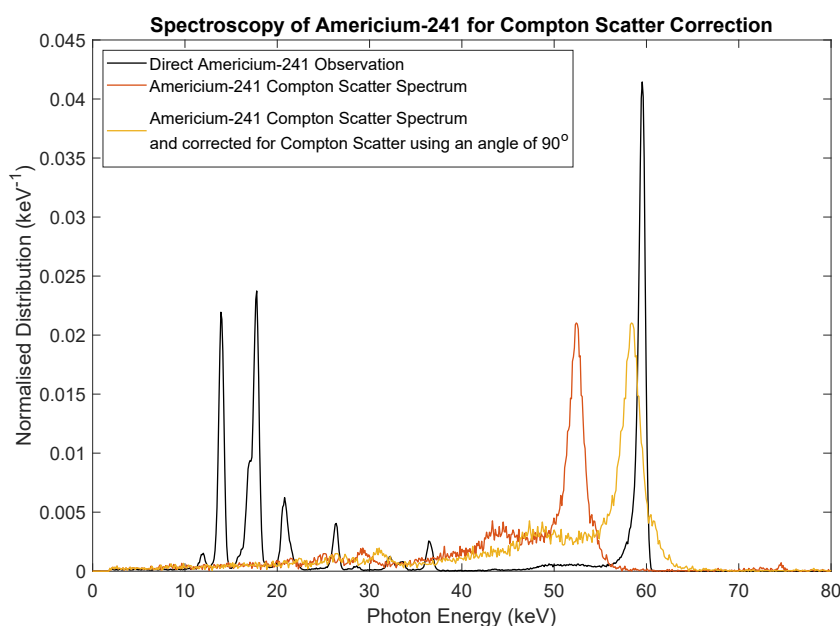
Figure 3.15: A Graph showing the measured emission peak of Am-241 at 59.6 keV, and the spectrum measured through Compton Scatter (CS), to which the correction method is applied

mation setup of the Thales X-ray source and the recorded events subjected to the Compton Scatter (CS) correction. In practice however, this was more difficult as a limited space made manoeuvring the source into the correct position was restricted. This can be seen by the corrected spectrum in figure 3.15, where the correction angle was assumed to be 95° but it is clear this peak is not fully aligned to the direct Am spectrum. Through adjustment it is found that an angle of 100° leads to the spectra aligning. Despite this finding, this is likely due to incorrect alignment for the Am experiment only, while the angle of the tube spectrum measurement was measured to be 90°, so the correction made to the X-ray spectrum initially followed that value.

However, Figure 3.16 displays the action of the CS correction upon the X-ray spectrum, as well as the CdTe correction, previously used in figure 4.3b. The
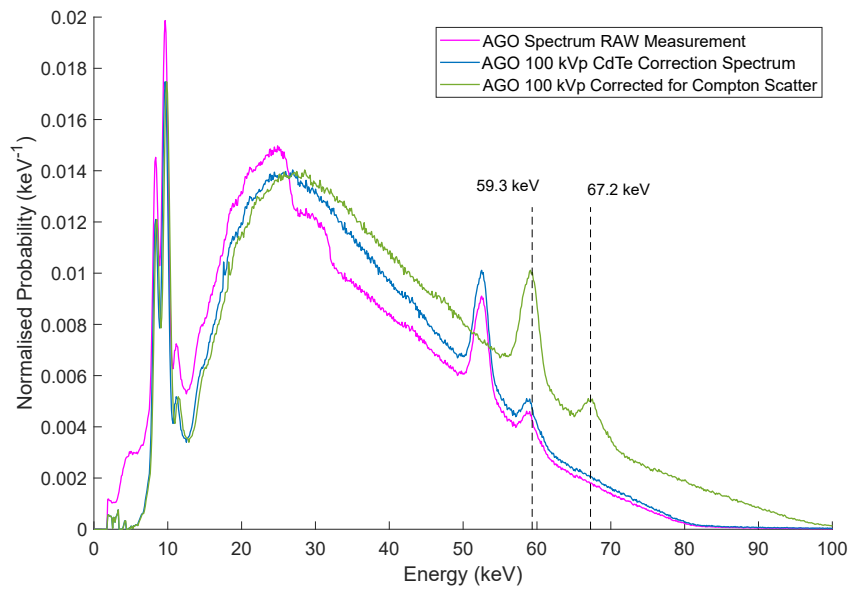
Figure 3.16: A histogram showing the RAW CS spectrum of the Thales tube as measured by a CdTe spectrometer, the spectrum after correction for CdTe escape peaks and finally the action of the CS correction

tungsten K-alpha lines serve as a calibration peak to ensure the alignment of the

the spectrum after correction. Using this as a calibration factor it is possible to

determine that the angle of scattering is more appropriately modelled as 95°.
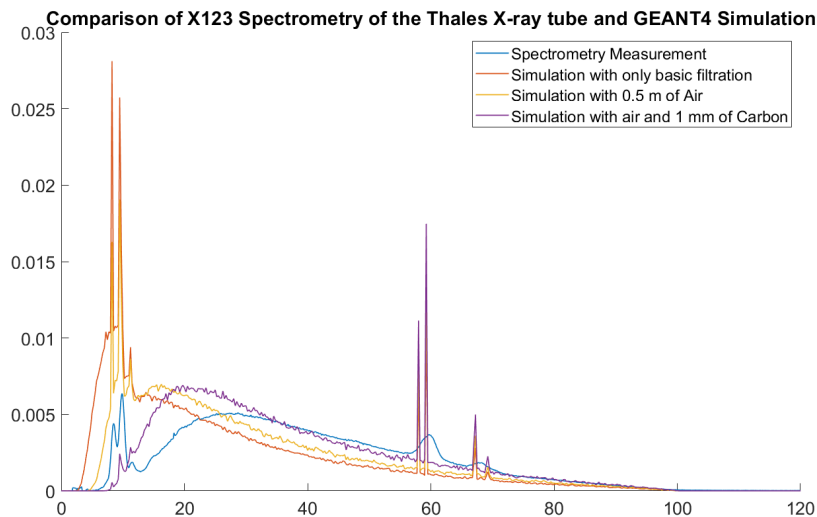
Figure 3.17: Spectra from Compton scatter measurement compared with simulations of the tube using different levels of filtration

Figure 3.17 shows the results. Here, the only way to cross confirm the spectrum between the measurement and the simulation is to take a Compton Scatter based exposure of the source. Since this involves multiple effects acting upon the X-rays; collimation, shielding, scattering effects, the measured spectrum is likely to be less reliable than in the previous case where a direct exposure was taken. Previously the directly measured spectrum was much more accurate in simulation of the beam exposure to TLDs, as the inherent filtration of the source was improperly characterised.
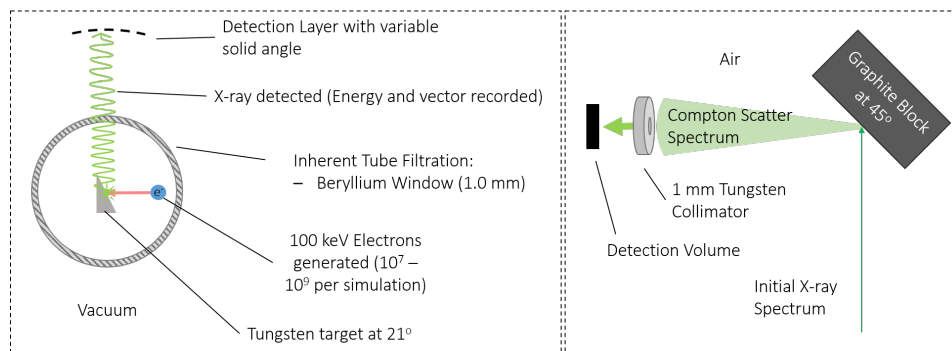
Figure 3.18: A diagram showing the arrangement used for the GEANT4 Simulation of the Compton Scatter Measurement

However, here, the filtration is well known, so it may be more advantageous to consider using the simulation spectrum over the Compton Scatter measured spectrum for energy absorption simulations. In order to then validate the simulation result, various blurring and convolution artefacts can be added to attempt to reach a similar spectrum as found with the spectrometry measurement. This can include subjecting the spectrum to Compton Scatter in a separate GEANT4 simulation.

A diagram of this method is shown in figure 3.18. In the first instance, a beam of electrons was directed at a tungsten target angled at 21°, surrounded by a 1 mm

shell of Be, while all other areas were set to a vacuum, and the photons recorded in a small solid angle of 0.024 sr which was perpendicular to the electron beam. Since the only filtration here was the Beryllium, the spectrum recorded from the first instance here is considered to be the fundamental spectrum just after leaving the X-ray generator. This output spectrum was then taken into a separate simulation, where the photons were directed at a 45° angled graphite block. The detector volume was shielded by a 1 mm Tungsten collimator, as was the case in the experiment, so that only a narrow angle of scattered photons made it to the detector volume. This second simulation was also conducted in a volume of air, with all the distances involved in experiment reproduced, so that the air scatter and filtration was also taken into account.

3.6   Conclusions

It has been shown that use of Monte Carlo (MC) simulation can be used to predict the radiation dosage to small volumes of material in various geometrical configurations, by comparisons with Thermoluminescent (TL) materials. It has been seen that both knowledge of the precise nature of the X-ray spectrum and also the number of photons produced by a source each second is crucial to correctly describing the dosimetry. A reliable model of this X-ray source has been built in the high energy physics simulation software GEANT4 and evaluated with comparison to TL dosimetry, so that future experiments can be simulated in GEANT4 with reliable accuracy ($\pm 10\%$) to determine the energy and dose received.

Although, a failing of the modelling process was found in the inability to pro-

duce a reliable X-ray spectrum for the SAXG 1701 X-ray generator, this method has been shown to produce satisfactory results in previous work [48, 49, 50, 34]. Since the MC model has been proven many times in the past, the failure of this model must be due to either an inaccurate modelling of the X-ray generators internal geometry or an incorrect knowledge of the specific materials and filtration involved below the visible surface of the generator. Measurement of the X-ray spectrum provided a much more accurate description of the source, however, still not entirely correct and this difference is attributed to inconsistencies in the intensity of lower energy photons in the spectrum.

It was subsequently demonstrated that reducing the ranges of the spectrum, through beam filtration, where inconsistencies lie between the model and the experiment is a useful method towards ensuring the reliability of dose predictions by the model. As the low energy photon intensities are most sensitive to small changes in the beam filtration, a heavy filtration effectively reduces their concentration to a negligible amount so that beams of entirely separate initial filtration would coalesce towards the same spectrum. However, when aiming to deposit large doses into target materials, this acts as a hindrance on the time taken to administer exposures, as the dose rate for objects in the X-ray beam is significantly reduced with this filtration.

Chapter 4: Device Simulation, Design and Synthesis

To use $CsPbBr_3$ in experiments for X-ray detection, it must first be synthesised in a reliable manner. However, in order to efficiently exploit the characteristics of $CsPbBr_3$ as a detective medium, the design for its most effective functionality should be decided upon. Furthermore, the parameters used in the design process should depend on values obtained through simulation of the material in an X-ray environment.

Thus it is most advantageous to begin from the process of simulating devices under X-ray illumination and evolve design ideas from there. This allows for a well-informed and performance-justified design process, and helps to understand problems that arise in functionality.

4.1 Crystal Synthesis Methodology

Multiple methods of synthesis have been reported for $CsPbBr_3$ and related perovskites, [51]. These have their advantages and disadvantages as listed in table 4.1.

Bridgman Growth (BMG) is performed through the slow cooling of precursor powders from liquid using a temperature gradient based furnace, and is consid-

ered the benchmark method of production for $CsPbBr_3$, along with many other perovskites. It is a well established crystal growth methodology and has been shown to form high purity single crystals with strong repeatability. In contrast, the production process is both time consuming and delicate, such that many days of synthesis work can lead to ruined batches due to small variations. It also lacks a cheap method of scalability, as the production process is limited to the BG furnace instrumentation.

Method	Advantages	Disadvantages	References
Bridgman Growth (BMG)	- High purity single crystals	- Delicate process - Limited yield - Slow growth period	[52, 53, 54]
(Modified)-Inverse Temperature Crystallisation ((M)-ITC)	- Scalability through repetition - Low cost	- Small crystals formed per step -Thermal control is delicate - High material waste per step	[55, 56] [57, 58]
Anti-solvent Vapour-assisted Crystallisation (AVC)	- Scalability - Low cost	- Small crystallites - Susceptible to impurities	[59, 60, 61]

Table 4.1: Reported successful synthesis methods for $CsPbBr_3$ along with the major advantages and disadvantages

Inverse Temperature Crystallisation (ITC) is a cheaper alternative, that utilises special conditions of some solvents that decrease their solubility at certain higher temperatures, leading to crystals forming from dissolved precursors under a slow increase of temperature. It has also been altered to include repeating the process multiple times on the same crystallite to simply increase the crystals volume, whereby this process is referred to as the (Modified)-Inverse Temperature Crystallisation (M-ITC). Both ITC and M-ITC have the advantage of being much more

scalable, given no limitation on solution volume and there is no large cost of instrumentation or time. However, ITC forms only small crystals in a single mixture and so M-ITC is required to form larger crystals, with each repetition step involving an entirely new mixture of precursor materials, leading to increased material cost.

Finally, Anti-solvent Vapour-assisted Crystallisation (AVC) is similar to ITC however, uses an atmospherically dispersed anti-solvent to gradually reduce the solubility of a mixture in which the precursor materials are dissolved. This is also a low cost, scalable method without the need to consider careful heating of the sample and can be performed at room temperature. This however shifts the importance from temperature control to precursor ratio control, where non-optimisation leads to impure crystal formation with unwanted by-products.

Here the perovskite was synthesised through AVC growth. Following the method described in [61] precursor materials and solvents were acquired from various companies as listed:

- Caesium (I) Bromide (CsBr, 99.9%, Alfa Aesar)

- Lead (II) Bromide (PbBr$_2$, 98%, Sigma-Aldrich-Meark)

- Hydrobromic Acid (HBr, 47-49%, Alfa Aesar)

- Dimethyl Sulfoxide (DMSO, 99.8%, Samchun Chemical)

- Dimeythylformamide (DMF, 99.5%, Samchun Chemical)

- Dicholoromethane (DCM, 99.8%, Samchun Chemical)

The AVC process of growth here is essentially through a slow diffusion of the antisolvent, DCM, into the precursor solution, which then reacts with the solvent,

DMSO, in which the precursors are dissolved and evaporating together, leaving behind the crystal formation.

Initially, portions of powdered CsBr and $PbBr_2$ are weighed out on chemical scale, in a molar ratio of 2:5. These powders are then mixed into a beaker containing DMSO in a suitable amount to ensure full dissolution. For example, the initial test synthesis used $0.127\,g$ of CsBr and $0.539\,g$ of $PbBr_2$ to be mixed with $3\,ml$ of DMSO. These mixtures were then heated to $60\,°C$ and stirred automatically for 1-2 hours until visually clear.

Once a clear solution had been reached, it is recanted into another beaker via a PTFE hydrophobic syringe filter (Saroius, PTFE, $0.2\,\mu m$ pore-size), in order to prevent inhomogeneous crystallisation by removal of any µm sized constituents. It is important to note, care is taken to select an appropriate size for this beaker, as the solutions volume will increase up to twice the original measurement during the crystallisation process. The beaker is then loosely covered with a sheet of Aluminium foil, after which small holes are made into the aluminium sheet to allow gentle ventilation. A second, larger beaker is filled with the antisolvent DCM at approximately 1.5 times the volume of the DMSO to ensure there is adequate antisolvent to react with all of the DMSO. The first beaker containing the ventilated CsBr-$PbBr_2$ in DMSO solution is then placed in the second beaker, partially submerged in the DCM so as not to allow direct contact between either of the fluids.

The larger beaker is sealed using another sheet of aluminium foil and secured on top with a full sheet of Parafilm lab film. It should be noted that Parafilm is susceptible to weakening as a result of exposure to a chlorinated solvent, so it is

used here only as a method to hold the aluminium foil tightly as a seal and so no resultant leakage was observed. The now sealed setup is left in ambient conditions at room temperature for 24-72 hours for the crystal growth to occur.

DCM has a boiling point of 39.7 °C so at room temperature it will continuously evaporate and fill the atmosphere of the beaker. Gaseous DCM will then dissolve directly into the DMSO, precipitating out the CsBr and $PbBr_2$, slowly forming crystallites of $CsPbBr_3$. Depending on the molar ratios of the precursor materials in the mixture, other crystals can form[61]. These crystals are of the form of either Cs_4PbBr_6 and the organic crystal $PbBr_2 \cdot 2[(CH_3)_2SO]$[62], the former of which is a sulphur yellow powdered substance and the latter is a white crystallite. $PbBr_2 \cdot 2[(CH_3)_2SO]$ can however be washed off with DMF. The growth is halted when a significant portion of white $PbBr_2 \cdot 2[(CH_3)_2SO]$ contaminant crystals begin to form.

The crystallites are then removed and placed upon filter paper and connected to a vacuum pump system to be washed with DMF, which removes excess PbBr, DMSO and DCM along with dissolving $PbBr_2 \cdot 2[(CH_3)_2SO]$ crystallites. Finally the cleaned crystals are placed in a vacuum oven at 80 °C for 24 hours to remove the DMF.

At this point, crystals are of 0.1–1 mm length and make up the raw material of the perovskite devices. However, these must be processed into functional shapes in order to be contacted and finally tested.

Through the synthesis process, a variety of perovskite batches were made, their designated name and referral in the text hereafter is shown in table 4.2.

Sample Name and Acronym	Chemical	Description
Test Batch 1 (TB1)	$CsPbBr_3$	Test growth of $CsPbBr_3$ sample 0.127 g of CsBr and 0.539 g of $PbBr_2$
Base Batch 1 (BB1)	$CsPbBr_3$	Mixing at a molar ratio of 2:5; 1.27 g of CsBr with 5.39 g of $PbBr_2$
Base Batch 2 (BB2)	$CsPbBr_3$	Mixing at a molar ratio of 2:5; 5.06 g of CsBr with 21.57 g of $PbBr_2$
Altered Ratio Batch 1 (ARB1)	$CsPbBr_3$ $Cs_2Pb_2Br_5$	Mixing at a molar ratio of 1:1; 20 g of CsBr with 34.5 g of $PbBr_2$
Iodine Batch 1 (IB1)	$CsPbBr_{3x}/I_{3(1-x)}$	Molar ratio about 4:9:1 of CsBr, $PbBr_2$, PbI_2; 1.27 g of CsBr, 4.55 g $PbBr_2$ and 1.03 g of PbI_2 so that x = 0.88
Iodine Batch 2 (IB2)	$CsPbBr_{3x}/I_{3(1-x)}$	Molar ratio about 4:8:2 of CsBr, $PbBr_2$, PbI_2; 1.27 g of CsBr, 3.80 g $PbBr_2$ and 2.06 g of PbI_2 so that x = 0.76
Base Batch 3 (BB3)	$CsPbBr_3$	Mixing at a molar ratio of 2:5; 5.06 g of CsBr with 21.57 g of $PbBr_2$

Table 4.2: A table of all perovskite crystal batches synthesised for experimentation and how much material was used in each solution growth

4.1.1 Growth Results
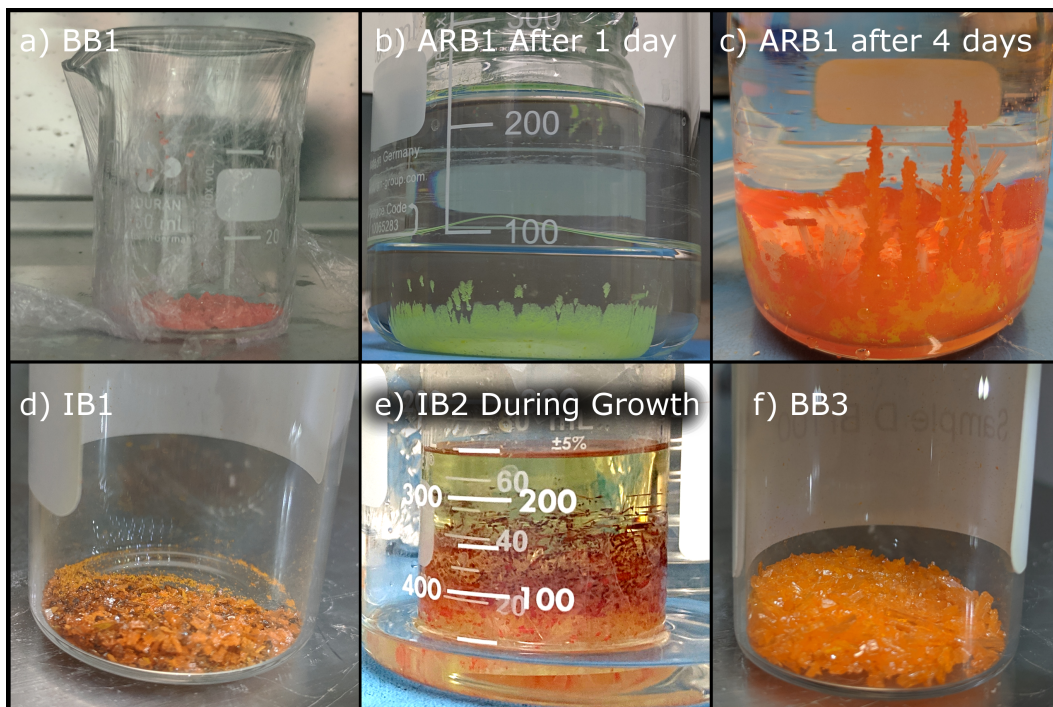
Figure 4.1: Images of batches from table 4.2 during or post growth. a) Base Batch 1 (BB1) post growth b) Altered Ratio Batch 1 (ARB1) when yellow crystals grew initially c) Altered Ratio Batch 1 (ARB1) after 4 days the yellow crystals were complimented with orange growths d) Iodine Batch 1 (IB1) Post growth and cleaning e) Iodine Batch 2 (IB2) during growth process f) Base Batch 3 (BB3) post growth and cleaning

Test Batch 1 (TB1) was to ensure the growth mechanism was working correctly and that the recipe was suitable to this particular lab environment. Only about 300 mg of CsPbBr$_3$ was produced in this instance, so for the next growths it was decided to scale up the ingredients by a factor of 10 and increase the mixing volume.

Base Batch 1 (BB1) grew as successfully as TB1, however, here white translucent crystals of PbBr$_2 \cdot 2[(CH_3)_2SO]$ were observed to be growing along with the CsPbBr$_3$. However, these were washed off with DMF in the post growth cleansing process, so were considered as removed. Base Batch 2 (BB2) was grown with the

aim of maximising the yield from a single growth mix, so the precursors were increased again by a factor of 4 and mixed with 120 ml of DMSO. Fig 4.1 a) shows crystals synthesised from BB1 after processing, and figure 4.2 shows BB2 at the end of its growth process, where the white crystallites can clearly be seen forming.

Altered Ratio Batch 1 (ARB1) was mixed at a 1 to 1 molar ratio of precursors, with the intention of observing the difference in this mixing ratio and possibly increasing efficiency of the growth rate. Initially, it was evident that this was not correctly synthesising crystals of $CsPbBr_3$, as yellow crystallites of Cs_4PbBr_6 were
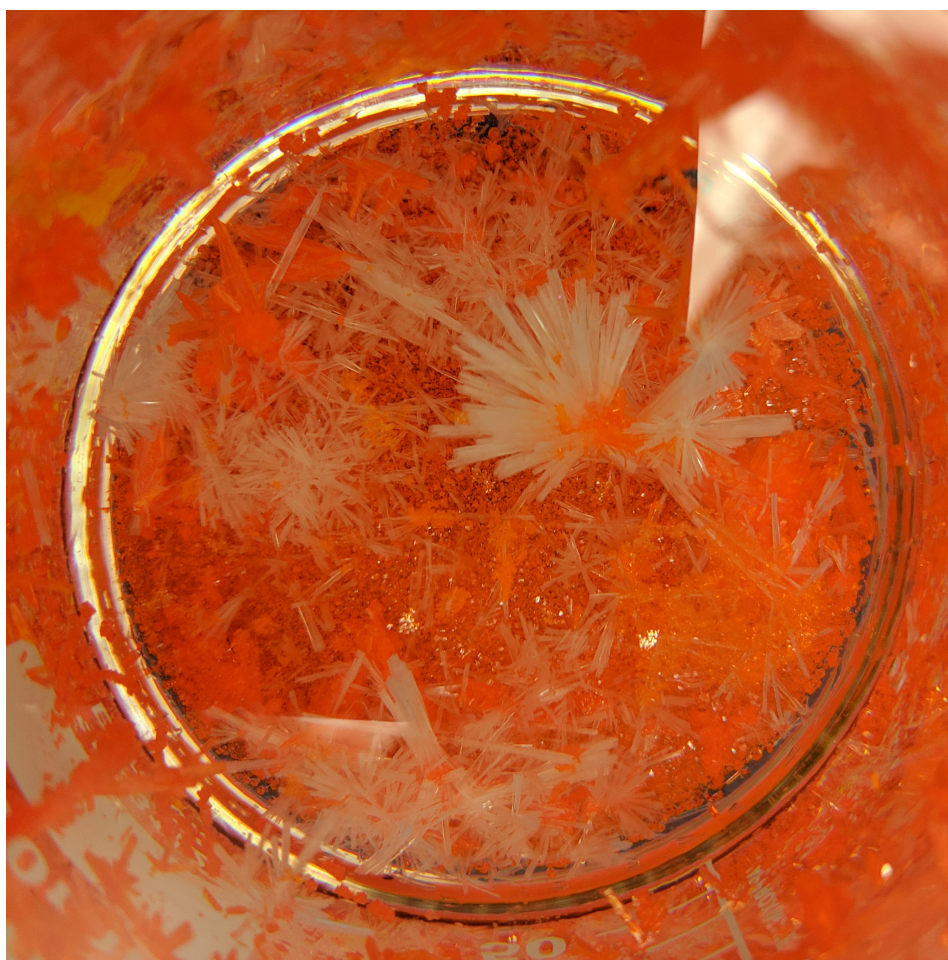
Figure 4.2: Top down view of batch Base Batch 2 (BB2) at the end of growth. Both orange $CsPbBr_3$ and white $PbBr_2 \cdot 2[(CH_3)_2SO]$ crystals are visible.

formed, as shown in fig 4.1 b). Eventually however, $CsPbBr_3$ crystals began to form mixed in with the yellow, shown in 4.1 c). After removal, cleaning with DMF did not remove the Cs_4PbBr_6, as it did the white crystallites. This batch was kept for device synthesis nonetheless as an interesting alternative to the base mixture.

Later, Iodine Batch 1 (IB1) and Iodine Batch 2 (IB2) were grown simultaneously, which are shown in figure 4.1 d) and e) respectively. In IB1 the mixture involved replacing 12% of the molar mass of $PbBr_2$ with 15% of PbI_2, and IB2 used twice that, 30% of the molar mass of $PbBr_2$ being replaced with PbI_2. Assuming $CsPbBr_3$ and $CsPbI_3$ have equal formation rates and even distribution when in solution, this should lead to a crystal structure of $CsPbBr_{3x}/I_{3(1-x)}$, where x = 0.12 and 0.24 respectively. These crystals grew with darker patches mixed amongst the standard orange of the $CsPbBr_3$, indicating a segregated crystal growth. This can be seen in fig 4.1 e).

Finally, Base Batch 3 (BB3) was synthesised following the same methodology as for BB2, which produced a similar batch, though with noticeably fewer white crystallites of $PbBr_2 \cdot 2[(CH_3)_2SO]$ forming. A sample of the post processing crystals is shown in 4.1 f).

4.2 Active Volume Processing Methods

As has been seen in literature [53, 32], single crystal devices of $CsPbBr_3$ are an ideal form to study, as they have a regular predictable structure and testing can be representative of the compound as a whole, and this is reflected in their good performance. Here forming devices out of the small powdered crystals by pressing

them together to form a predefined shape can have many alternative advantages, primarily a much more scalable method and much greater control over the active volume dimensions. It was therefore decided to attempt to test both forms.

4.2.1 Crystal Melt Formation

In order to try to form a single crystal from the perovskite crystallites, it was decided that a suitable method would be through melting and annealing to form a singular crystal lattice, by following the method described by [52]. The melting point of $CsPbBr_3$ had been found to be $567\,°C$ so any container for this crystal formation would have to be able to withstand temperatures up to $600\,°C$ without deformation or phase change. The most ideal material to use here, as is used in general for crystal growth mechanisms was quartz.

The crystallites were ground with mortar and pestle to increase surface area and mixing efficiency. Measures of perovskite powder were then placed into flat bottomed quartz tubes of $8\,mm$ inner diameter and $150\,mm$ length. The quartz tubes were subsequently evacuated using an industrial vacuum pump and simultaneously sealed via glass blowing to form evacuated ampoules. No more than $3\,g$ of perovskite was placed in a single tube so that the material would not be adversely affected by the heat from the glass blowing.

Once sealed, sets of ampoules were placed vertically in a ceramic box furnace. The heating profile was set to follow; 6 hours of continuous heating by $1\,K\,min^{-1}$ up to $600\,°C$, held at constant temperature for 12 hours, and then cooled for another 95 hours at the slowest available rate of $-0.1\,K\,min^{-1}$ until reaching room temperature,

taking a total of 5 days. As mentioned in [63], keeping the perovskite at $600\,^{\circ}\text{C}$ is helpful for reducing inhomogeneities in the liquid perovskite distribution and also protecting against possible inaccurate temperature measurements.

Afterwards, the ampoules were broken via a vice and the solid crystals that formed extracted cautiously. In order to shape these crystals into functional devices, the crystals were cut to shape using a wire saw. The crystal structure was found to be partially unstable and vulnerable to crumbling, especially to forces of torsion. To reduce the damage to the crystals in cutting, the lengths to be cut were submerged in melted paraffin and left to cool, while the wire saw blade speed and pressure was lowered to minimal values, taking 5 minutes to cut each slice. The paraffin acted well to protect the crystal and absorb some of the vibrational energy of the blades friction, as well as assisting in cooling. $CsPbBr_3$ is soluble in water, so the coolant used to maintain the blade and cutting efficiency was propan-2-ol, as it has a relatively low dipole moment.

Once cut, the crystal slices were retrieved by melting the paraffin, and then residual paraffin film evaporated by brief heating to $400\,^{\circ}\text{C}$ with a soldering iron.

4.2.2 Compressed Powder

Pressing the powder into compressed pellets required much less processing than through melt crystallisation. Some selection of the solution grown perovskite crystallites were also ground up via mortar and pestle, while others left in their initial state, to inspect the difference in response from pellet composition. A diagram of the compression method is shown in figure 4.3a.
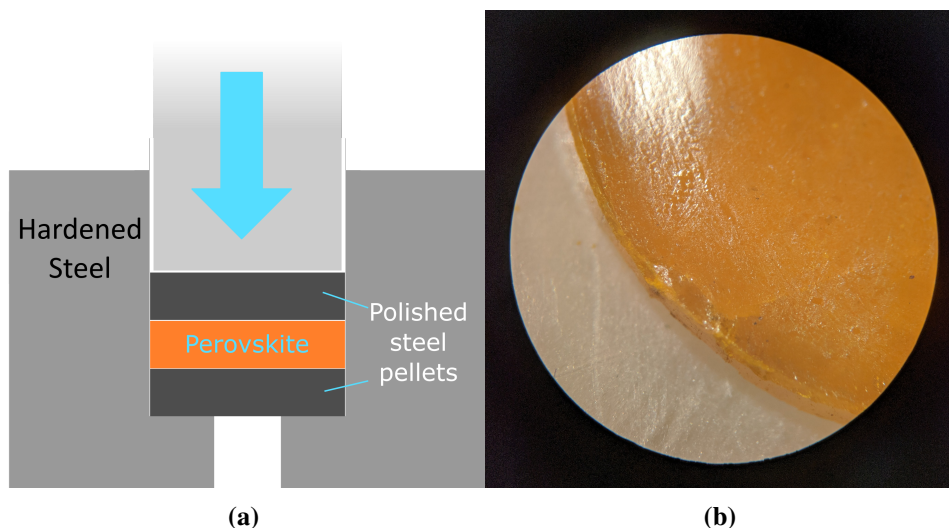
Figure 4.3: a) A diagram showing the pressing method between two polished steel plates to create the perovskite pellets, b) A microscope image of the surface of a perovskite pellet after pressing

The goal was to synthesise 1 mm thick pellets, so with a diameter of 8 mm and knowing the density of $CsPbBr_3$ to be $4.55\,\mathrm{g\,cm^{-3}}$, the mass used should be 229 mg. However, in early tests, it was noted a proportion of the mass, around 10 to 20%, was lost through the pressing technique either leaking out or becoming stuck to the dye, so it was decided to overestimate the mass by 20% to ensure the pellets were thick enough for experimentation. So a measure of 300 mg of perovskite crystallites was used to form each of the pellets.

Pellets were formed by a pressure of 784 MPa. This was found to be a reliable pressure that formed strong pellets, without risking too much deformation or breakage of the pressing setup. However, through repeated use, the sandwiching plates slowly deformed to feature a central depression from the pressing action and so it was decided to reform new pairs of plates after 10 presses at a time.

4.3 Photoluminescence Spectroscopy

Analysing the materials pre and post processing is key to understanding the influence of the methodology. Here, a useful technique for deciphering the perovskite material composition while also looking for the presence of contaminants, is Photoluminescence Spectroscopy (PL).

PL is a process via which a monochromatic laser of photons of a known wavelength anywhere between Infrared-Ultraviolet are directed upon the surface of, or transmitted through, a semiconducting sample. The photons will be absorbed by the sample, through which electrons will be excited from the valence band to the conduction band. The excited electrons then lose energy through interactions with the lattice, either by Coulomb scattering or phonon interaction, and decay to the bottom of the conduction band. Once there, the only further way to lose energy is through recombination with a hole in the valence band, which causes the emission of a photon with energy given by the band gap of the semiconductor.

This process is a form of fluorescence, and observation and spectrometry of these fluorescence photons can then be used to infer the energy of the band gap of the material. It can also reveal the presence of multiple band gaps, implying multiple configurations, compounds or impurities present in the material. The intensity of the emission can be used to infer the quality of the semiconductor in that it provides a high density of excitable sites for the use as a semiconductor.

Here, PL was performed on multiple sets of perovskite samples to learn about the bandgap in the material and the purity, while also looking for changes brought

about through processing. A Xenon laser operating at 415 nm was used to gener-
ate the absorption photons, focused upon a set of samples as shown in table 4.3.
The emission peaks observed from these samples were mostly monomodal with di-
minished bimodal peaks at $< 1\%$ intensity. The FWHM can be translated into an
estimation of uncertainty [64] via the equation:

$$FWHM = 2\sqrt{2\ln 2}\sigma \approx 2.3458\sigma \tag{4.1}$$

Through this equality, the standard error of the peak energies is between
± 0.07–0.04 eV, scaling with the FWHM.

These bandgap values reflect values obtained in literature (2.32–2.43 eV)
[28, 65], which helps to assure that these samples are not improperly produced.

Batch Name	Sample Description	Observed Peak (eV)	FWHM (eV)
BB1	Small Crystallites	2.35	0.17
BB2	Single Crystallite	2.35	0.11
BB2	Pressed Pellet	2.36	0.15
BB2	Single Crystallite	2.33	0.12
IB1	Small Crystallites	2.37	0.15
IB1	Single Crystallite	2.33	0.13
IB1	Pressed Pellet	2.35	0.13
BB3	Furnace Melt & Cut Pellet	2.34	0.12
IB1	Furnace Melt & Cut Pellet	2.37	0.12
IB2	Furnace Melt & Cut Pellet	2.36	0.13
ARB1	Furnace Melt & Cut Pellet	2.36	0.10

Table 4.3: Batches of perovskites in various forms, their emission peaks found through
photoluminescence and the FWHM of the peak observed.

Knowledge of this bandgap is useful for estimating the charge generated from radiation energy deposition, which will be further discussed in chapter 5.
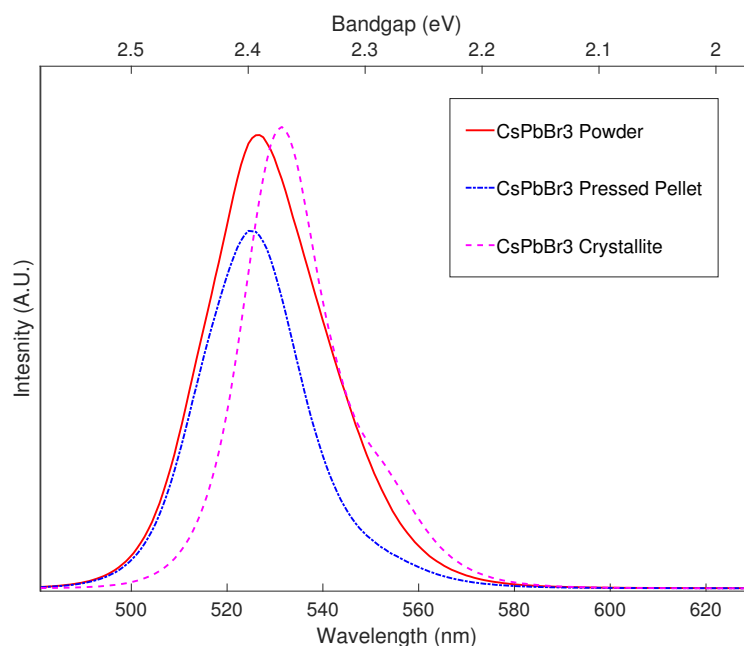
Figure 4.4: A graph of the PL response of 3 separate forms of $CsPbBr_3$, as a ground powder, a fully processed pressed pellet and as a crystallite with no modification since growth. Wavelength is shown at the bottom while photon energy is shown at the top.

Figure 4.4 features data taken from the same production batch but after different levels of processing, i.e. unchanged crystallite, ground powder and a final pressed pellet. What can be observed is a lack of any major shift as a result of this processing, with the bandgap shifting upwards by only $0.03\,eV$. There is also a second mode visible within the crystallite response at 550–560 nm, which could be attributed to impurities such as PbO or CsO, however this mode does not show up after further processing.

The resilience of the bandgap is further observed in figure 4.5, where the peaks of each emission spectra of all of the furnace melt and cut samples are plotted vs the relative intensity between them. Here the peak values vary only by values much
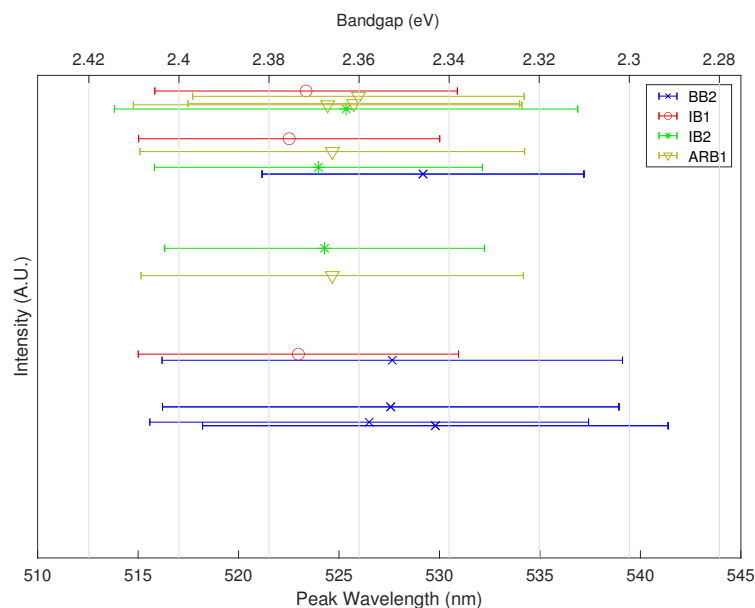
Figure 4.5: A scatter plot of the peak energies and relative intensities taken from PL measurements on completed pressed pellet samples with error bars plotted according sigma value taken from the FWHM

less than the error in the samples found from equation 4.1. These samples have each been fully melted and cooled to form crystals and yet continue to show the same region of bandgap energy.

Figure 4.6 shows PL data acquired of 3 crystallites from the Iodine doped batch, nominally $CsPb(Br_{0.8}/I_{0.2})_3$. Each distribution is vastly different between samples, with the three emission peaks of the crystallites being present in each sample. This reflects the visual difference between these samples that feature discolourations towards darker red and brown while also containing the bright orange of standard $CsPbBr_3$. This indicates inhomogeneity of the $CsPbI_3$ within $CsPbBr_3$ along with what is perhaps an interstitial state between the two compounds.
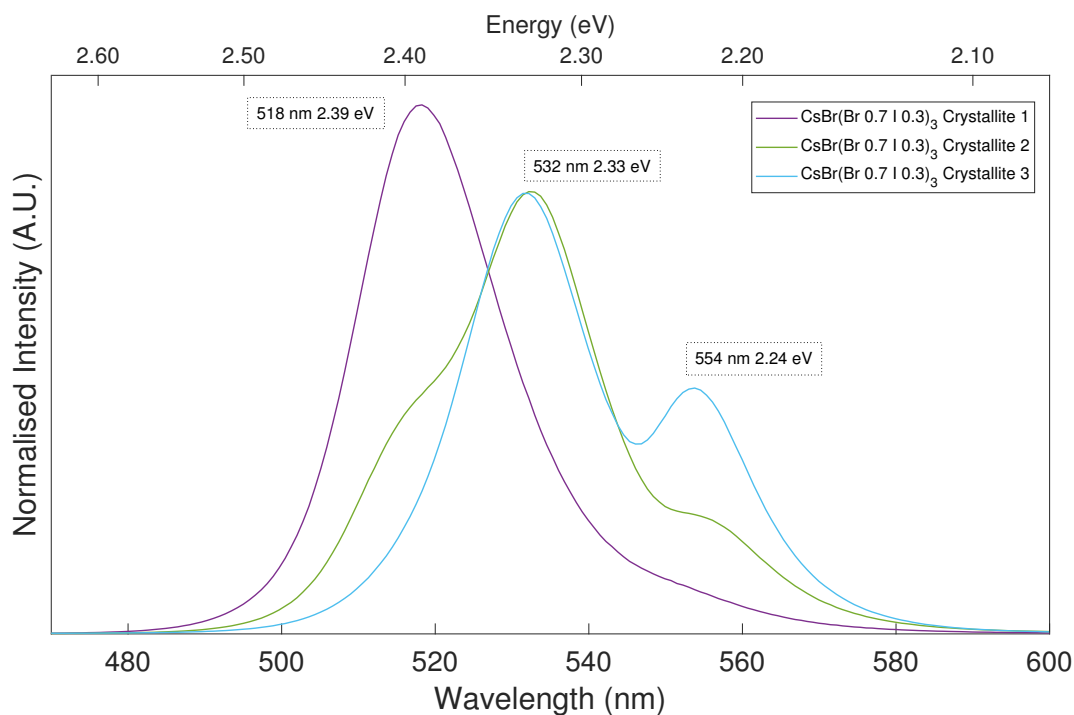
Figure 4.6: PL Data of 3 crystallites taken from batch IB2, with their respective prominent peaks indicated in nm and eV

4.4 Samples Prepared

Over the course of the experimentation, multiple samples were prepared with variations between them.

Generally, there were two generations of samples; the initial set, described in table 4.4, and the final set, described in table 4.5. The initial sample set was much more experimental, where parameters were highly varied to search for successful synthesis and processing methods, for example growing a batch using a 1:1 mixing ratio, which yielded yellow crystals with a high proportion of $Cs_2Pb_2Br_5$. The final set was prepared using the synthesis parameters that provided the best results in order to attempt to make optimised devices for X-ray sensing, along with interesting leftover material from previous sets.

Sample Name	Acronym	Description
First Sets		
Test Pellet 1	TP1	First iteration making a pellet from pressing, circular 10 mm across and 1.25 mm thick, with
Test Pellet 2	TP2	Second iteration, similar to Test Pellet 1 circular 10 mm across and 1.25 mm thick, with
Furnace Crystal	F1A	The first produced sample in a furnace melt ampoule, forming a polycrystalline sample
Pressed Pellet 1	PP1	Single 500um Pixel
Pressed Pellet 2	PP2	3x3 500um Pixels
Pressed Pellet 3	PP3	Connected with Silver Powder
Pressed Pellet 4	PP4	Connected via soldered contacts
Crystal Shard	CS1	A shard of recovered crystal from a furnace melt that appeared to be a single crystal

Table 4.4: Table describing the first sets of devices synthesised for testing

Sample Name	Acronym	Type	Description
Final Sets			
Sample 1A	G1A-Br	Ground $CsPbBr_3$	302.3 mg from batch BB3
Sample 1B	G1B-Br	Ground $CsPbBr_3$	300.3 mg from batch BB3
Sample 1C	G1C-Br	Ground $CsPbBr_3$	299.6 mg from batch BB3
Sample 1D	G1D-Br	Ground $CsPbBr_3$	301.7 mg from batch BB3
Sample 1E	G1E-Br	Ground $CsPbBr_3$	304.9 mg from batch BB3
Sample 1F	G1F-Br	Ground $CsPbBr_3$	299.3 mg from batch BB3
Sample 1G	G1G-Br	Ground $CsPbBr_3$	300.8 mg from batch BB3
Sample 2A	F2A-Br	Furnace $CsPbBr_3$	1069 mg from batch BB2 after furnace treatment
Sample 2B	F2B-Br	Furnace $CsPbBr_3$	305.1 mg from batch BB3 after furnace treatment
Sample 3	F3-Mix	Furnace $CsPbBr_3$	299.5 mg from batch ARB1 after furnace treatment
Sample 4	F4-I	Furnace $CsPb(Br:I)_3$	228.0 mg from batch IB1 after furnace treatment
Sample 5A	G5A-I	Ground $CsPb(Br:I)_3$	310.0 mg from batch IB2
Sample 5B	G5B-I	Ground $CsPb(Br:I)_3$	299.0 mg from batch IB2

Table 4.5: Table describing the final devices after refinement for testing

Sample	Mass (g)	Diameter (mm)	Thickness (mm)	Density ($\mathrm{g\,cm^{-3}}$)
Errors	±0.001	±0.01	±0.01	±0.02
G1A-Br	0.277	8.80	1.09	4.18
G1B-Br	0.278	8.85	1.08	4.18
G1C-Br	0.283	8.84	1.10	4.19
G1D-Br	0.269	8.93	1.10	3.91
G1E-Br	0.273	8.81	1.11	4.04
G1F-Br	0.261	8.78	1.07	4.02
G1G-Br	-	-	-	-
F2A-Br	-	-	-	-
F2B-Br	-	-	-	-
F3-Mix	0.278	8.85	1.26	3.59
F4-I	-	-	-	-
G5A-I	0.250	8.86	1.02	3.96
G5B-I	0.257	8.86	1.01	4.12

Table 4.6: Table of pressed pellet physical properties for the final batch measured prior to contact deposition. Samples with no data are those that failed to be fully processed and thrown out

4.5 Device Designs

In order to properly quantify and validate the functionality of a new material such as $CsPbBr_3$ it should be tested in such a way to compare directly to the current industry standards, along with similar materials under research. To test a material, a device must also be designed with a variety of operational modes to test for a broad application of techniques, e.g. large contacts, pixels and channels.

When testing a new material in the realm of X-ray detection, it is both important to compare that materials performance against current standards as well as
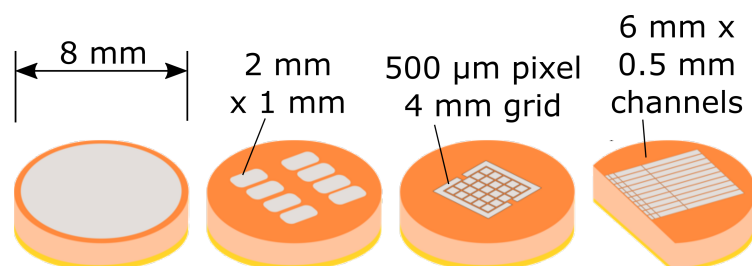
Figure 4.7: Diagram showing the shaping of the different contact designs and the pellet thickness of the perovskite Devices. Pellets are 8 mm diameter and contact dimensions are shown, where the channels are separated by increasing select distances

considering new possible functionalities that open up when considering the materials unique qualities. $CsPbBr_3$ has a significantly higher attenuation coefficient than the lighter industry standards such as Si, α-Se, CdTe, and is comparable to materials currently under research such as TlBr.

This attenuation property allows the process of specification to consider multiple design strategies. A shorter mean transport range of photons means that charge carrier distribution will be more finely concentrated. This can be exploited in multiple ways, such as by creating smaller pixels, allowing for a higher resolution 2D image, or thinning the absorbing channel layer, allowing for greater electric field density or lower voltage operation.

Various designs were considered through the iteration of the project, starting from the simple method of contacting as much of the sample as possible and moving to more heavily controlled and experimental designs, as shown in figure 4.7. Initially, devices were of a simple contact method, using the entire surface of $CsPbBr_3$ samples as contact planes to extract generated charge. This acted as a proof of concept method to ensure the devices were responding predictably and the experimental set up was functional. Following on from this, devices were manufactured
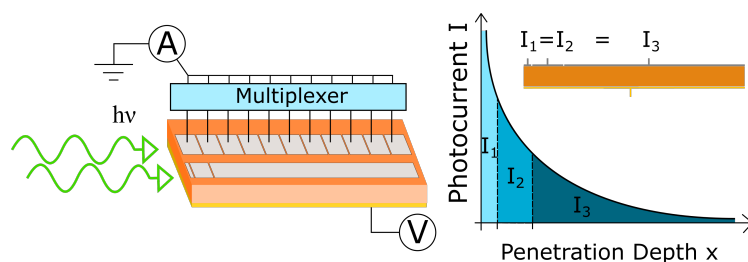
Figure 4.8: A diagram showing the intended functionality of the lateral pixel readout method. X-ray photons would enter from a lateral direction and generate photoelectrons at positions within the material which would then be read out be charged contacts above these sites. A multiplexer would be used to discern the signal being generated by each contact. The pixel contacts could be designed either with equal width and homogenous, or with variable length to try to optimise the current read out by each according to the radiation energy, which is shown in the right part of the figure.

with smaller contact area to observe the change this made in the device response. At this point, only pressure based clips or soldering was used as a method to contact these devices, as the investigation was less focussed on optimisation and more on testing feasibility.

An experimental contact design was considered also, shown in the last drawing from figure 4.7, where the contacts are more in the form of gradually lengthening channels. The proposed functionality of this device is, as shown by figure 4.8, that the X-ray photons enter from an exposed side of the perovskite and their photogenerated charge is read out to these channels, placed perpendicular to the beam path, depending on how deep within the perovskite the charge carriers are generated. Since the radiation penetration depth is proportional to the photon energy, measuring an increase in photocurrent at separate contacts would correlate to different photon energies. If taken in an array, this would theoretically provide a multi-modal set of X-ray images that inspect different ranges of the energy spectrum of the beam.

Moving on from basic designs, it was decided contacts should be optimised

for performance of the charge carrier collection efficiency. An ideal device would form a natural Schotkey junction by using materials with variable work functions to control electron hole transport mechanisms. However, CsPbBr$_3$ has a relatively high Fermi level of 3.95 eV [66], and as such it is difficult to find a metal contact material that is unreactive and of a lower work function to create a Schotkey diode device. In the interest of working towards this effect, thermally evaporated pixels of silver or gold contacts were utilised on the top surface of perovskite samples, as has been conducted in [53].

Gold and Silver are useful contacts in opposition to one another as their work functions are 5.45 eV and 4.26 eV respectively [67, 68], leaving a large disparity of 1.26 eV, to try to ensure a preference of direction for the charge carriers in use.
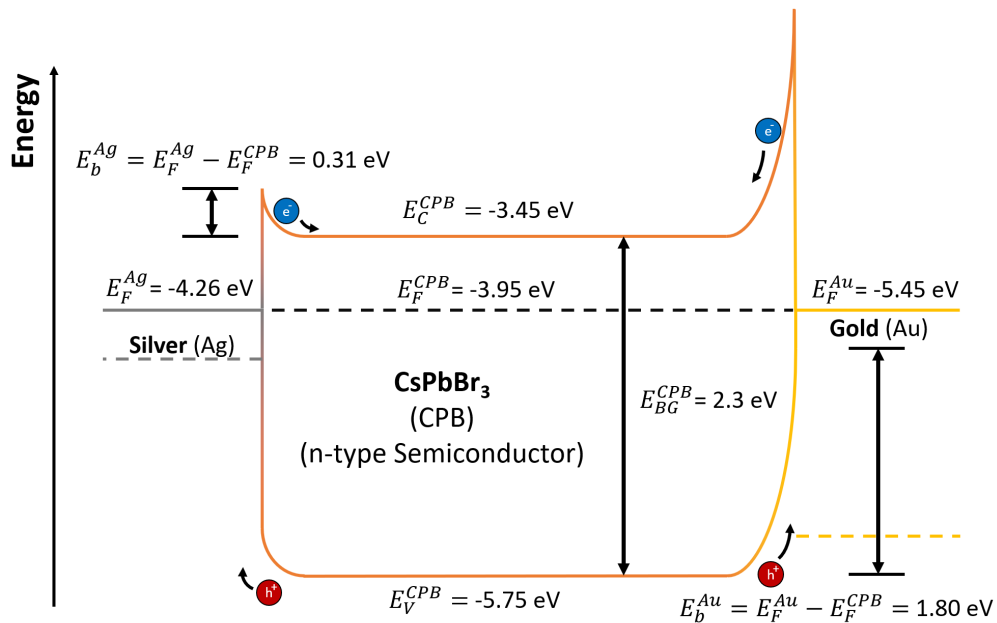
Figure 4.9: Energy Band Diagram for CsPbBr$_3$ in contact with Gold and Silver, showing the band bending at the interfaces as a result of the contact with each metal, CsPbBr$_3$ values obtained from [29]. Electrons and holes are drawn at boundaries to show their preferential direction

Figure 4.9 is an analysis of the band bending that would occur at the interfaces of the perovskite with gold and silver. Here it can be seen that, since the work function of both metals is greater than the Fermi level of CsPbBr$_3$ (E_F^{CPB}), the band bending at both ends is upwards in energy, meaning that there is a certain energy barrier to escape for an electron sitting at the bottom of the conduction band. However, this energy barrier is much lower towards the silver contact, meaning this device architecture should still show a preferential flow for negative charge towards the silver electrode and positive charge toward the gold electrode. Also, given that the depth of the depletion region is proportional to the square root of the difference in energy Fermi level [66], the region near the gold contact will extend more deeply within the perovskite than for the silver contact. This means that if an electron-hole pair were to be generated within this region, close to the gold contact, the hole would move to the gold and contribute to the readout signal without requiring a bias voltage to attract it. However, the electron counterpart would require a bias voltage to make it over the energy barrier at the silver electrode. Nonetheless, some positive signal should be observed from X-rays under 0V bias.

In general, these energy level values should be considered approximations as they can change based on the unique structure and composition of each instance of a material, so should not be considered as exact calculations but rather guides for the physics processes underlying the operation of these devices. Analyses of I-V bias curves of devices can offer insight into how accurate these predictions are. A prediction on what a typical I-V curve for this device design would look like is shown in figure 4.10. Where the silver contact is used as the control electrode,
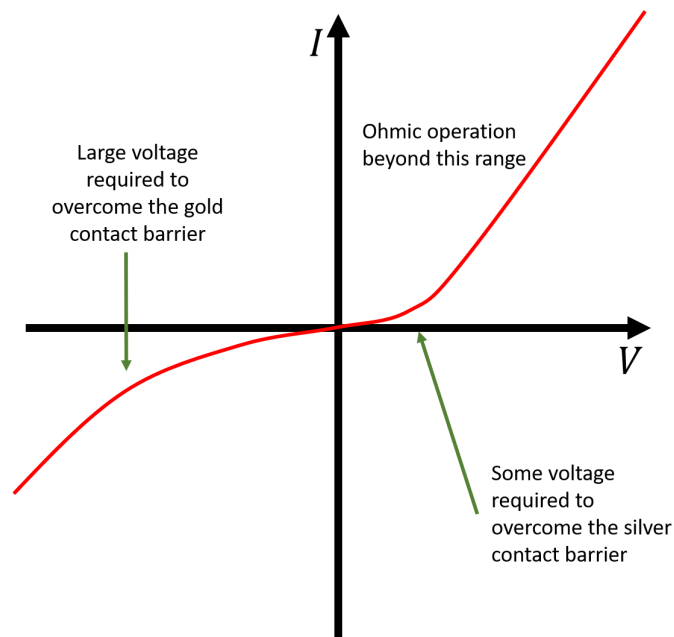
Figure 4.10: An approximation of how an IV curve for this Ag/CsPbBr$_3$/Au device would manifest

going from $0\,V$ to high voltage, it would be expected that electrons would flow towards the silver contact and require a small boost to overcome the barrier, which is seen in the sharper curve that then becomes ohmic at higher voltages. Going from $0\,V$ to high negative voltages would show much less charge transmission at first, as electrons would be held at the gold contact, which would slowly increase to become ohmic over a relatively large voltage range, essentially a very gentle version of a breakdown current as seen in diodes.

4.5.1 Evaporation Mask Design

For more intricate surface contact designs, the thermal evaporation with masks was used as a material deposition technique. There are multiple advantages to this as it allows for bespoke high resolution (up to 25 µm) contact design to be directly

deposited onto the material surface, while also tuning the thickness of the contacts to between tens and hundreds of nm, ensuring very weak and known interference with the X-ray beam.

4.5.1.1 First Evaporation Mask Design

The first mask design employed two sections, labelled MA and MB, which are shown in 4.11 and 4.15 respectively. MA is a set of 4 5x5 pixel arrays, with varying pixel pitches of 500 μm, 200 μm, 100 μm and 50 μm. Each array is surrounded almost entirely by another section, which acts to form a guard ring for modulating the electric field of the pixels, the gaps are included as they are required by the mask to hold the rest of the pixel array up. The separations between each pixel and various other measurements are set to be 30 μm as this was the lower limit the mask manufacturer could offer with precision. These pixels are designed to be contacted via wire bonding on to the perovskite chip.

MB, the second section of the mask, is designed to create channels of contact that are of variable length. As discussed earlier in this section and shown in figure 4.8, the aim is to create channels that will have a photocurrent readout equivalent between all three for a certain mono-energetic beam of X-ray photons. This implies that the channel lengths should become exponentially longer as the X-ray beam is exponentially penetrative, according to equation 2.2 and so electron-hole pairs are generated in an exponential distribution throughout the material.

The penetration depth varies with the energy of a monoenergetic beam, so areas of equal charge generation will be different lengths depending on this energy. Figure 4.12 shows the results of a GEANT4 simulation where monoenergetic X-ray
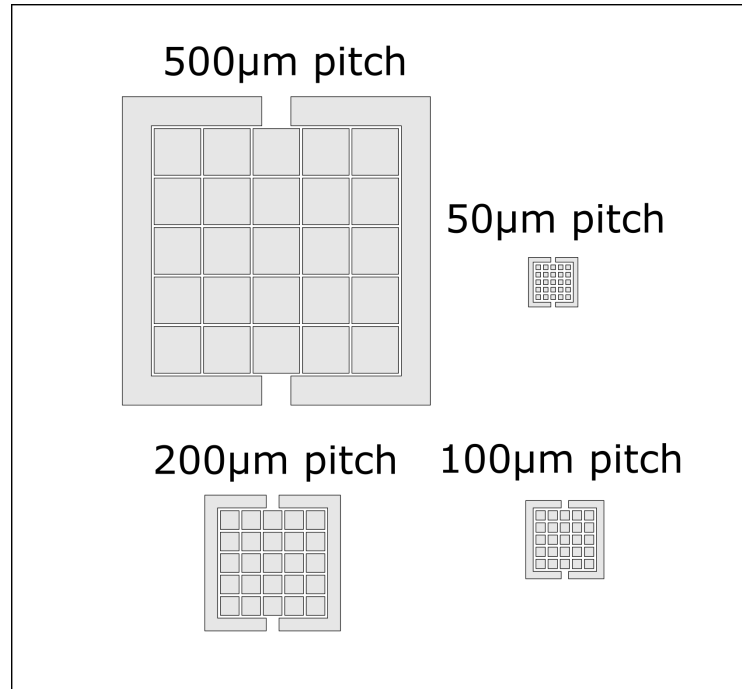
Figure 4.11: A diagram of the design of the pixelated part of the evaporation mask used to deposit silver coatings to the surface of the perovskite pellets, the complete measurements are shown in 8.2

photons of energies 10–120 keV are directed through a 8 mm thick $CsPbBr_3$ crystal, of single crystal density ρ =4.55 g cm^{-3}. This simulation was 1 dimensional in that it only considered the z value for the depth of photons, and the crystals x and y extents were set to be large (1 m) approximating an infinite crystal plane. The 8000 µm of material was divided up into 800 layers 10 µm thick. The total energy deposited across all layers was summed up and then the set of layers were divided into three divisions. Each division represents a third of all the energy deposited in the crystal, with the final third representing up to 99.9%, as 100% absorption is not guaranteed.

From the simulation it can be seen that the depth of energy penetration in the $CsPbBr_3$ varies from as low as 150 µm at 10 keV and above 8000 µm at 120 keV.
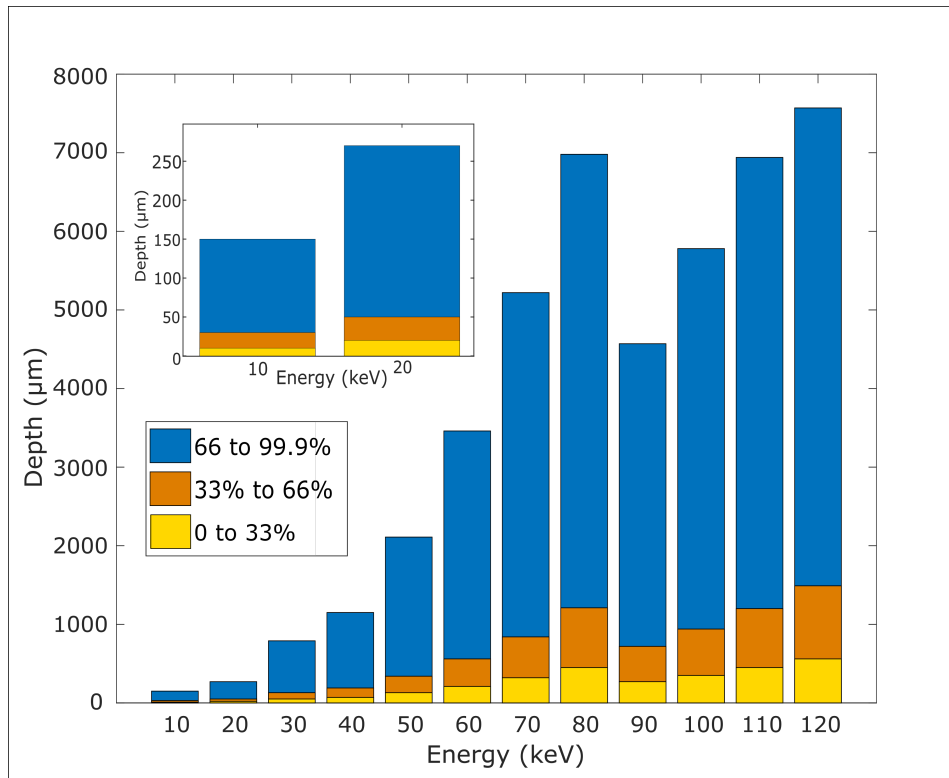
Figure 4.12: Bar chart showing a simulation of the charge deposition distribution of monoenergetic beams of photons from 10 to 120 keV and divided into thirds, where yellow is depth at which the first third of charge is deposited, orange is the second third and blue is the last third (more specifically 66.6% to 99.9%, as 100% absorption is much longer for high energies)

There is a dip in the penetration depth between 80 and 90keV due to the K-edge of the Pb in the material. As energy increases, not all of the beam is absorbed by the material. This is shown in 4.13, where it can be seen that although absorption is never 100%, it never drops below 99% when the energy is 120 keV or below for a thickness of 8 mm.

To test this measurement scheme, various channel lengths were chosen as lengths of interest by using lengths dictated by figure 4.12. 40 keV, 60 keV, 85 keV and 90 keV were chosen to be tested as part of the devices, and their depth profiles are shown in 4.14. 40 keV was chosen as it was the lowest energy with a reasonably
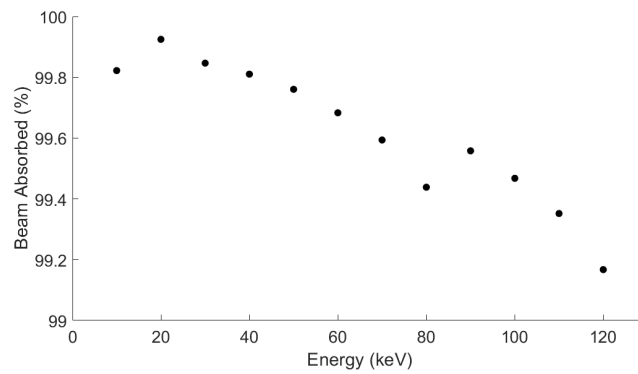
Figure 4.13: Percentage of the total energy of the beam which was absorbed in simulation by the CsPbBr$_3$ crystal for each energy in steps of 10 from 10 to 120 keV
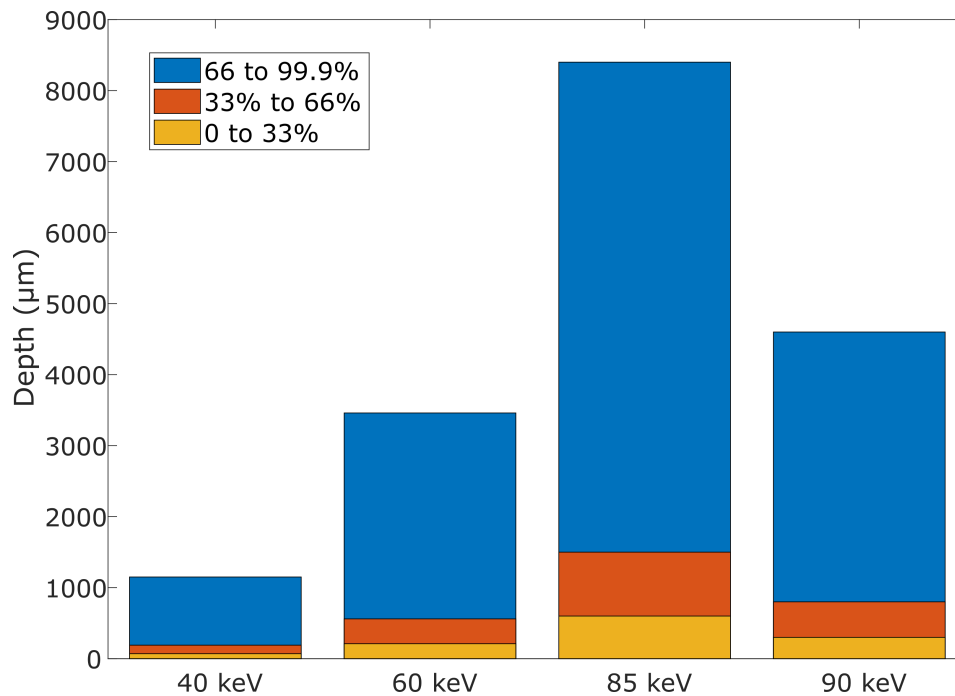
Figure 4.14: Bar chart showing a comparison amongst the selected penetration depths for consideration in experiment

reproducible width to the first division and the 60 keV as a good comparison with 40 keV. 85 keV and 90 keV profiles were chosen because they are either side of the absorption edge of Pb, such that the 85 keV penetration profile would end up having the same depth as an 110 keV beam, while the 90 keV would have the same depth as a 66 keV beam.
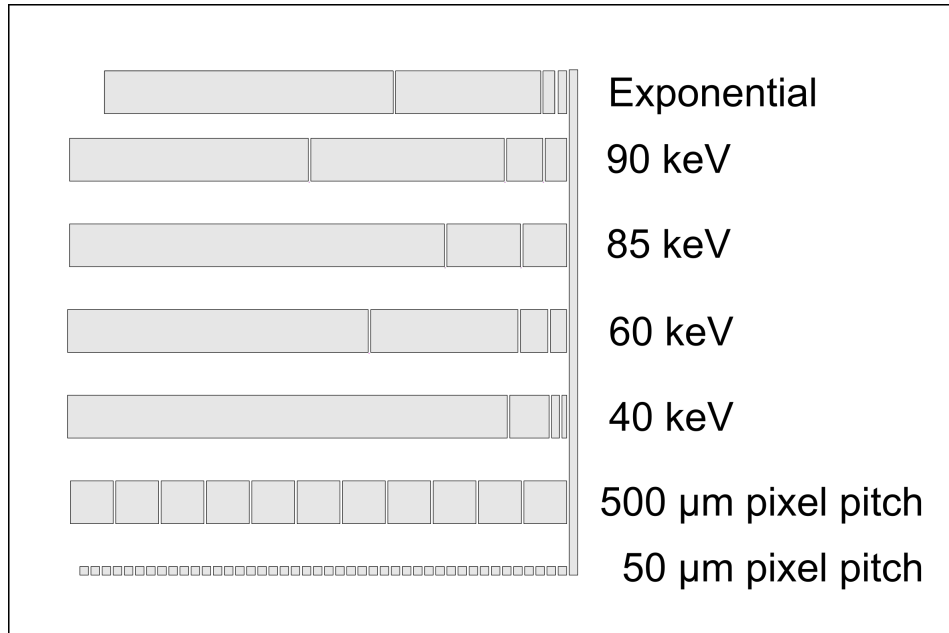
Figure 4.15: A diagram of the design of the channelled part of the evaporation mask used to deposit silver coatings to the surface of the perovskite pellets, the complete measurements are shown in 8.3

Figure 4.15 shows these channels labelled as they are added to the evaporation mask, along with 3 others. The first, labelled Exponential is a more general approach of simply separating channels by an exponential increase, starting from 140 µm and increasing each subsequent channel by a factor of *e*. The final two additions are using simple pixels at set 500 µm and 50 µm, to determine how much of the signal produced by experimentation on the other channels can also be interpreted or inferred from these pixel signals.

This mask was manufactured by Veco Precision through electroformation of Nickel to a thickness of 20 µm. This was then used in an evaporation chamber to pattern the surface of the samples with silver contacts, each sample having to be deposited one at a time. 14 samples were patterned before the mask broke through adhesion to a sample.

4.5.1.2 Evaporation Mask 2
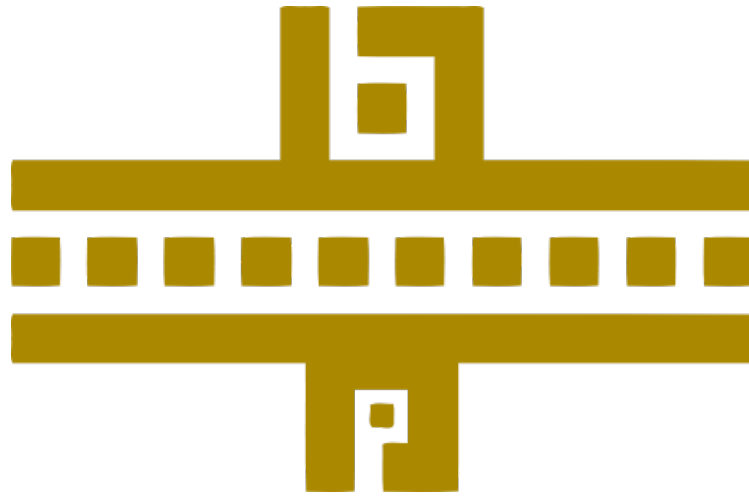
Figure 4.16: A diagram of the second pixel mask design, where gold sections mark where the contacts are deposited.

Later, a second mask design was used for contact deposition. This second design modified the pixel array to instead be a single row with guard rails either side. This design aimed to reduce the high detail and complexity of the previous design, so that it could be manufactured more easily. This design is shown in figure 4.16.

The mask here aimed to deposit only a single line of 10 pixels, each 500 μm square, and flanked on either side by long contacts to act as guard rails for the biasing of the central pixels. On the outside of this area were also two separate single pixels, one 500 μm and the other 250 μm, each almost entirely surrounded by a continuation of the guard rail contacts. Ideally, the guard rails on either side of the pixels will absorb most of the charge surrounding, but not under the pixel. However, as shown by figure 4.17, this will form a hexagonal shaped absorption area under the square area of the pixel, as points to the left and right of the pixel are

closer to the pixel than the guard rails and so will attract charge generated in those areas nearby.

This excess area can be calculated to make a correction to the absorbed photocurrent, and also connection to the outer pixel that is entirely surrounded by the guard contact can be used as a comparison for validating this correction. Using figure 4.17 as a reference to calculate this area, by two parts to the hexagonal area A, a central square of area Q and side length q, flanked by two outer isosceles triangles of area R. The central square width q is equal to the pixel width plus half the distance to each rail,

$$q = \frac{s}{2} + d + \frac{s}{2} = d + s \quad Q = (d+s)^2 \quad R = \frac{Q}{4} \tag{4.2}$$

making

$$A = Q + 2R = \frac{3Q}{2} = \frac{3}{2}(d+s)^2 \tag{4.3}$$

So given the pixel width is designed to be $500\,\mu$m and the separation to be $250\,\mu$m, the detective area under a single pixel in this device regime is $0.844\,\text{mm}^2$, which is 3.3 times larger than the pixels surface area, P of $0.25\,\text{mm}^2$. This must then be considered to be the detective area when making detectivity calculations based on the charge collective area. This malformation of the detective area also might lead to artefacts in xy-scan based imaging done with these devices, essentially increasing blurring in the lateral direction more so than the vertical.

The second mask was produced though use of a precision laser cutter on laser paper, of thickness $100\,\mu$m, which was made possible by the reduction of the mask
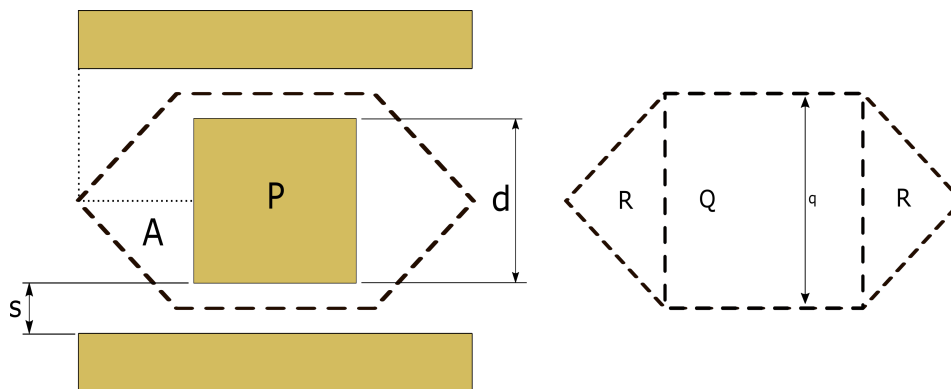
Figure 4.17: Diagram of the effective area of detection for a square pixel with electronic guard rails above and below. P is the pixel area, A is the detective area, d is the pixel width, s the separation between the pixel and the rails, Q is the effective area square and R area of the isosceles triangles on either side of the square created by finding the nearest attractive surface

details. This ensured the process of cutting was much cheaper, masks could be disposable and remade on demand, and corrected immediately upon the emergence of errors.

4.5.2 Final Devices (D1-D9)

For the final test measures that aimed to create a standardised set of data to record, 12 perovskite pellets taken from table 4.5, save for F2A-Br as it was too large, were used. These used the second mask pattern for contact deposition along with one channelled device and one 5x5 pixel array. Through the patterning and further processing, 3 pellets broke apart and so 9 final devices were left for testing. Images of these devices and their surface contacts are shown in 4.18.

Devices D4, D7 and to an extent D9 suffered from misalignment of the deposition mask, which was due to poor stabilisation prior to evaporation that would be avoidable for further depositions. Devices D3, D5 and D9 were pellets used after melting in the furnace, which generates the notable lightening of their colour.

(a) D1 → G1A-Br

(b) D2 → G1B-Br

(c) D3 → F2B-Br

(d) D4 → G5A-I

(e) D5 → F4-I

(f) D6 → G1D-Br

(g) D7 → G1E-Br

(h) D8 → G1F-Br

(i) D9 → F3-Mix
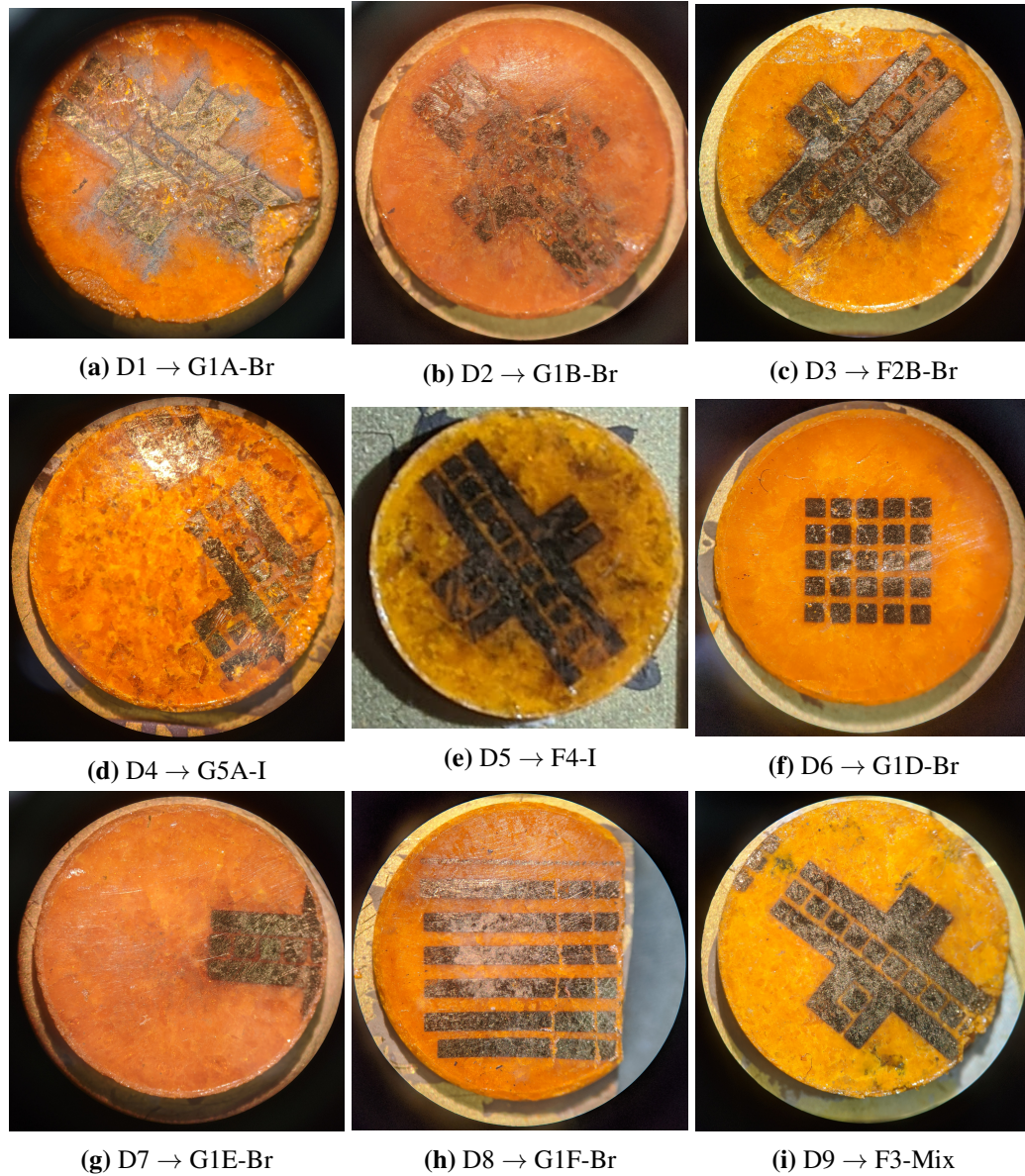
Figure 4.18: A set of images taken through a x36 Microscope of the samples D1-D9, where each image is captioned with the pellet sample used. (D5 was not captured in this set). Samples D1-D4 at this point had already been tested, and as such show signs of degradation from both the testing method using a needle probe and also from high voltage induced contact spreading

D4 and D5 used mixtures that involved $CsPbI_3$, which can be seen in darker flecks mixed into the bulk of the pellet.

Because these devices were contacted through a needle probe that exerted strong pressure on the surface, some contacts were scratched during use which can

be observed in D1-4. Also, D1 was tested with a relatively large bias voltage of 20 V, which has the observable effect of causing the gold contact material to disperse from its initial location. This phenomena led to electrical contacts partially linking up and short circuiting, leading to a much less useful test device.

4.6 Conclusions

In summary, two broad sets of devices were synthesised. The first instance involved devices mostly used as a 'proof of concept', to calibrate measurement equipment and determine best practices for building a standardised set of devices. The second instance built upon these by creating a set of devices with a large degree of self similarity such that they are much more comparable amongst one another so that a comprehensive set of X-ray detection testing would yield useful results.

$CsPbBr_3$ was successfully grown through the Anti-solvent Vapour-assisted Crystallisation (AVC) method, along with two additional batches of iodine doped $CsPb(Br_{0.8}/I_{0.2})_3$. Two methodologies for sample preparation were attempted; pellet pressing with a hydraulic press and furnace melting in vacuum ampoules. Greater success was found with pressed pellets, as their structural integrity and surface flatness was far greater, while the furnace pellets failed to hold together under even gentle pressure and did not form well bonded single crystals. As a result, the final batch of samples was entirely composed of 1.01–1.12 mm pressed pellet devices, with a few taken from the furnace melt batch and reprocessed into pressed pellets.

PL measurements showed devices to have a reliable bandgap between 2.32 eV and 2.38 eV, even after being ground and pressing or furnace melting. Iodine doped

samples exhibited bi/trimodal peak distributions, however this was not observed in the standard $CsPbBr_3$. Though, many samples had large variations in PL intensity dependent on the location upon the sample surface.

Designs for contacts were developed for best measuring X-ray detection with the equipment available. An initial mask design was used with pixel contact arrays of 100–500 µm width, for the first batch of devices, which had some success but was unfortunately not useable for more than a few iterations. The second batch found success in a much cheaper mask design process through laser cutting cheap plastic laser paper, making for disposable masks. This led to a new mask design of a lower resolution but nonetheless effective in achieving 500 µm pixel contacts, as well as electric field guarding contacts.

Chapter 5: Perovskite Modelling

In order to design devices specifically for the purpose of X-ray detection, in the operation range of 10–150 keV, it is necessary to run simulations of the materials under X-ray irradiance to predict performance and compare with measurements made. For this reason, many simulations were set up to observe where in the samples the deposition of energy should be most concentrated and the degree to which this energy spreads through radiation transfer. In this chapter, simulations of $CsPbBr_3$ radiation attenuation and absorption were run using GEANT4, utilising much of the progress made in chapter 3.

5.1   Simulating Dose Depth

A good starting point for the understanding of a material's performance under X-ray irradiance is through analysing the level of attenuation for relevant energies of photons. To study this, a simulated thin beam of monoenergetic X-ray photons were directed towards a cube of $CsPbBr_3$ and the energy deposition and its depth recorded. The X-ray beam energy was then incremented from 5–150 keV and the cube was separated into 100 μm slices so that the penetration depth of the photons
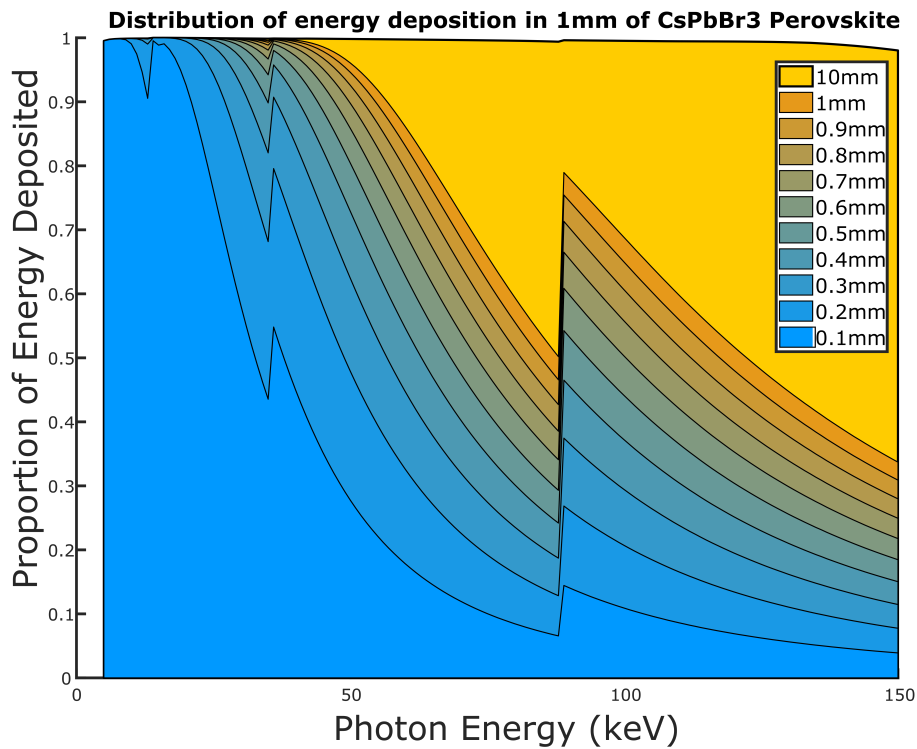
Figure 5.1: A simulation of CsPbBr$_3$ in GEANT4 attenuating X-ray photons with energies varied from 5 to 150 keV.

could be observed in steps. Photons and freed electrons were considered reaching rest and depositing the energy when dropping below 1 keV total kinetic energy.

The results from this simulation are shown in figure 5.1. This shows the proportion of the beam of each energy deposited in the first 1 mm of the perovskite, divided into 0.1 mm subsections. For the first 5–10 keV the entire beam is absorbed by the first 0.1 mm, which begins to decrease and share with the next layer, until reaching high enough energy to hit the first major absorption edge of Br at 13 keV. After this, the first layers absorption continues to drop again to below 50 % before the Cs absorption edge at 36 keV gives a small increase. Only above this energy does some of the beam begin penetrating through the entirety of the first 1 mm. As energy is increased, still at least 50 % of the beam is absorbed all the way up to

the Pb k-edge at 88 keV, which then contributes to the majority of the remaining absorption up to 150 keV. The remaining energy from the beam up to 150 keV is essentially entirely absorbed if the material is extended up to 10 mm.

The results from figure 5.1 can be used to decide upon a minimum thickness for an active channel dimension for the $CsPbBr_3$. Around 1 mm would be ideal for diagnostic energies, given the average energies of diagnostic X-rays rarely exceed 120 kV p and even then the mean photon energy is around 50 keV. Increasing this thickness much more will provide diminishing returns verses the increases in photons absorbed, as it will increasing the charge collection time and decreasing the charge collection efficiency due to recombination.
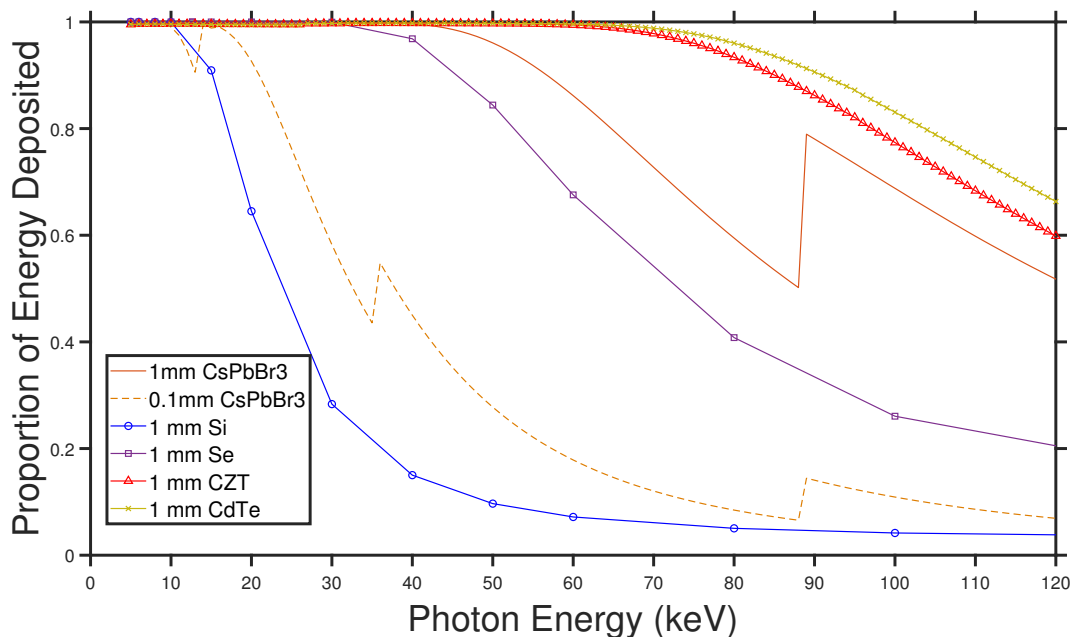
Figure 5.2: A graph showing the proportion of incident X-ray energy absorbed per keV within 1 mm of $CsPbBr_3$ and various relevant materials. 0.1 mm of $CsPbBr_3$ is included for comparison to Si

The attenuation of X-rays by $CsPbBr_3$ can be compared with current popular materials for radiation detection, such as CdTe, CZT, Silicon and Selenium, as

shown in figure 5.2. Silicon is easily the least attenuating material, as it is light and low density in comparison to others, such that even $CsPbBr_3$ of a tenth of the thickness has greater attenuation. For the range of energies from 40–90 keV, $CsPbBr_3$ is about 20 % greater than Selenium. After the characteristic edge of Pb at 89 keV, however, the attenuation is closer to CdTe and CZT. These two materials continue to have greater beam absorption than $CsPbBr_3$, owed to their high density, which is one reason for their research interest.

The device thickness to use would ideally be informed by prior knowledge of the perovskites electronic characteristics, i.e. the $\mu\tau$-product, which unfortunately will only be measurable post production. Nonetheless, 1 mm is a very practically comfortable thickness for these experiments, since material structural integrity is also important to ensure their longevity.

5.2 Perovskite Material Attenuation Experiments

Through the experimental validation of the simulated X-ray spectra in chapter 3, it is possible to then simulate perovskite samples in a beam of X-rays, and to verify the result by comparing with observables from experiment.

5.2.1 Attenuation Measurements

In this section, a variety of perovskite samples were placed in a collimated beam of X-rays. A diagram of the setup is shown in figure 5.3. The samples were placed 264 mm from the X-ray source and the dose read out using an air based ion chamber, as used in chapter 3, from behind. The beam was collimated to 1 mm at a distance of 51 mm leading to a beam width of 5.2 mm when reaching the sample,
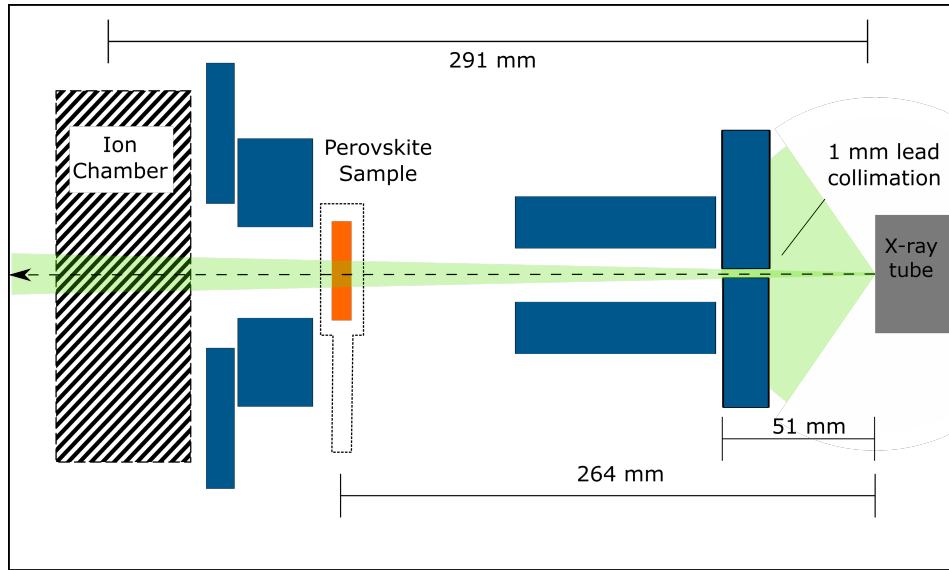
Figure 5.3: A diagram showing the filtration setup used to test the perovskite samples, using a collimation window of 1 mm

and 5.7 mm when reaching the ion chamber.

Material	Thickness (mm)	Diameter (mm)	Mass (g)	Density ($g\,cm^{-3}$)
Errors for each measure	±0.01	±0.01	±0.001	±0.01
$CsPbBr_3$ Sample 1	1.10	8.93	0.269	3.91
$CsPbBr_3$ Sample 2	1.11	8.81	0.273	4.04
$CsPb(Br:I)_3$	1.02	8.86	0.250	3.96
CsPbBr(Impure)	1.26	8.85	0.278	3.59
Lead pellet	3 ± 0.05	8 ± 0.25	1.71	11.34

Table 5.1: Table of the dimensions, mass and density of samples used in experiment, the errors row refers to errors in each column where error is not explicitly stated

Each perovskite sample was weighed with scientific scales and extents measured with digital vernier callipers, which are shown in table 5.1. There is slight variation between each sample, so this was considered in the experiment and simulation. The exact material composition differences and causes are discussed in section 4.4.

Material	Attenuation Density $(\mathrm{kg\,m^{-2}})$	Dose Recorded in 300 seconds (μGy)	Dose Rate $(\mathrm{μGy\,s^{-1}})$
Errors	± 0.003	± 2.5	± 0.002
None	0	159650 ± 25 (in 40 seconds)	3991.25 ± 0.02
$CsPbBr_3$ Sample 1	0.169	5315	17.717
$CsPbBr_3$ Sample 2	0.166	4925	16.417
$CsPbBr(Br:I)_3$	0.154	5720	19.067
$CsPbBr_3$ Impure	0.171	4125	13.750
3 mm Lead Pellet	0.860	375 ± 0.5	1.250 ± 0.003

Table 5.2: The doses measured by the ion chamber when placed behind the perovskite samples initially recorded over 300 seconds, however the bare case only allowed recording for 40 seconds before overloading the sensor. The Thales tube was run at 100 kVp and 9.0 mA.

Table 5.2 shows the measured doses from this experiment. The dose rate was found by switching the source on for 300 s, taking the total dose measured in that time and averaging over the period, reducing the effects of beam instability and ramp up time. For the case where the ion chamber had no pellet and was directly exposed to the source, the exposure time was reduced to 40 s as the total value overloaded the ion chambers maximum integration limit. It can be seen that the attenuation density is a good measure of the expected dose to carry through to the ion chamber, as this is a value proportional to the total physical quantity of the material between the X-ray source and the ion chamber.

5.2.2 Attenuation Simulation

A simulation of this environment was built, as shown in figure 5.4. Using the simulated spectrum determined from section 3.5.1, the beam was set to diverge at

the same degree the Thales collimated beam should at 1 mm per 52 mm. Each material was simulated as an 8 mm diameter disc placed in the beam with variable thickness and density according to their measured values. The sample with Iodine present in the makeup was assumed to have 24% Iodine to Bromine ratio as was calculated from the synthesis ratios, discussed in section 4.4. The rest were assumed to have 100% $CsPbBr_3$ as exact material composition of contaminants was not measured.

The simulated doses were taken from measuring the energy absorbed by the air volume of the modelled Ion Chamber, which is modelled the same way as in section 3.3.1, where all deposited energy is considered to be collected by the electrode. Using the results from the spectrum simulation, it was possible to calculate the number of photons produced per second by the Thales tube. This was done through first determining the amount of high energy electrons emitted per second from the generators cathode, by multiplying the tube current by the number of electrons per amp. During simulation of the spectrum, the number of photons counted by the detection volume corresponded to a small solid angle determined by the size of the detection volume. Multiplying this by the electrons per second, a value for the photons per second over a set solid angle is produced, and when the solid angle is small (~5°) the spectrum can be considered invariant across it. So for the case of the perovskite dose simulation, the ratio between the initial solid angle and the solid angle produced by the collimation of 1 mm per 52 mm will give the photons per second directed at the pellets and ion chamber, labelled here as P.

The simulation was run for 2e9 photons, and the dose recorded in the ion cham-
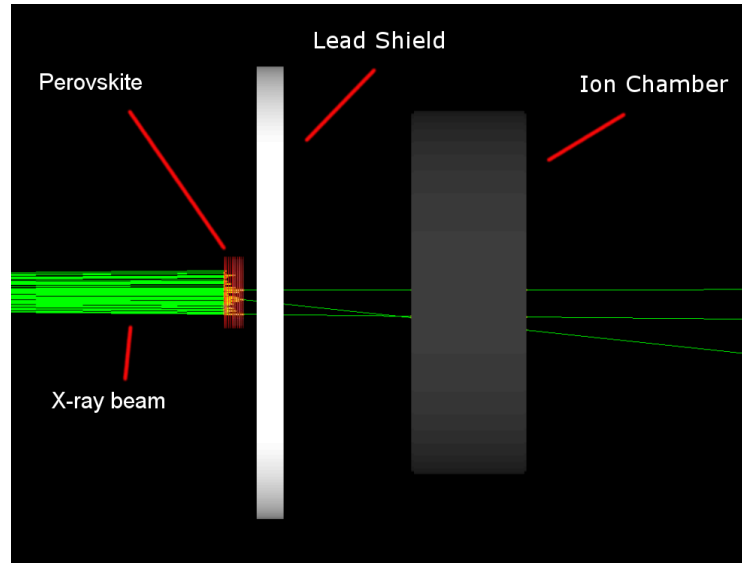
Figure 5.4: Side view of GEANT4 simulation showing a beam of 100 X-ray photons being mostly attenuated by the perovskite sample. The photons are generated from a histogram representing the Thales source

Materials	Thickness (mm)	Measured dose rate (μGy s^{-1})	Simulation (μGy s^{-1})	
			(a) Bare	**(b) Photon**
Bare Exposure 1	-	4185	4200	2853
Lead Pellet	3.25	1.25	0.010	0.0068
CsPbBr$_3$ - Sample 1	1.10	18.6	24.51	16.65
CsPbBr$_3$ - Sample 2	1.11	16.9	22.62	15.37
CsPbBr(Br:I)$_3$	1.02	19.4	27.02	18.36
CsPbBr$_3$ Impure	1.26	14.5	22.32	15.16
Bare Exposure 2	-	4230	4200	2853

Table 5.3: A table of the dose rates recorded by the ion chamber in experiment compared to the values predicted by a simulation of this experiment, where the simulated doses are scaled to match either (a) the dose recorded in the bare exposure or (b) by the estimated photon fluence of the X-ray generator

ber air volume was then multiplied by this correction factor, P. Table 5.3 shows the

results of this simulation compared with the results found from experiment.

There are two methods to consider the dose recorded by the simulation, by

scaling the values so that the bare exposure is equivalent between experiment and simulation, or by multiplying by the expected fluence of photons in the sample. The former faces difficulties in that it relies upon the virtual geometry of the exposure being accurate, and despite being simplistic, the spectrum also has a strong influence on this value. Meanwhile, scaling by the photon flux is heavily reliant upon the manufacturer specification to be accurate enough to predict a translation from the beam current to the number of X-ray photons generated. Both of these methods can be skewed by inaccurate simulation of the filtration and collimation, as small changes in filtration vastly modifies the number of low energy photons, which shifts the spectrum also and so the scaling of the dose deposition can be insufficient due to small inconsistencies.

Nevertheless, in this instance multiplying by the predicted photon fluence produces much closer results than scaling by bare exposure. Perhaps a more informative measure is paying attention to the ratios of dose recorded behind each sample, as this serves to make a good comparison of material simulation at this similar level of filtration.

Materials	Measured exposure rate ($\mu Gy\,s^{-1}$)	Simulation Scaled to Photon output of the tube ($\mu Gy\,s^{-1}$)	Ratio
$CsPbBr_3$ - Sample 1	17.4	16.65	-4.0%
$CsPbBr_3$ - Sample 2	15.7	15.37	-1.8%
$CsPbBr(Br:I)_3$	18.2	18.36	+1.2%
$CsPbBr_3$ Impure	13.3	15.16	+14.4%

Table 5.4: A table directly comparing the measured dose after removing the background exposure and predicted dose from simulation

One detail to note is that the simulation predicted that the amount of Lead in use should lead to a negligible recording of dose in the ion chamber, whereas a value of $1.25\,\mu\mathrm{Gy\,s^{-1}}$ was observed. This is likely due to a background leak of X-rays in the experiment reaching the ion chamber via alternate directions to the initial collimation, via effects such as backscatter. As a result, the values recorded behind the lead can be subtracted from the measurements, which lines up closer with the simulation results. This is shown in table 5.4.

It can be seen that the Impure sample has the least accurate prediction in simulation and is in fact more attenuating than expected, even despite the extra thickness. This is likely due to some level of contamination, from the precursor ingredients not entirely reacting to form $CsPbBr_3$, perhaps involving excess Pb or Cs.

5.3 Simulation of Micro Scale Dose Deposition

To accurately model distribution of charge in the material by X-ray exposure, not just the vertical dose distribution should be considered, as lateral spread in energy is valuable to understanding the response. X-ray scatter and ionising electrons will diffuse within the perovskite laterally to spread and smooth out the localisation of beam information. Ideally, the high attenuation properties of $CsPbBr_3$ will resist this delocalisation of charge, however, understanding its magnitude and effect for diagnostic energies is nonetheless important.

Here, the simulated Thales spectrum was used as an ideal spectra to observe this spread of energy, where a singular 1 dimensional beam of X-rays was directed at the simulated sample and then the deposition of energy recorded in a cu-

bic voxelisation of $CsPbBr_3$. In this instance, two sizes were selected, a cube of 500x500x500 μm and 100x100x100 μm, split into 10x10x10 50 μm and 20x20x20 5 μm voxels respectively. The results of these simulations are displayed in figures 5.6.

For experiments carried out later in chapter 6 simulations were needed to be run to determine the dose to an amount of perovskite material placed in the beam when it is varied from 20 to 100 kV p. To verify the simulation, the ion chamber was used to record the dose at the same distance as the perovskites in experiment and then simulations of the ion chamber were run. However, it was found at this point that doses measured from the ion chamber were inaccurate and vastly overestimating the actual dose. An alternative dosimeter, a RaySafe Solo R/F, was used for validation purposes, referred to here as the RaySafe dosimeter, which is an air based ion chamber dosimeter with a cavity of 2x22 mm and a 1 mm thick lead backing to prevent backscatter interference.

The main concern for this was sourcing the X-ray spectrum to use in the simulation of this dose. A set of spectra were generated for the Thales tube specifications for 20–100 kV p using both SpekCalc and the GEANT4 simulation model. The results from this experiment are shown in figure 5.5.

The dose prediction from the GEANT4 simulation of the RaySafe ion chamber was within the quoted 5% error in measurement by the RaySafe, save for at low kV potentials, where the instruments inherent filtration generates uncertainty. The simulation follows experiment closely here, disparities between these two are likely due to simplifications in the simulation that allow for inaccurate photon counting for
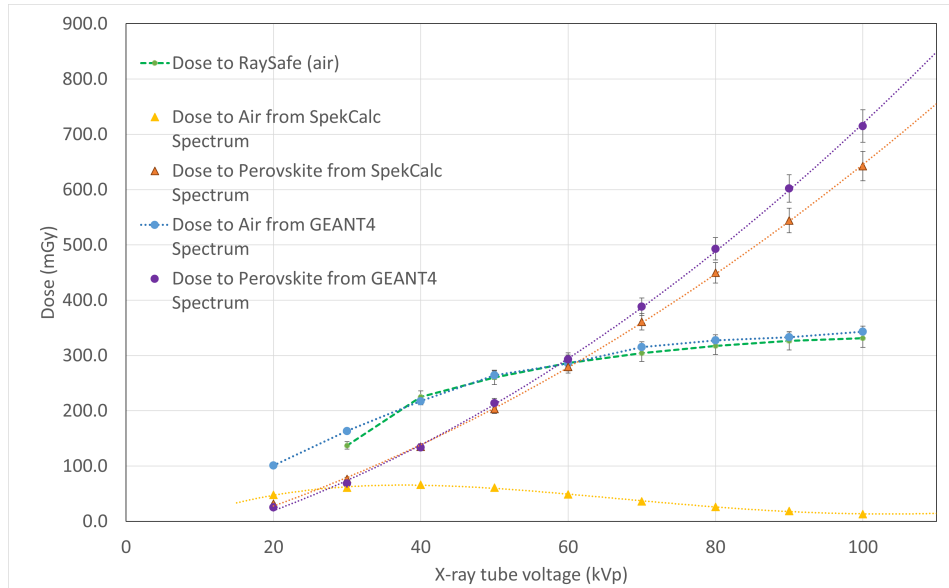
Figure 5.5: The dose deposited in the RaySafe dosimeter placed at 163 mm from the Thales source and operated at 20–100 kV p, and comparison to dose prediction using GEANT4 simulation, where the input spectra were either taken from SpekCalc or from prior GEANT4 simulation

each spectrum. This was considered a satisfactory simulation of the beam output and so used to simulate the dose delivered to the perovskite materials.

The major failure of the SpekCalc simulation was in predicting the total output of the tube, such that the values assigned to the higher energy spectra did not contribute enough total photon counts to account for the spectral shift to higher energies. For example the total photon count given by SpekCalc at 100 kV p was 5 times greater than at 20 kV p, whereas the GEANT4 simulation found this same ratio to be 10 times greater, a factor of 2 difference in dose rate. As a result, the simulation showed the dose in fact decreasing with increasing kV p (while tube current is kept constant), which is highly unrepresentative of reality.

The graphs are fitted with power laws however this is mostly an approximation to show the general progression, as the spectra and the spectral absorption by the

samples scale much more complexly given the numerous characteristic X-rays and absorption edges. The major contribution in the uncertainties is the variance in the mass of the perovskite samples for determining dose absorbed per sample.

It can be seen that from figure 5.6 a) and c) the primary energy of the beam does not diverge greatly beyond the central beam line at even $5\,\mu m$ of voxel resolution. It should be noted that not all of the beam is absorbed in these simulations, where in a) 29.1 % of incoming energy escapes, while in c) 65.5 % escapes, primarily all through the back of the cube. Taking logarithms of the energy absorbed to the base 10 is shown by figure 5.6 b) and d), where the spread to the immediate neighbours can be seen to equal about 1 % (2 orders of magnitude) and to the next nearest neighbour of the initial central voxel line one third lesser again.

This is an understandable observation as the majority of the interactions after X-ray absorption and x-ray scatter are in the form of ionisation electrons, which have much less penetrative power than the X-rays, and so are caught by the high stopping power of the material. This eliminates the initial concern about charge delocalisation due to direct scattering of photons and electrons within the device, so that charge sharing between contacts over relatively long distances ($> 50\,\mu m$) in a device can be attributed most directly to conduction electron drift within the material. Further loss of information would be due to X-ray scatter and fluorescence that takes the photons outside of the material.
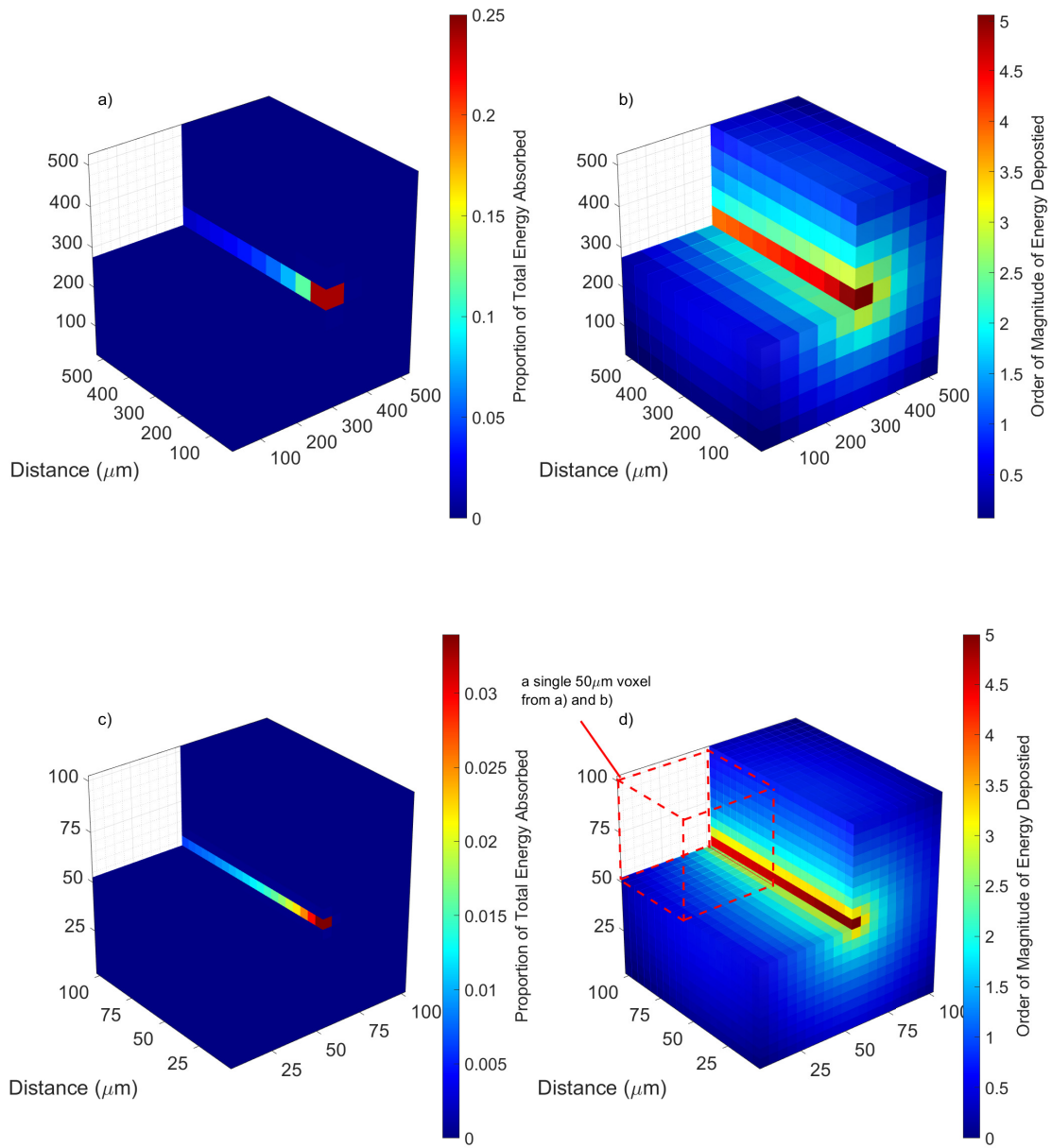
Figure 5.6: The deposition of energy in the a 500 µm cube sample divided into 50 µm cubes in a) and b) and a sub volume of such in the form of a 100 µm cube sample divided into 5 µm cubes in c) and d). These use a colour scale of blue to red as the indication for values in each cube. a) and c) show the linear proportion of total beam energy absorbed per cube while b) and d) show the logarithmic view of beam absorption in the cubes, showing the difference in orders of magnitude for energy deposited in each cube surrounding the central beam line. d) also shows the size of a singular voxel used in a) and b)

5.4 Conclusions

GEANT4 simulations were utilised to infer an optimal detection thickness of a $CsPbBr_3$ device for X-ray absorption of 1 mm. The charge distribution from X-ray irradiance at energies between 1–120 keV within the perovskite bulk material was also found, which helps to further develop contact designs and optimise charge extraction methodologies.

Validation for the GEANT4 simulations was made through an X-ray beam attenuation experiment, where a collimated beam from a tungsten target X-ray source operating at 100 kV p was directed through samples of $CsPbBr_3$ and $CsPb(Br_{0.8}I_{0.2})_3$ the change in dose rate recorded by an ion chamber. A simulation of this experiment was run finding a dose rate agreement of $< 5\%$ when the samples composition were well understood.

A further GEANT4 simulation was run to observe the lateral spread of charge deposition sites from line beam of X-ray photons through separating the perovskite material into cubic volumes or voxels, where it could be concluded that the divergence from an initial beam was small (1% spreading $> 5\,\mu m$) when compared to the charge mobility of $CsPbBr_3$ (140–$200\,cm^2\,V^{-1}\,s^{-1}$)[69].

Chapter 6: Perovskite X-ray Photoresponse

6.1 Introduction

In this chapter, the response of the devices to X-rays will be analysed and quantification of the perovskites response compared.

A major method of comparison between devices and alternative materials specifically in the realm of semiconductor photodetection is the $\mu\tau$-product. As discussed in section 2.2, this is a measurement of the overall performance of a detector in extracting electronic information after exposure to X-ray photons.

An empirical method for determining the $\mu\tau$-product is to use the Hecht equation [70]:

$$CCE = \frac{Q_m}{Q_0} = \frac{v_h \tau_h}{L}\left[1 - \exp\left(\frac{-x_p}{v_h \tau_h}\right)\right] + \frac{v_e \tau_e}{L}\left[1 - \exp\left(\frac{L - x_p}{v_e \tau_e}\right)\right], \quad (6.1)$$

where CCE is the charge collection efficiency, Q_m and Q_0 are the measured charge and maximum possible charge respectively, $v_{(h/e)}$ refers to the mobile velocity for holes or electrons, $\tau_{(h/e)}$ is the mean lifetime of charge carriers for holes or

electrons, L is the thickness of the channel, and x_p is the position within the sample that the energy is absorbed.

This equation assumes operation in a linear electric field, whereby the carrier velocity can be directly related to the electric field by: $v_{(e/h)} = \mu_{(e/h)}E$ and the electric field to the voltage across the full thickness of the detector by: $E = V/L$. This is a reasonable assumption to make when contacting the devices while connected to the guard contacts, as these guard contacts control the electric field around the readout contact to ensure it is close to linear through the material. Using this we can rearrange the Hecht equation to simply hold for either electrons or holes [71]:

$$CCE = \frac{Q_m}{Q_0} = \mu \tau \frac{V}{L^2} \left[1 - \exp\left(\frac{-L^2}{\mu \tau V} \right) \right] \tag{6.2}$$

CCE can be determined by knowledge of the photon spectrum incident upon the device and thus calculation of the maximum generated charge from such photons, compared with the charge extracted. For X-ray photons, the number of electron-hole pairs generated in the material should be equal to the total dose deposited within the channel divided by the bandgap energy required to free them. Fitting an inverse exponential to this relation while keeping the electric field constant will give the $\mu \tau$-product.

6.2 Experimental Setup

6.2.1 Testing Apparatus

The novel properties, such as the high Z and the various methods of synthesis of $CsPbBr_3$ could be exploitable for alternative device designs. For example the high attenuation of the material enables a much thinner layer to be required for absorbing incident radiation, which in turn enables more reliable photogenerated charge collection. In a pixelated detector, this could lead to either smaller pixels and an increase in resolution, or a decrease in spatial blurring in the image.

For interfacing with devices a system was required to be developed to simplify the inspection and exchange of multiple samples. Such a system would need to have reliable electrical contact with each device, regardless of individual design modifications.
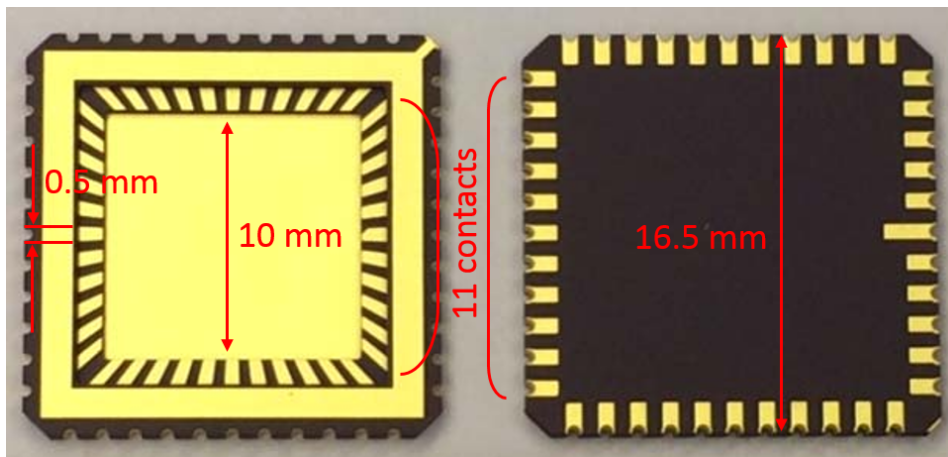
Figure 6.1: An image showing the ceramic Leadless Chip Carriers (LCC) used for device contact in most experiments, acquired from spectrum semiconductor materials

It was decided that a standard to follow would be to use Leadless Chip Carriers (LCC) as the base carriers for the devices. A diagram of the LCC type selected is

shown in figure 6.1. The carriers were a ceramic plate, coated with evaporation deposited thin layer Au contacts of $> 1.5\,\mu m$ thickness designed for wire bonding interfacing. This offered a reliable and standardised testing bed for placement of of the samples, with a simple mechanism for contacting the back plane of the device from underneath. The LCCs utilised 44 contacts in total, so each provided a large amount of flexibility and capacity for interfacing with contacts laid down on the surface of samples. The back plane was also coated with gold, so that a sample secured in the centre would have an even and continuous electrical contact.
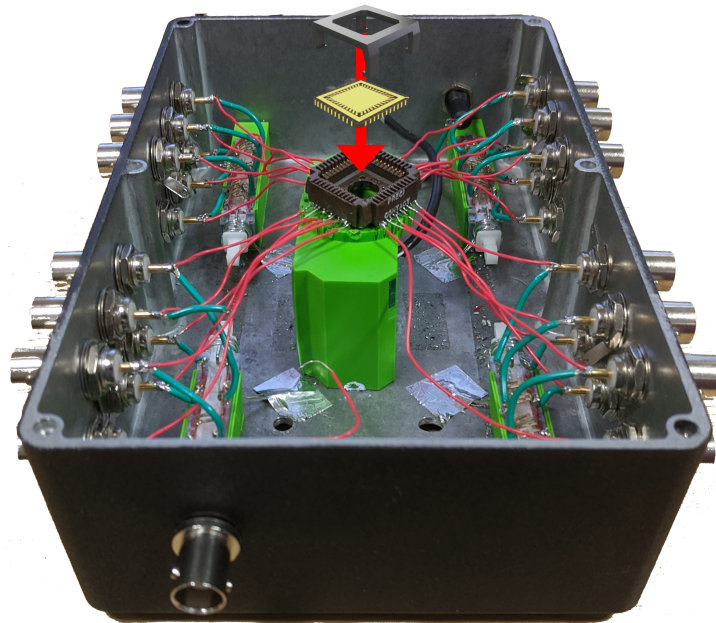
Figure 6.2: An image of the testing box apparatus with the LCC and a 3D printed clip above the socket

These LCCs would be placed in a receptor socket with spring loaded contacts and would directly interface with each of the outer gold coated grooves of the LCCs, which is shown in figure 6.2. This required force to hold the sample carriers in place, so a kinetic clip was 3D printed to fit over and press enough force onto the LCCs to

ensure reliable continuity between carriers and socket. To find an appropriate clip size, the LCCs were tested using different lengths of printed clip, using a multimeter to ensure reliable connection between the carriers and the outer contacts. A full diagram of this setup is shown in figure 6.3.
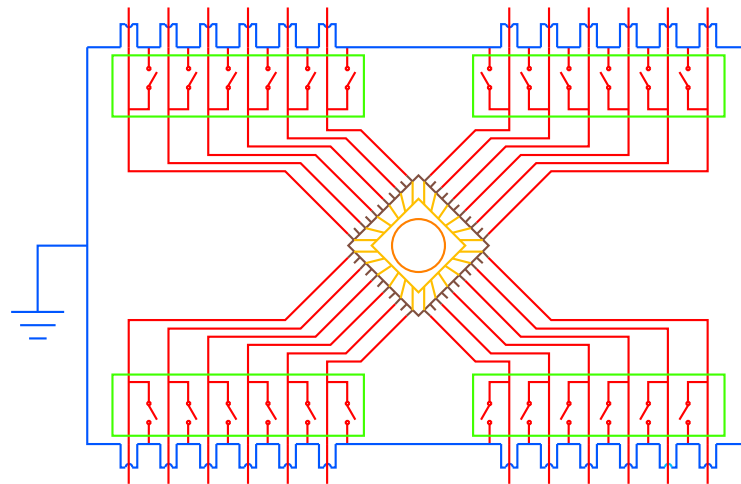
Figure 6.3: A wiring diagram of the test box showing in fig 6.2 to show how the devices were connected and measured. Red lines represent the connection directly to the LCCs socket, the cyan line is the grounded outer shell of the box for Electro Static Discharge (ESD) and background noise shielding, and green boxes refer to the bulk on-off switches which connect to each input to the grounded box in cyan

The socket was secured inside of an aluminium box as a protection against several potential issues. Firstly, the sealable lid meant it was reliably light tight, enabling repeatable dark current measurements. Secondly, it served as a structure for attaching and detaching wiring connections to measurement instruments and for protection from disturbing the samples or internal delicate wiring. Thirdly, connecting the aluminium box to ground acted as a shield against background electronic noise and, with installation of a switching array the testing wires, served to protect any plugged in devices from Electro Static Discharge (ESD) effects.

Once secured inside the box, thin Ag coated Cu wires were soldered from the

LCC socket to feedthrough BNC plugs. Due to a lack of space, only 24 of the socket contacts were able to be connected. Each of these was directly connected to a switch array leading to direct connection to the box and ground. The switch was closed when handling the box and open during any device measurement. The total ohmic resistance between any BNC plug and each LCC contacts was consistently measured to be $\sim 10\,\Omega$, which was well within acceptable limits for accurate testing on the high resistance samples in this project.

Underneath the LCC and socket assembly, a CCD webcam chip was placed. It has been observed [72] that X-ray photons, when impacting the surface of a CCD detector, will overload the pixel with charge and hence produce an observable event. Since the pixel pitch of the CCD was $4.6\,\mu\mathrm{m}$, this was useful for locating an X-ray beam when it was tightly collimated to a pencil beam anywhere less than $500\,\mu\mathrm{m}$.

To reduce impact on the X-ray beam filtration, a $25\mathrm{x}25\,\mathrm{mm}$ square of material was removed from the lid of the aluminium box directly over the LCC socket and replaced with an adhesive strip of aluminium $60\,\mu\mathrm{m}$ thick. This could be removed for direct exposure, or left closed to ensure light tight X-ray detection while avoiding much filtration of the beam.

Measurement of the current through devices was conducted through connection to a Keithley 6487 picoammeter, which can resolve currents as low as $0.01\,\mathrm{pA}$. However, the measurement rate can only be increased up to $600\,\mathrm{Hz}$ on this instrument, limited by the power supply AC period, so sub-millisecond measurements were unavailable for the majority of experiments. This testing box was used for the majority of primary experiments where the device contacts were wire bonded to

LCCs.

Due to a break down of the wirebonding tools and time constraints, an alternative contact method was required. As such a direct contact based probe station was designed. The design of this probe station is shown in figure 6.4. It is designed so that the height of a probe can be adjusted by screwing a support bolt into the main bed higher or lower, and then the main body of the probe made to hold in place through tightening a bolt around the base. Then the probe needles themselves are made from gold plated 200 µm needles soldered to the output of BNC sockets, which are then screwed in and held in place by attachments to the probe station structure. The entire apparatus assembled together grants adjustable probe positions both in the lateral plane upon the device surface and the height above the device, leading to adjustable contact pressure.

A disadvantage of this design is that it does not incorporate any form of electrical noise shielding as the previous testing box did, and so may result in more noisy response measures. Depending on the magnitude of device response, this issue may diminish.

6.2.2 Experimental Procedure

6.2.2.1 X-ray Response Exposures

For the measurement of direct detection of X-rays, to look at responsivity and detectivity, each device and their pixels were tested following a standard repeatable exposure regime.

Each device current was measured for 940 seconds, during which time the
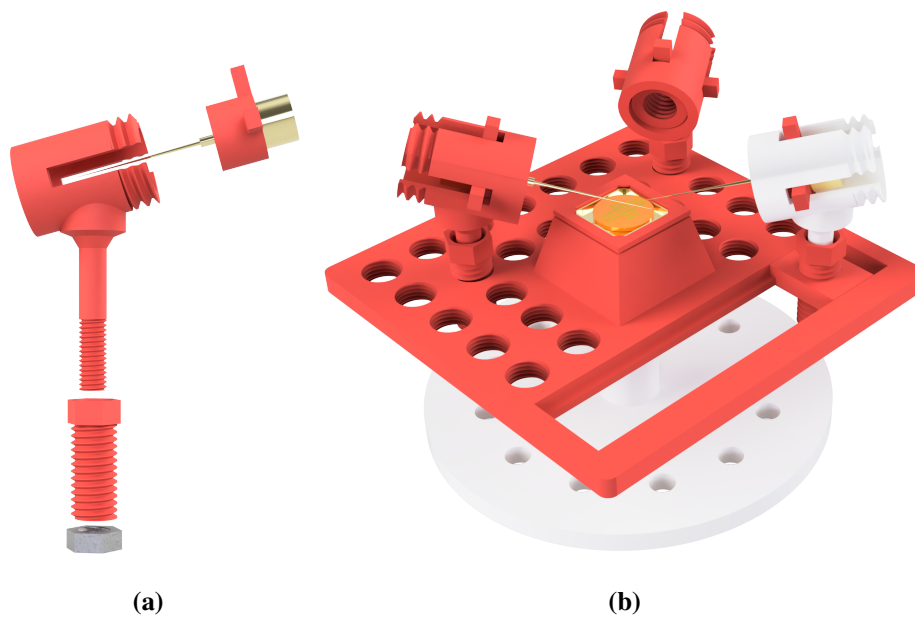
Figure 6.4: 3D renders of the probe station a) showing a blown up view of the parts for each probe stand b) the finished probe station as printed connecting to a sample device

Thales X-ray tube was switched on and off at equal timings. The regime followed as such; 120 seconds of no activity, then switch X-rays on at a set kVp and mA for 20 seconds and then switch off again for a further 20 seconds, then increment the kVp or mA, ranging from minimum values to maximum values allowed by the X-ray generator. No filtration was used beyond the inherent of 1 mm of Be and the focal spot was set to 4 mm to allow the tube to be operated at a higher maximum power output.

Initially, in the first set of devices and experiments, the exposure regime followed increasing the kVp from 20 - 100 in 10 kV increments. Later, especially for the final set of devices, the regime was expanded to include also keeping the kVp at 100 and instead increasing the mA from 1 - 10 in 1 mA increment. Figure 6.5 describes this scheme of varying both values and shows an approximation of the X-ray

tube output. This is acquired by assuming the energy of the beam is proportional to V^2I, so increases in the tube voltage increase output non-linearly while increases in the current scale linearly. This should also be visible in device response, assuming an ideal coupling between beam absorption and charge collection, and so deviations from the shape shown in figure 6.5 can be used to observe and discuss energy and photon fluence based variations in sensitivity.

This regime was selected in order to test the response of the devices to both these geometric and linear variations in the tube output. There is a long 2 minute period at the beginning for the device dark current to observably settle under the applied bias, which can be used as a section for estimating the dark current and to fit a function to in order to remove this dark current in subsequent processing. Each ON period lasts 20 seconds in order to analyse the response over time, as it is frequently not a constant value but more following a function of time. Similarly, the OFF time between measurements lasts 20 seconds to observe how the device current relaxes back to the base dark current after exposure. Finally, the end of the regime also features another 120-140 second period to look for the longer term relaxation rate of the device after exposure and if there are any lasting change to the devices dark current as a result of radiation damage or measurement effects.

To ensure that what is being measured from connection to devices is genuine X-ray generated photocurrent, a resistor of a similar resistance to the perovskite devices was placed under examination. Figure 6.6 shows the results of exposing a $16.5\,\mathrm{M\Omega}$ resistor to the first regime of increasing kV p. In 6.6a no bias was used, a dark current of $-20\,\mathrm{pA}$ was found, and an increase in charge of $-30--65\,\mathrm{pA}$
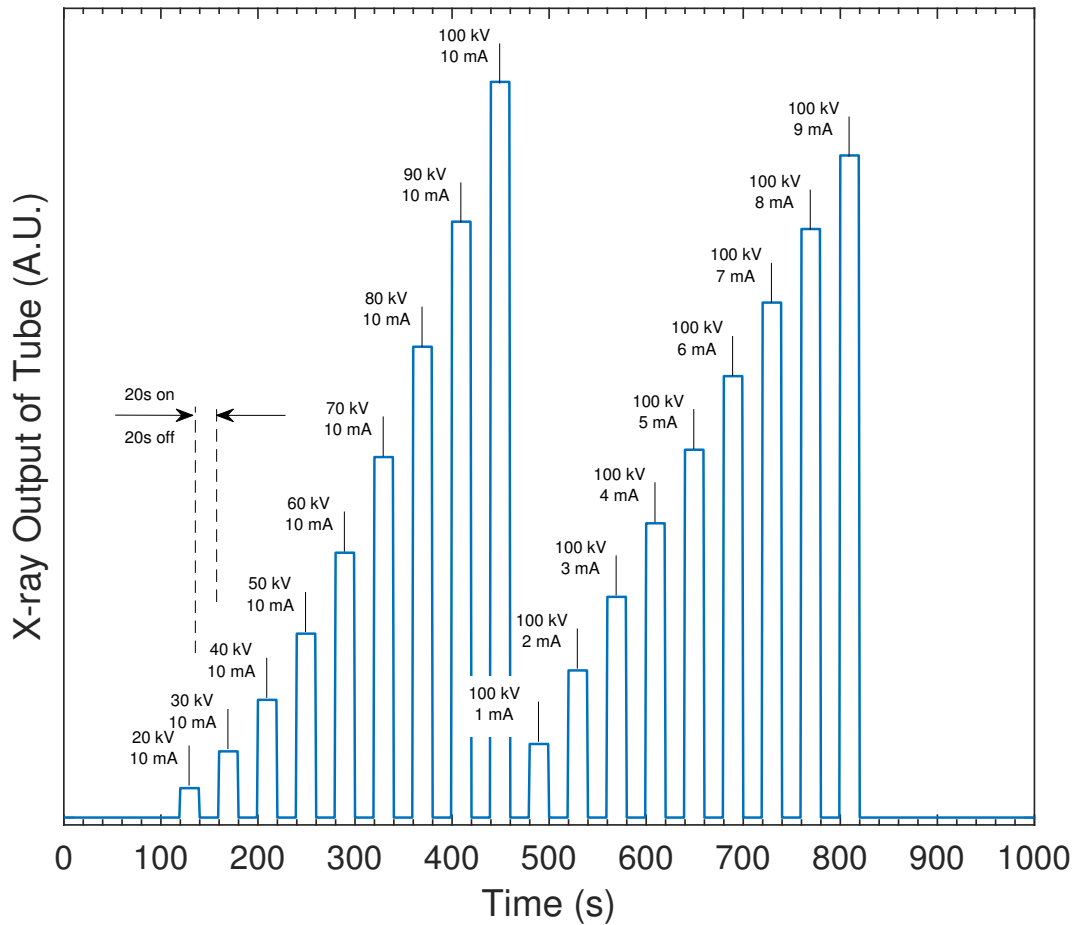
Figure 6.5: A graph of the expected energy output of the X-ray tube following the exposure standards used for the measurements of device response. Only the first half of this scheme, where kV is varied from 20 to 100 with 10 mA was used in initial experiments, but later the full scheme was used.

was observed. Interestingly, the response stops becoming more negative at around 70 kVp and then slightly decreases towards a positive current. At 10V bias, the predicted current should be 606 nA, which is a little higher than in figure 6.6b where the dark current is raised to 604 nA, leading to a total resistance in the circuit of 16.56 MΩ, well within 1% error of the resistor in use. The response here ranges from 1.1–3.9 nA increase, and appears to be proportional to a square root function of kVp.

The response here is likely due to ionisation of singular metal atoms within the
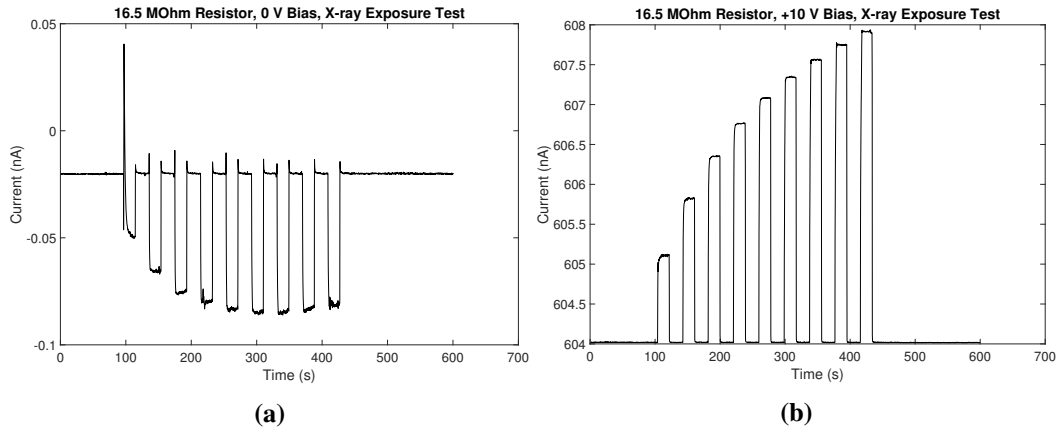
Figure 6.6: X-ray photocurrent observed by exposure of a 16.5 MΩ resistor. Figure a) is at 0V bias and figure b) at 10V bias

wiring of the test circuit, which is tending towards an upper saturation limit with further exposure. The reducing response of the resistor photocurrent is due to increase in the proportion of high energy photons which are too penetrative to interact with the resistor leading to a smaller increase in response. This phenomena is much less likely to be observed in the perovskite devices as their high attenuation properties are expected to absorb the majority of the X-ray photons up to an energy of 120 keV within their volume, as shown in figure 5.1. This helps in distinguishing between responses of a functional device and that of incidentally involved electronics.

6.2.2.2 I-V Bias Curves

Each device was also measured for its current vs bias voltage, under dark conditions and illuminated by constant X-ray exposure. For these measurements the X-rays were set at 100 kV and 10 mA, with a 4 mm focal spot. The bias voltage was varied from 0 upwards to a maximum voltage of one of $+2$ V, $+10$ V or $+20$ V, back to 0 V and continuing to -2 V, -10 V or -20 V, respectively, and finally back to 0 V, all in steps of one thousandths of the maximum voltage, over a period of 400

seconds.

Measuring I-V bias curves of these devices is very useful for multiple functions. It can be used to find the optimal operating voltage where the current under X-ray illumination is greatest relative to the corresponding dark current. Using the relation of $R = V/I$ the resistance of the material can be determined, and using the known contact dimensions and channel thickness, the resistivity also through $\rho = RA/L$. An I-V curve can also be used to observe diode like behaviour in the device under positive and negative bias, and the degree to which charge carriers are resisted in either direction. The degree of hysteresis in the material, the difference between the current observed as the bias is increased and as it is decreased immediately after, can be used to look for evidence of charge polarisation in the material. Finally the devices response stability at various biases can be observed to determine at what voltage the most noise free measurements can be made.

6.2.2.3   Dark Current Measurements

Whilst the I-V curves show the dark current of devices momentarily at various voltages, it is also helpful to measure the dark current over a longer period while holding the bias voltage constant in a static environment. In this way, several devices dark currents were measured at voltages ranging logarithmically from $0\,\text{V}$ to $+-20\,\text{V}$ bias for periods of 10 minutes at a time. This helps to understand the more medium term time dependence of the device dark current, looking for general noise values along with any broader change over time.

6.3 Measurements Made

6.3.1 Undesired Phenomena

6.3.1.1 False Positive Responses

As was seen in figure 6.6, simple resistors exhibit small but measurable response to X-ray exposure, even with no electronic bias. This form of response is characterised by diminishing increases in charge generated as the beam kVp increases, which is also a phenomena observable when recording the dose with an ion chamber, as described in chapter 3 and shown in figure 5.5. This is due to the increased energy of photons penetrating through these sensitive volumes and depositing less energy than the lower energy photons.

From the resistor tests in figure 6.6, it was initially considered that any photocurrent of this nature would be negligibly small relative to the current of a functional perovskite device. However, figure 6.7 shows an instance where this was much larger than expected. This device was contacted by silver glue of an aluminium sheet to the top surface of the entire 8 mm diameter sample. The response observed was initially considered to be material response, however, upon closer inspection, the response followed this trend of diminishing kVp response. Additionally, the dark current was observed to be 8.1 pA, which is unreasonably low for what has been seen in this material at room temperature. However, the fact that the response was several nA when exposed to a beam collimated to only impact on the sample (2 mm), and reduced largely when the beam was collimated more precisely

upon the sample (0.5 mm) implied it had to be some part of the sample contribut-
ing. It was concluded that this was likely a response from free charge excited in the
aluminium sheet directly on top, while any connection through the perovskite layer
was negligible or non-existent. The relatively larger contribution of charge would
be due to the exposure of the entire surface area of the sheet of $50\,mm^2$ to X-rays.
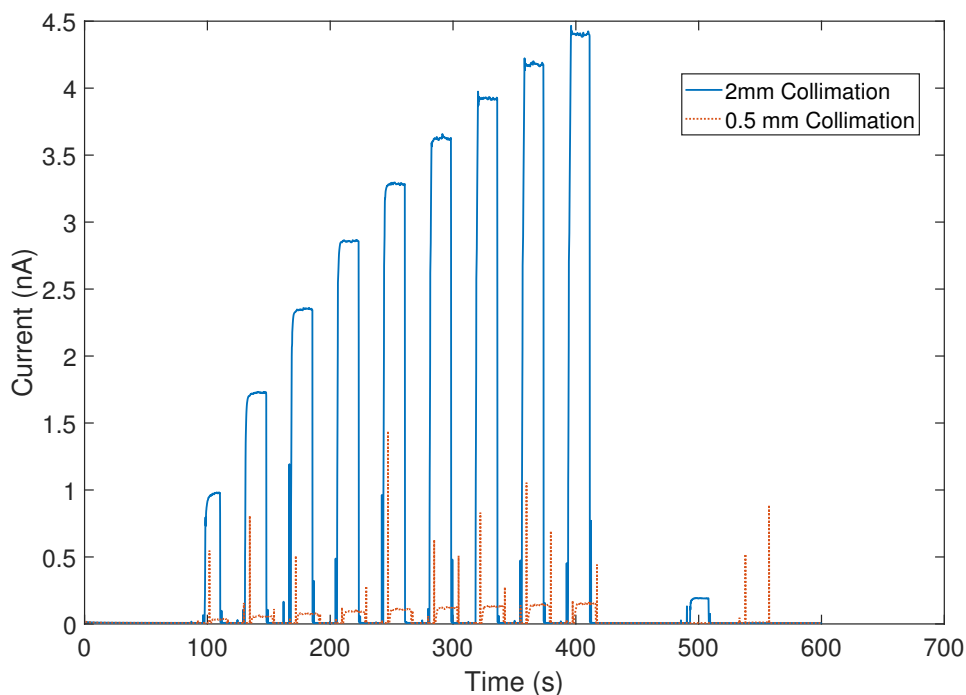
Figure 6.7: First exposure of an aluminium sheet contacted crushed sample, biased at 10 V,
showing a maximum response of 4.4 nA and an I_{on}/I_{off} ratio of 600.

6.3.1.2 Contact Erosion

Through use of the probe station apparatus, the pressure applied by the needles
upon the sample led to the removal of the gold layer after use. Two examples of
this are shown under microscope inspection in figure 6.8. Care was used to avoid
as much removal as possible, but nonetheless many contacts were damaged in the
process of testing through this method. This affected repeatability, as pixels could
not be expected to exhibit the same response when the contact area was affected af-

ter every experiment. Mitigation of this was managed by making the most efficient use of a device before removing and testing another.

(a) D6 - 100x zoom, Direct scope

(b) D3 - 100x zoom, Differential scope, highlighting edges
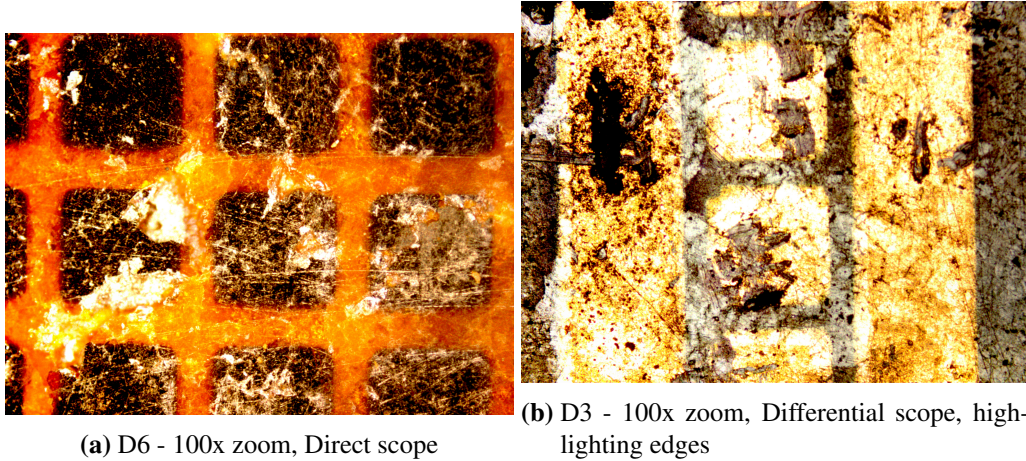
Figure 6.8: Two images of surface contacts of the samples showing the degree of contact erosion caused through application of the test probes

6.4 Analysis of Response

When measuring the response of the devices following the second regime of exposure, as described in section 6.2.2.1, analysis followed automatic peak identifying which is exemplified in figure 6.9. The device used in this example is a multigranular crystal sample that showed a large RC curve to emphasise the corrections made. Initially, in figure 6.9a, the peaks are found from thresholding the differential and then a fit with a curve of $Ae^{Bt} + D$, as in figure 6.9b, where B is the $\frac{1}{RC}$ constant and D can be used as the value for the dark current after the RC curve has flattened. The Ae^{Bt} part of this fit is then subtracted from the results to consider the device as if it had a long time to settle, i.e. t is large . The current values for each response are then taken as median values from the peak data, in figure 6.9c. These are then divided by the determined dark current to find a response ratio for

each peak, finally in figure 6.9d, to look at devices with the greatest sensitivity.
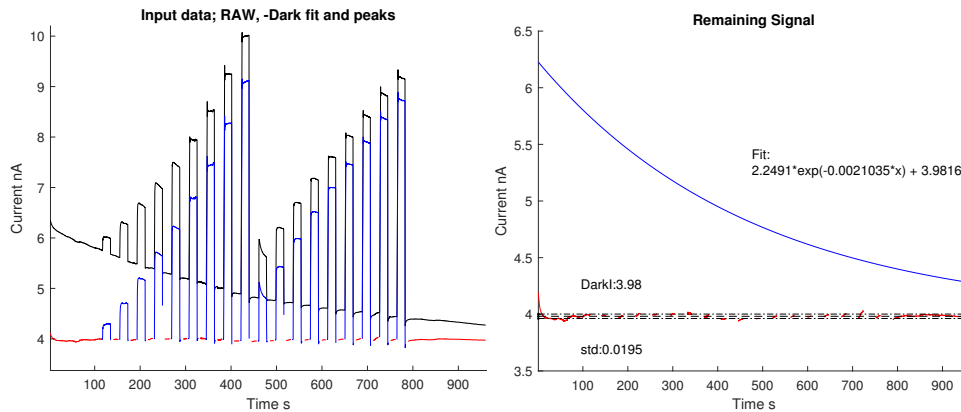
(a) A graph showing the subtraction of a fit to the dark current in order to flatten out the response data. Black is the raw data, blue the identified peaks and red the identified dark current

(b) The curve of the dark current fit with the values for the $Ae^{Bt} + D$ equation shown, and the determined dark current after subtraction with standard deviation uncertainty
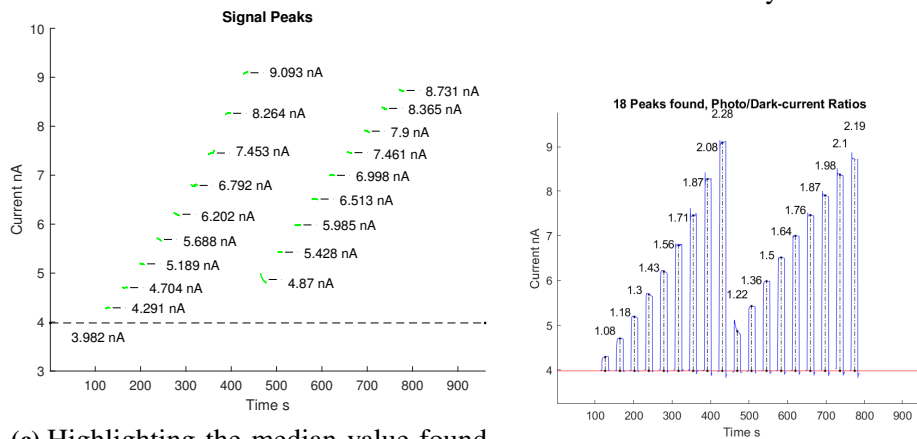
(c) Highlighting the median value found in each peak as the absolute photo current for each peak and compared with the dark current at the bottom

(d) Showing the peaks found, with the numeric values representing their ratio to the dark current

Figure 6.9: A set of 4 graphs showing the the X-ray response data processing methodology using the response of a crystal shard as an example

Using the analysis process displayed in figure 6.9, extended to all device responses measured, where the data was well behaved and easy to process, a large database of responses can be built up and analysed. Figure 6.10 shows X-ray responses observed for each device, with either increasing kVp or mA. Data was taken from as many devices as provided stable computable responses, where some

were guarded pixels, others unguarded or guards broken down. Device 6 and 8 had no guards, thus their status was difficult to accurately estimate.

Because the device contacts were not so well predictable, especially under connection from the pressurised probes that would scratch away the surface, the active area of each pixel was highly unreliable. Also, devices without guards had unknowable active areas that potentially included the entire crystal. However, the dark current for each device is directly proportional to the active area, so taking a ratio between the device responses and the dark current provides a much closer idea for how the perovskite is responding to X-rays. In addition, normalising for active area also requires normalising for dose delivered in the perovskite per unit area.

As a result of this conversion, figure 6.11 displays this, where the y-axis uses units of increase in current relative to the base dark current, for each mGy delivered per mm^2. This can be seen to be a much less erratic method of device judgement, as the unguarded devices are grouped together with the rest and there is less than an order of magnitude of variation between each set of pixels. This analysis theoretically completely accounts for unknowns in lateral spread of sensitivity, ideally should only be dependent on the perovskites resistivity, and can be considered as a relative rating of the $\mu\tau$.

Looking at the actual values displayed in figure 6.11, the response of the majority of devices follows an exponential decrease with increasing kVp, which indicates that a large portion of this increasing dose is unmeasured. This is perhaps because the radiation is able to penetrate deeper into parts of the perovskite crystal where the resulting photoelectrons are not collected before they recombine. This would

imply that the mobility in the device is not great enough to extract charges that are delivered beyond the first few µm of the material. A decrease of a lesser gradient can also be seen where only the tube current is increasing, which leads to a linear increase in dose, and, as there is no change in dose distribution only intensity, must be due to the number of photogenerated charges moving towards a saturation current.

(a)

(b)
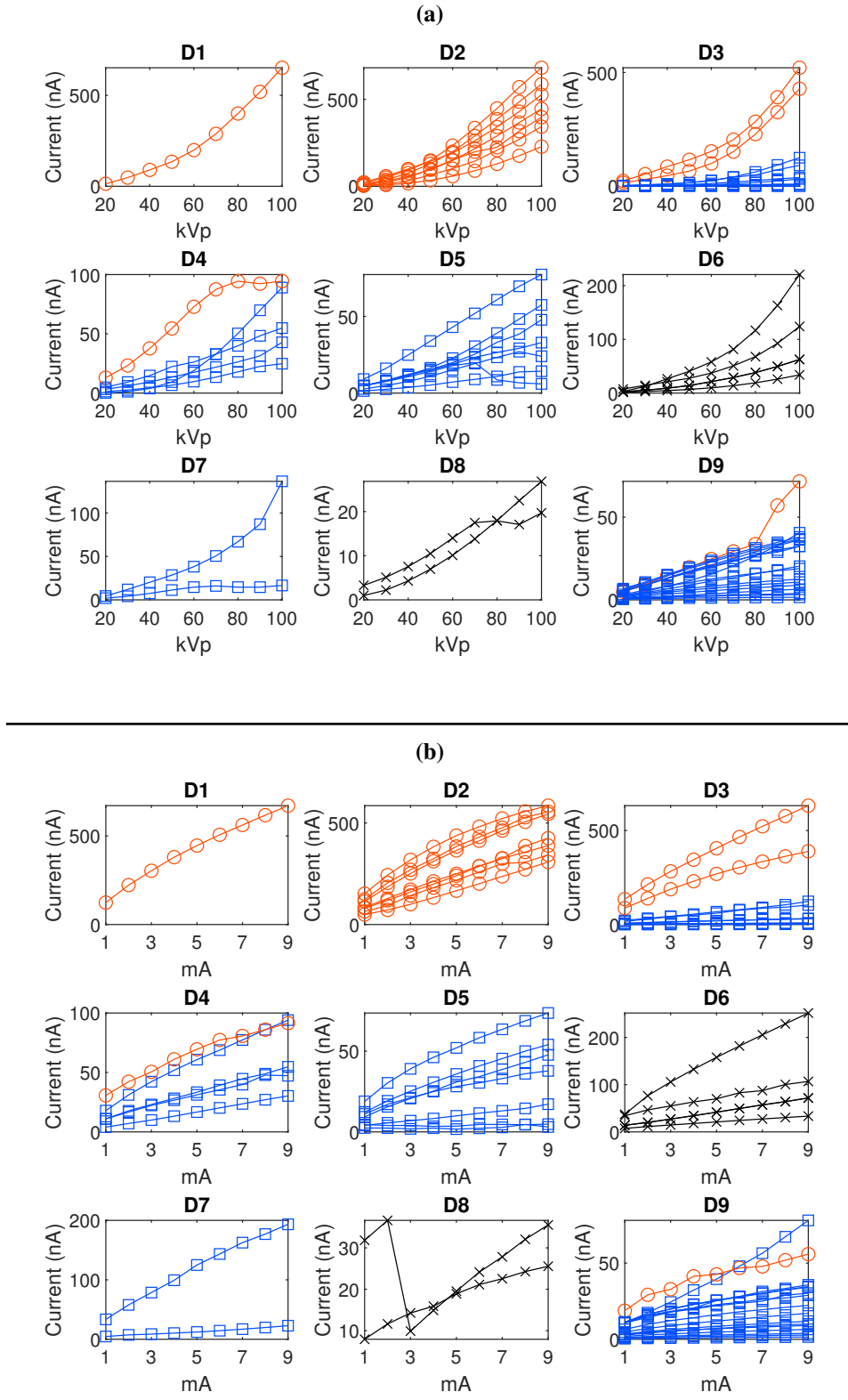
Figure 6.10: The response current relative to the kVp 6.10a and the mA 6.10b of the X-ray tube in nA proportional for most pixels of each device, after subtracting the dark current. Red (O) lines mark unguarded pixels, blue (□) lines mark guarded pixels and black (X) mark devices where the state of guarding was partial and uncertain.
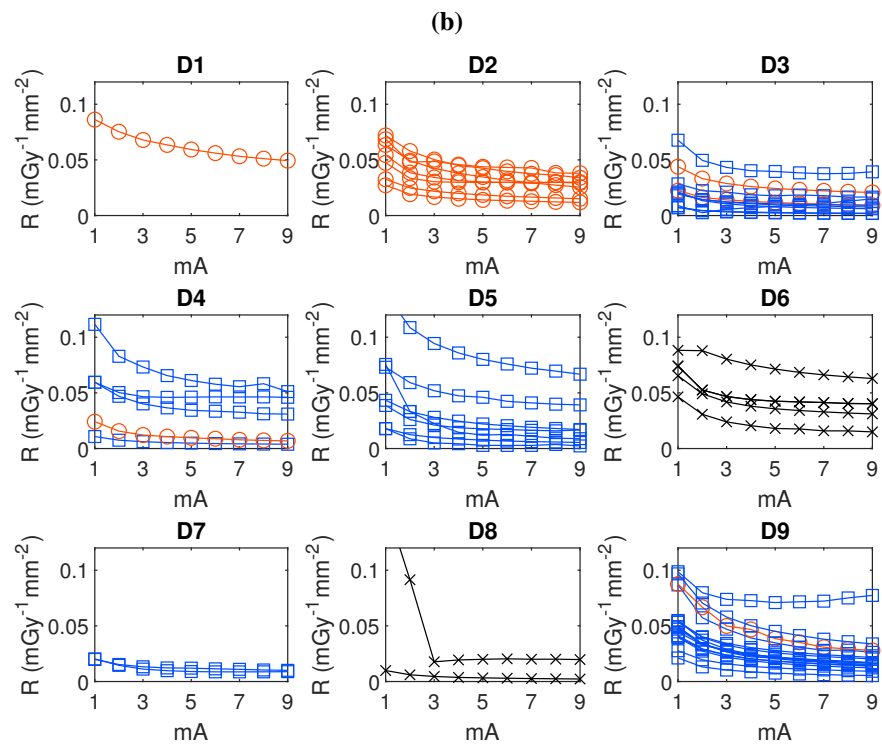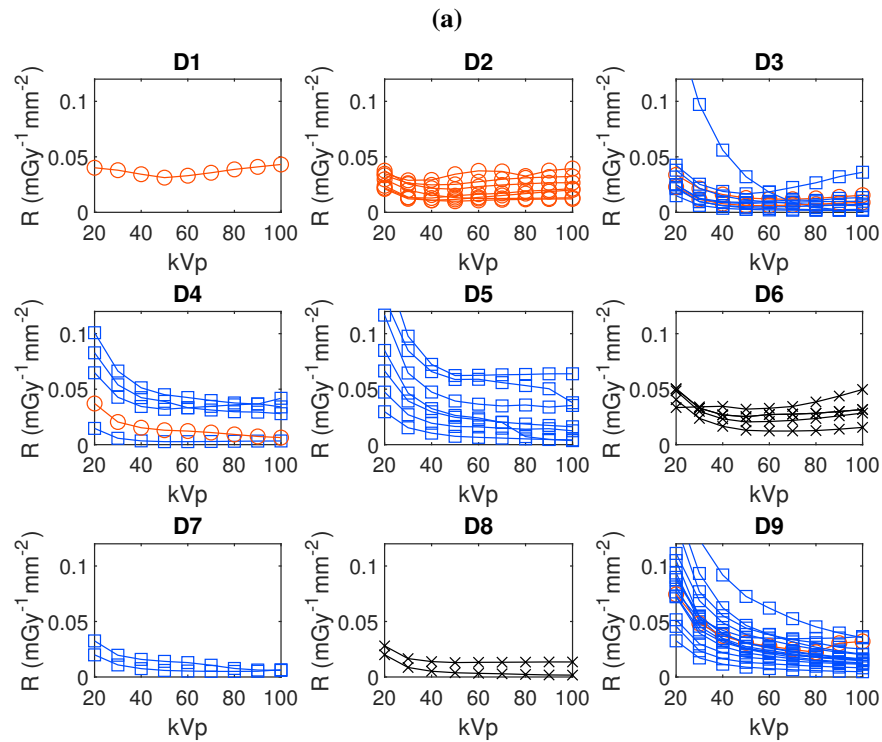
Figure 6.11: Using the data from 6.10 to find a response ratio relative to the magnitude of the dark current and normalised against the simulated dose delivered per unit area to the perovskite. Red (O) lines mark unguarded pixels, blue (□) lines mark guarded pixels and black (X) mark devices where the state of guarding was partial and uncertain.

6.4.1   Response with Varying Bias Voltage

There is much to learn about a device's characteristics from IV curves. In figure 6.12, an IV-curve is taken from a single pixel in each device to display the general response observed in each device. These are all 500x500 μm pixels being contacted via gold needle probes and were each exposed to the same X-ray fluence of photons each, for a dose rate of $1.7\,\mathrm{Gy\,s^{-1}}$ delivered to the perovskite. There are differences between each device here in how they behave, however, with the exception of device D1, all appear to function similarly with changing bias voltage. There is a linear response in the positive voltages, with minimal hysteresis. However, at negative voltages, the response current initially slows its decrease and then accelerates again to a breakdown voltage. There are also large hysteresis effects at negative voltages.

It is notable that the X-ray photocurrent is clearly distinguishable from the dark current also. However, the magnitude of the current response is highly variable between devices, some near 20 nA while others up to 500 nA. The larger differences are due to some devices being measured without contact to the guard rails, as the contact was not always reliable.

Nevertheless, it can be at least be inferred from this diagram that some of the better performing devices for direct detection would be D3 and D7 for their strong response even with guarding rails, and also the sharper diode like performance at the low negative voltages.

However, there is large disparity between pixels within the same device, which can be seen in the large variation in all X-ray induced responses seen in figure 6.13.
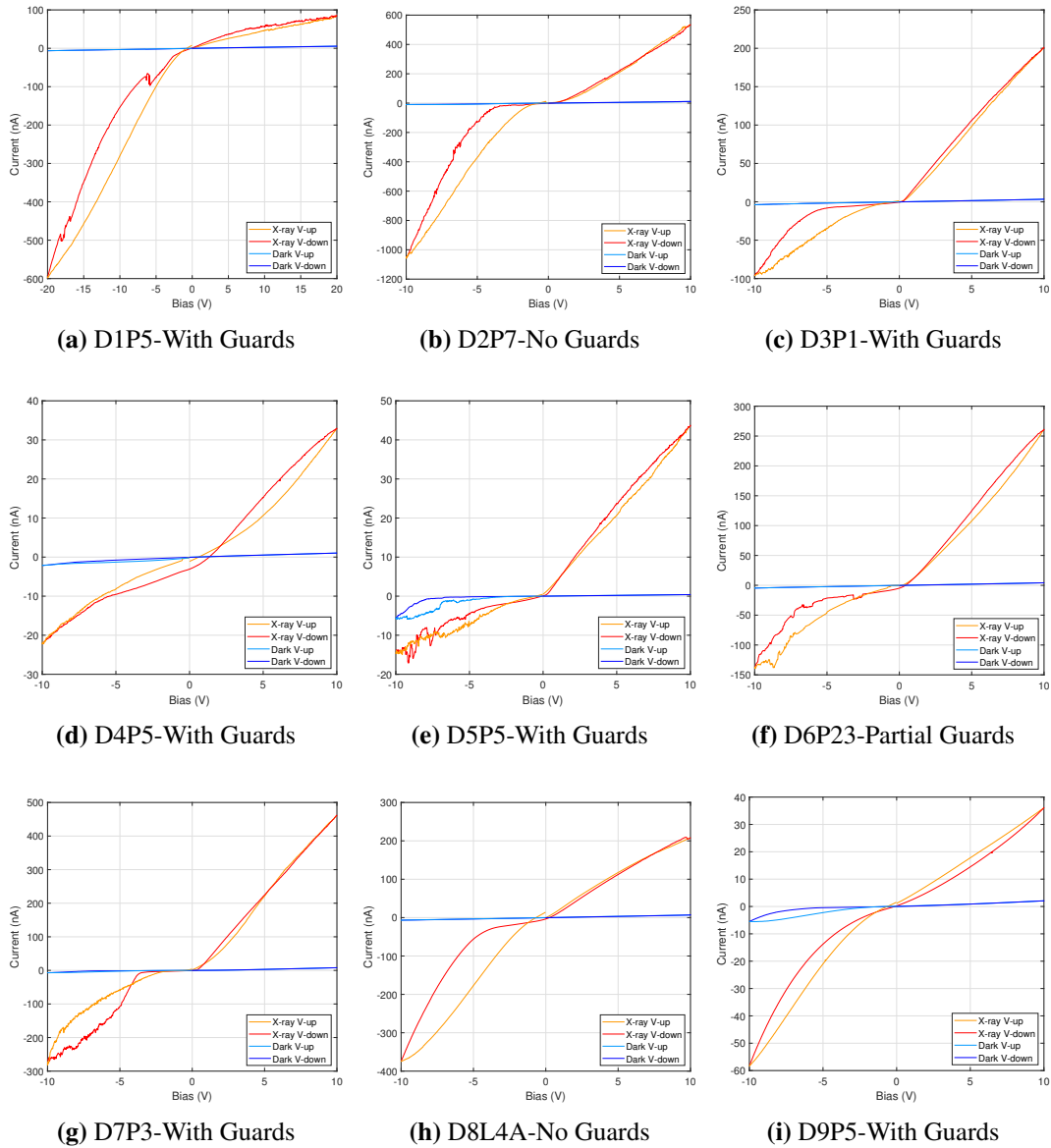
Figure 6.12: Responses taken from each device comparing the X-ray response to the dark current over a range of voltages, most ± 10 V. X-rays are set at $100\,\text{kVp}\,9\,\text{mA}$ for a dose rate of $1.7\,\text{Gy}\,\text{s}^{-1}$

A large portion of this variation can be placed upon the fact that upon placement of the probe, under the pressure it exudes, some contact can be scratched from the surface, and with multiple attachments and detachments this will erode the active area of the pixel. This fact is true of the guard rails also, which can then decrease the modulation of the current from other areas of the device.
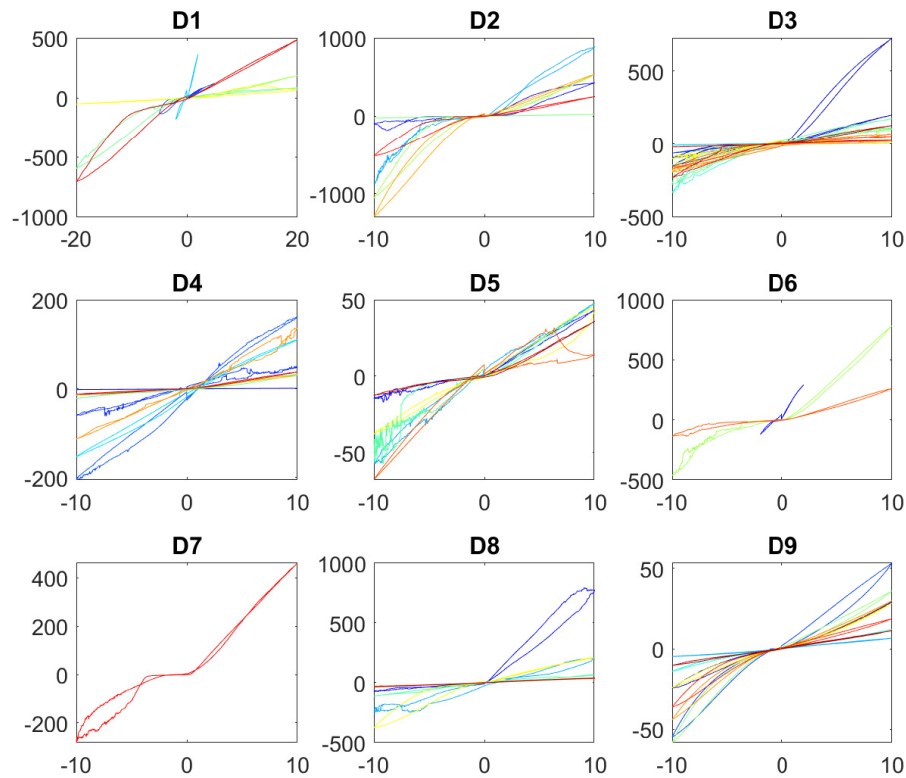
Figure 6.13: X-ray responses of all measured pixels on each device to show the spread of response values observed and inter pixel variability. Traces are coloured by red to green to blue for devices from 1 - 9.

Some peculiarities were observed in certain pixels behaviour, as shown in figure 6.14, whereby the dark current was initially stable and following an ohmic relation, but upon reaching a negative voltage of great enough magnitude, the current would sharply increase, or rather the resistance would sharply decrease. This in itself is not unexpected of diode behaviour, however the uncertainty arises as the voltage begins to be reduced yet the resistance continues to also decrease such that in D3P3 in figure 6.14a reaches maximum current at -9 V. This perhaps indicates that there are anomalous electron or hole trap states that have a delayed effect on the electric field within the material. Another explanation could involve electric field

induced ion migration through the crystal medium that leads to an enhanced cur-
rent, which slowly reset after the electric field is reduced. In either case it leads to
an extreme hysteresis where a large breakdown is induced at $sim-10$ V that would
otherwise have continued to accelerate to higher currents, but the reduction of the
voltage slows this until it is finally counteracted and reduces again.

Yet furthermore, in figure 6.14b, the voltage is taken to -20 V, where a sim-
ilar phenomena occurs, leading to a much less stable signal and recovery, but then
decreases again from -15 to -10 V. On top of this, the dark current raises from
nA up to 7 µA, which corresponds to a resistivity of $1.15\pm0.11\times10^5\,\Omega$ cm. After
X-ray exposure under the same IV-curve, which exhibited a similar response and
magnitude to the dark current breakdown, and with no external influences the device
reverted to an ohmic contact with only a maximum of ±10 nA. This behaviour is
very difficult to determine the origin for, as there are many uncertainties about exact
material composition, contact displacement & degradation, local inhomogeneities
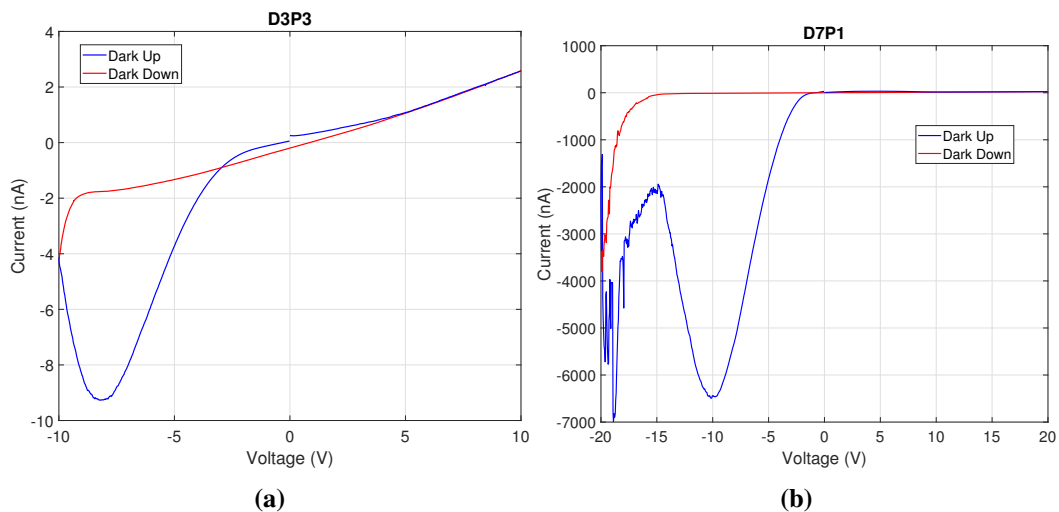
Figure 6.14: The dark current observed in two separate devices, D3 and D7, where the
higher negative voltages exhibit some unusual runaway breakdown character-
istics.

or even mobile ions, as seen in ThBr[73]. However it is also a rare instance across all device tests, so can be considered a confounding effect upon certain tests.

The bias voltage is a very fundamental parameter for operating these devices. In figure 6.15 Device 1 shows a response to increasing kV p with the bias voltage set at $\pm 1, 5, 20$ Volts. Shown on a logarithmic scale, there are various interesting behaviours observable here. Firstly, it is clear that the dark current is not overly stable during an exposure process, more so in the negative voltages, where it either steadily changes or appears modified by the exposure to X-rays. At $-20\,\mathrm{V}$ the most pronounced change occurs where the dark current and response increases by 1.5 orders of magnitude, which is due to an effect discussed earlier in 6.2.2.1 where the material resistance is temporarily lowered. There is a similar though much reduced effect at $-5\,\mathrm{V}$.
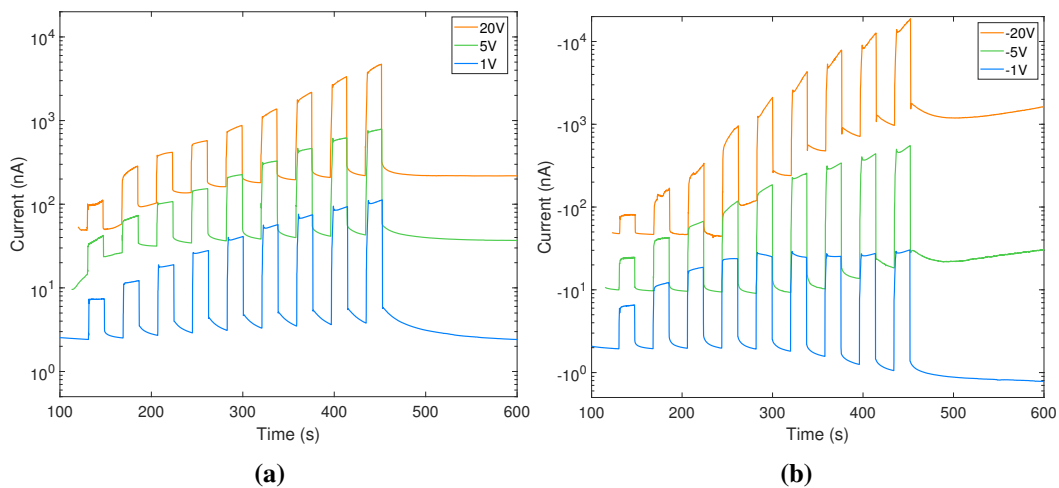
Figure 6.15: The response of Device 1 Pixel 1, under multiple positive and negative voltage biases and exposed to regime 1 (X-ray spectra of 20–100 kV p)

Figure 6.16 shows a deeper analysis into the functionality of D1P1 which can help understand some of the contact properties of this design. Initially, at 0V bias, the photoactive area can read out a positive photocurrent of a few nA, which is an
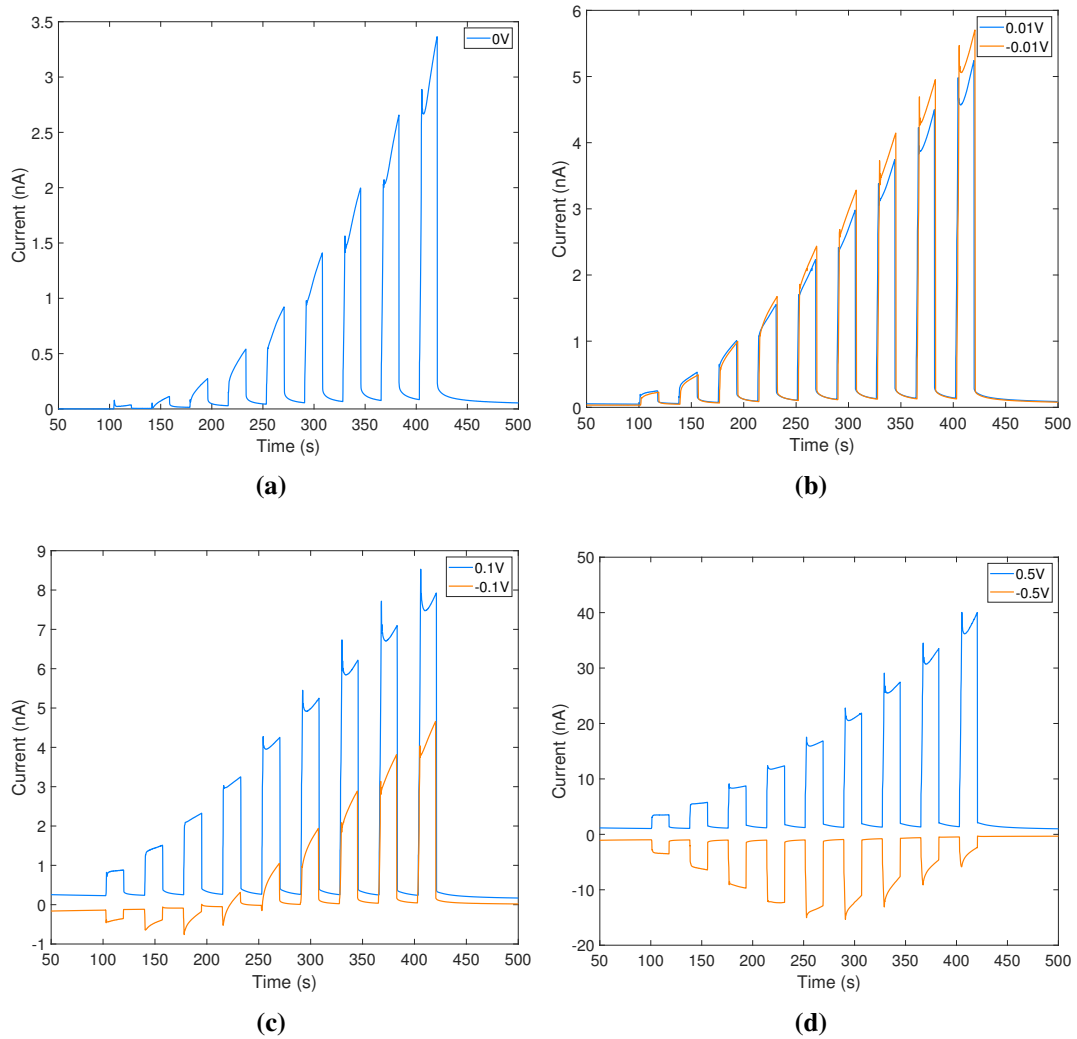
Figure 6.16: A set of responses to scheme 1, of increasing from 20 to 100 kVp, for D1P1 at a range of small voltage biases demonstrating the photocurrent polarity dependence upon the energy of the X-ray beam: a) set at 0V b) ±0.01V c)±0.1V d)±0.5V

expectable outcome, as the gold contact atop the crystal will set up a local electric field that serves to ferry generated holes out of the crystal and generate a current. The first peculiar behaviour emerges when small biases of ±10 mV are used, as the response values increase approximately twofold, indicating that these biases leads to additional charge absorption, however, both result in a positive current. Increasing the bias to ±100 mV leads to, in the positive bias, a linear expected response step, but in the negative bias, an initially negative photocurrent becomes positive as the

kV p of the X-ray spectrum increases. Finally, at ± 500 mV the response is almost perfectly symmetrical about the x-axis at 0 until it begins to decrease again from 60 kV p and upwards.

Firstly, it can be reasoned that 10 mV is not enough to overcome the inbuilt electric field given that -100 mV was not enough to reduce the majority of it. The increase in response therefore, is due to an effect where the resistance of these devices changes with exposure time, as these exposures were taken one after another, which would also explain why there is more response in the -10 mV set than in the positive counter part. However, this does not explain the later effects.

The response is proportional to the kV p of the beam, and so is either dependent on the X-ray penetration, power output of the beam, or both. However, the X-ray penetration is the most likely cause for an effect such as this, as the increase in penetration leads to charge being deposited farther away from the gold read out contact. What is unexpected is that the charge initially begins negative and becomes positive with greater kV p, since, as seen in figure 4.13, at energies of 20 keV X-rays cannot penetrate much deeper than 100 μm within the medium. Thus the vast majority of electron-hole pairs will be generated within or close to the Au/CsPbBr$_3$ depletion region, which naturally extracts the holes while pushing the electrons deeper into the material, creating a flow of charge positively towards the ammeter. As a larger number of photons become more penetrative, the potential difference across the semiconductor should account of the majority of charge carrier flow, as these absorption sites are much further within the material from the depletion regions. Figure 6.16c is a reaction that is opposite of what would be expected if this

were the case.

Instead, it could be related to the total energy deposition per second, whereby, electron and hole traps are being filled in greater numbers, so much so as to negate the electric field generated by the small negative potential difference and reverse the direction of the flow of charge. This would explain why a larger electric field is needed to overcome this internally generated potential difference. This is further backed up by the observation that during the course of exposures, the total photocurrent increases while at a constant dose rate, as this internal electric field intensity is mounting. This notably changes by an inverse exponential, which can be related to the filling of random available traps.

Figure 6.17 helps understand this by showing a similar response when cycling the bias between +2 and -2 V, where the device is exhibiting an intense hysteresis during X-ray exposure at negative voltages. Since the X-rays are exposing for the entirety of this run, ($100\,\mathrm{s}$), the effect that occurs in figure 6.16d appears sensitive to the duration of exposure from first becoming negatively biased, since for example, at $-0.5\,\mathrm{V}$ the value at first is $-40\,\mathrm{nA}$ and then reduces to $0\,\mathrm{nA}$. This shows an exposure time sensitive behaviour, complicit with a self modifying electric field due to exposure. These effects reset after some time, as can be seen in figs. 6.17b and 6.17c, however the hysteresis is more intense, likely due to the larger voltage. It can be reasonably concluded that these devices exhibit some slow incrementing and relaxing resistance dependency on X-ray exposure that is not insignificant at low voltages.

(a)

(b)

(c)
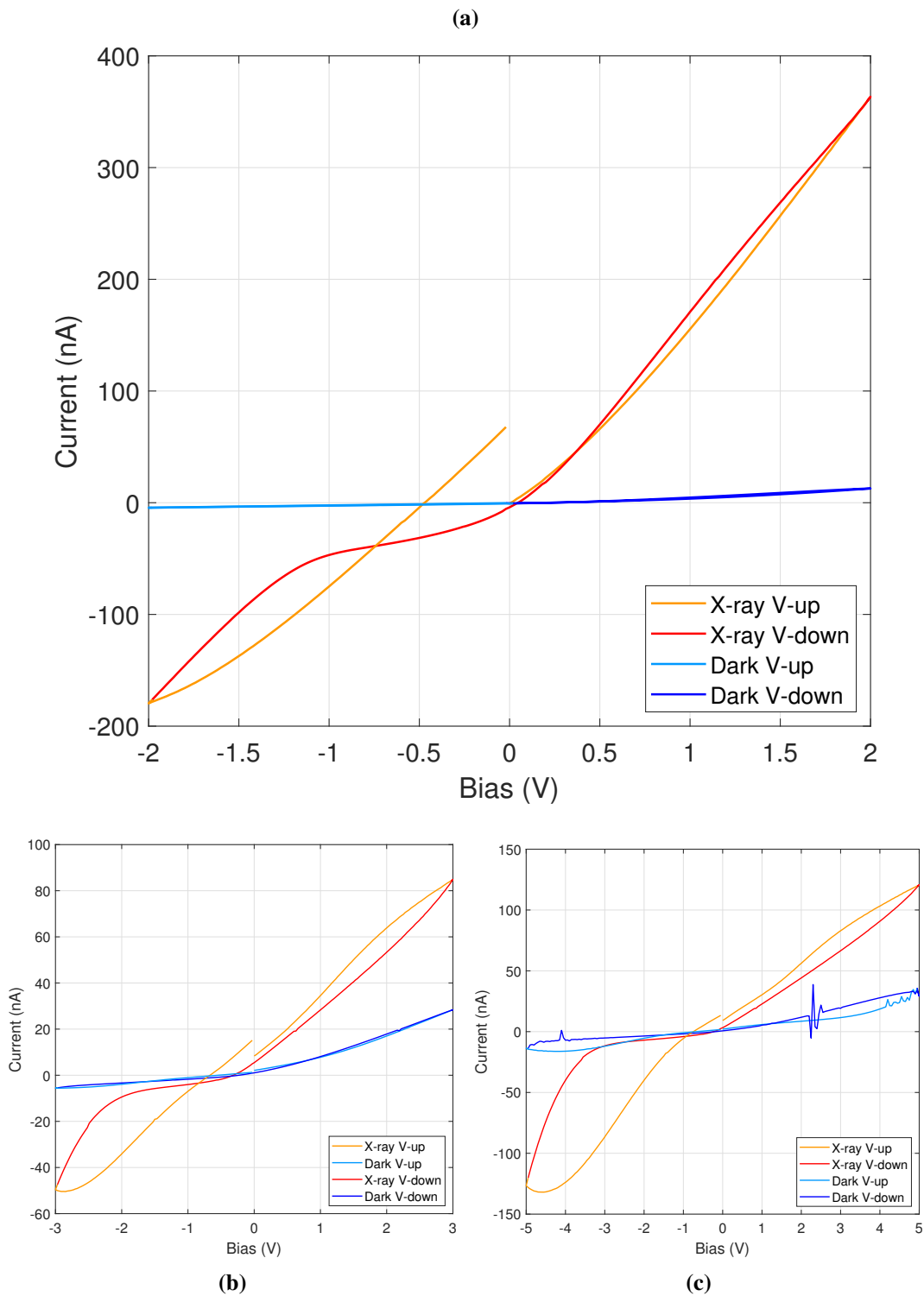
Figure 6.17: A set of bias curves taken from device D1P1, showing the device photocurrent for $\pm$2–5 V when in the dark and under direct X-ray exposure (100 kV p, 9 mA). The 3 V exposure in b) is made behind a 10 mm aluminium filter hence the reduced photocurrent. The spikes in c) are due to background vibrational disturbances.

The result of running the simulation on an active area ($0.844\,\text{mm}^2$) of these perovskites is shown in table 6.1. For each tube voltage the total energy deposited per second in eV is shown, and that is then divided by the bandgap and multiplied by two for both holes and electrons, to find the number of charge carriers generated. This number is shown in $\mu\text{C}\,\text{s}^{-1}$.

Tube Voltage	Energy Deposited	Generated charge
kVp	TeVs^{-1}	μA
20	16.2	2.19
30	20.4	2.76
40	24.3	3.29
50	27.9	3.77
60	31.5	4.26
70	34.8	4.70
80	38.3	5.18
90	41.7	5.64
100	44.9	6.07

Table 6.1: A table of simulated values of the energy deposited and charge generated per kVp of the tube

Device and Pixel	Resistivity	Charge Collection Efficiency at 100 kVp	Sensitivity at 100 kVp	$\mu\tau$ product
	$\Omega\,\text{m}$	%	$\mu\text{C}\,\text{Gy}^{-1}\,\text{cm}^{-2}$	$\text{cm}^2\,\text{V}^{-1}$
D3-P2	$(3.2\pm0.6)\times10^{8}$	2.1 ± 0.5	170 ± 34	$(2.5\pm0.5)\times10^{-5}$
D4-P2	$(1.9\pm0.5)\times10^{9}$	0.90 ± 0.18	76 ± 14	$(1.1\pm0.1)\times10^{-5}$
D5-P2	$(1.4\pm0.4)\times10^{9}$	1.00 ± 0.25	80 ± 16	$(1.1\pm0.1)\times10^{-5}$
D7-P3	$(1.0\pm0.2)\times10^{8}$	0.27 ± 0.05	23 ± 5	$(3.3\pm0.3)\times10^{-6}$
D9-P2	$(8.7\pm1.6)\times10^{8}$	0.60 ± 0.12	45 ± 10	$(6.5\pm0.5)\times10^{-6}$

Table 6.2: A table of extracted values for resistivity, charge collection efficiency and $\mu\tau$ of multiple devices. Errors are calculated from error in estimation of the active area, as this is the largest uncertainty

Table 6.2 shows a compilation of the device resistivities, Charge Collection Efficiency (CCE) and $\mu\tau$ products. The resistivity, ρ, was calculated with the relation of

$$\rho = R\frac{A}{l} = \frac{\delta V}{\delta I} \cdot \frac{A}{l} \tag{6.3}$$

where R is the resistance, A is the active area of the contact, and l is the thickness of the sample. The resistance value was taken from the gradient of the dark current IV-curve at positive voltage linear segments. The CCE was calculated through finding the number of charges that should be generated each second by the X-ray beam according to the bandgap of the material (2.35–2.40 eV) and comparing that with the photocurrent measured. The CCE was then used to find the $\mu\tau$ through the Hecht equation (6.2). Device 1, 2, 6 and 8 cannot be evaluated as all measurements involved an unknown active area due to the lack of guard contacts. Uncertainties were given by the standard deviation of measurements from each pixel measurement.

The first observation to note is that the charge collection efficiency is low for these devices, as low as 0.27 %. This is reflected in the low values for sensitivity, however, comparable to the values found by Wei et. al. [74], of $80\,\mu C\,Gy^{-1}\,cm^{-2}$. As a result, the $\mu\tau$ values for all devices are in the range of $10^{-5} - 10^{-6}\,cm^2\,V^{-1}$. This is likely due to the pressed pellet nature of these devices, leading to grain boundaries that inhibit the free flow of charge through the active volume, decreasing carrier mobility. The low mobility perhaps also leads to a low dark current when compared with typical devices [75]. This low mobility implies that the charge being extracted is mostly from within a few tens of microns close to the front contact, as

well as some from the back when the X-ray beam begins penetrating enough. This is
not an unexpected result, however, as these devices are vastly different from single
crystal based devices.

6.4.2 Radiation Hardness

Some instances of radiation degradation were observed in devices, whereby
long exposure generated a slow decrease in the device photocurrent. One instance
can be seen in figure 6.18, where a 20 minute exposure with the X-rays at maximum
output leads to a 21 % decrease in signal response over the course of the exposure
and the response to radiation afterwards decreases by 14–28 %.
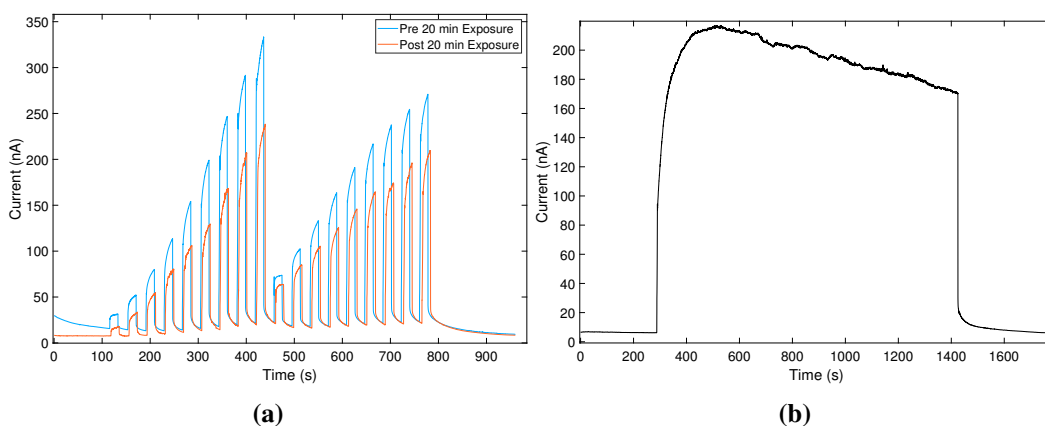
Figure 6.18: Exposure of device D7P3 exhibiting an instance of radiation degradation after
20 minutes exposure to a total of 2.0 kGy, biased at 10 V in all tests

If this is only a temporary offset, then the change is perhaps a result of elec-
trons or holes entering long term trap states that removes them from the overall
conduction current, similar to in the instance of TLD from chapter 3. If it is more
permanent then a physical change to the lattice is being made by the radiation, such
as displacement of ions from their lattice sites. Unfortunately no long term follow-
up measurement were made, so it cannot be confirmed if this reset is a permanent

effect in these devices, and remains to be determined in future work.

6.4.3 Response Times

In order to measure the effect of charge mobility in the perovskite, time based analysis of the devices is crucial. Initially, measures were made on the time response using a beam chopped at 0.8 Hz, with an exposure window of 35 ms, using the Keithley at the fastest readout rate. A sample of these results is shown in figure 6.19. Unfortunately the readout rate is no where near great enough to observe the rise and fall time of the sample under test, however this at least confirms the response rise time is less than $55(13)$ ms, and that the fall time for 90% relaxation is within $110(26)$ ms.
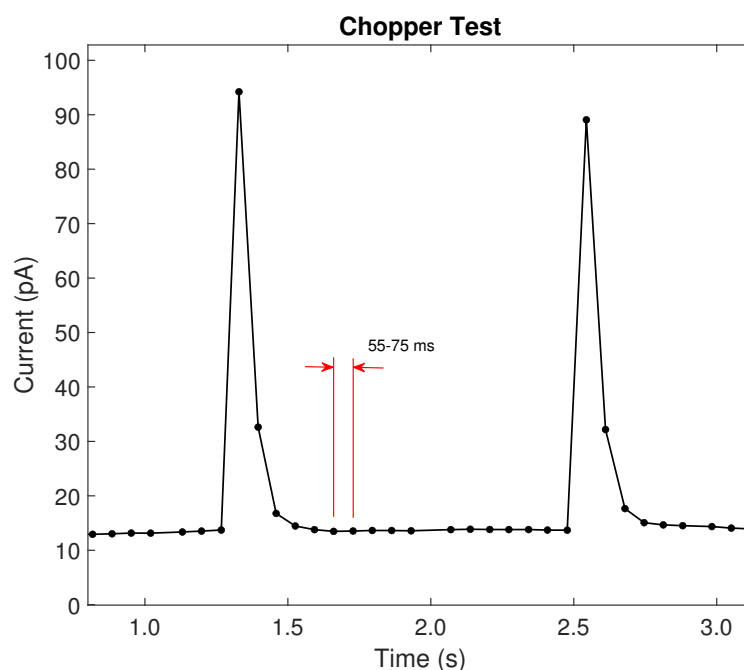
Figure 6.19: The response of a select pressed powder device to X-rays as filtered through an X-ray chopper running at 0.8 Hz, measuring using the Keithley 6187 at its maximum stable read speed.

Further to this test, a modified furnace sample was observed under exposure

while utilising a voltage amplifier to observe the signal at a much higher time resolution. This sample was used for initial apparatus testing purposes, and was not ideal for exact value determination. However, only one set of acquisitions was taken, where figure 6.20 shows the clearest measure of the X-ray response. Rise time and fall time were calculated as the time from 10–90 % of full response and relaxation. The results here are limited but nonetheless, given a rise and fall time of this duration, it would be feasible to operate similar potential devices at 30 Hz. It would be expected that further tests would yield lower response times purely because this was carried out on a non-ideal sample, for initial test purposes. However, without standardisation to the test sample, it is not possible to draw any solid conclusions on the charge carrier mobility in this or other samples.
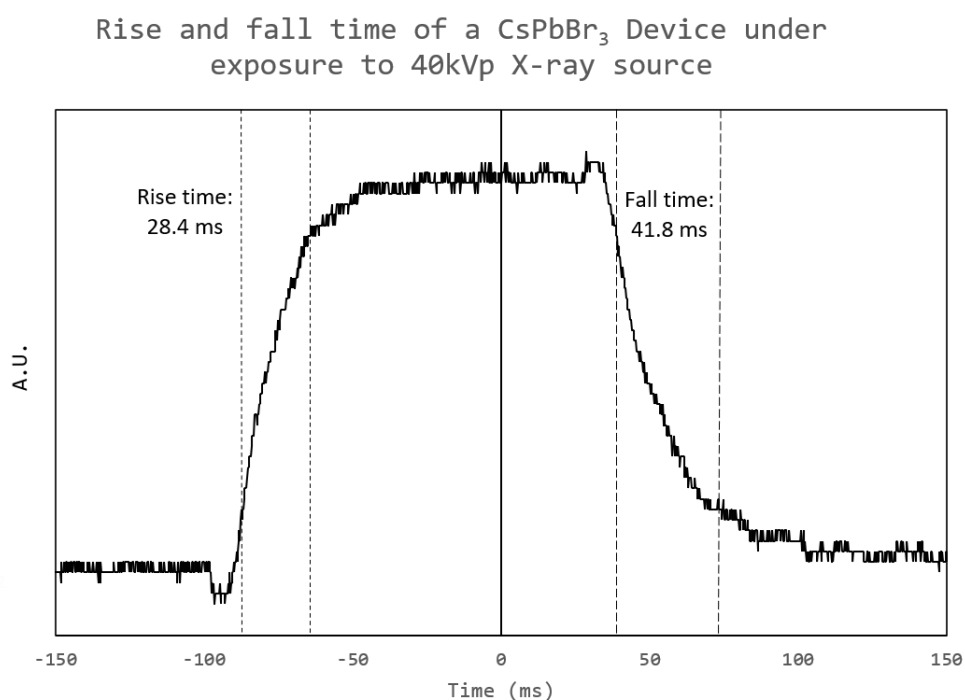
Figure 6.20: The response time of a furnace pellet sample biased at 4.75 V under a chopped beam of 40 kVp X-ray, with the calculated rise and fall time shown. The chopper used a 1.0(5) ms shuttering time

6.5   Channel Device Response

Device 8 of the final samples featured a novel readout mechanism for X-ray detection, and the first results of this are shown in this subsection. The readout contact is placed atop the surface of the sample, but X-rays are directed in through the exposed side of the device. These contacts shall be referred to as lateral pixels as the readout contacts are orthogonal to the illumination beam. The testing mechanism involved placing the needle probes down on each of the 3 channels, labelled A, B and C in order of depth within the sample and also channel length, for each channel line (L1-L6).

In figure 6.21 the main form of experiment run on this device is shown. This example is where there was no filtration applied to the beam before reaching the device, and the beam was collimated down to 1 mm diameter by tungsten pinhole windows to reduce backscatter induced charge. The sample was translated across this laterally to find the area of greatest response, and thus the centre of the beam. The step at the beginning of the data for channel A marks the point at which the X-ray tube is switched on. Unfortunately, the device was not able to be synthesised with guard rails either side of the active channels, so the charge capture area is inflated over the actual width of the pixels, however, the entire channel line was simultaneously grounded during readout, so there was no crossover in capture area.

What can initially be observed in figure 6.21 is the clear relation of response current to increasing kVp, and how it diminishes for each channel deeper within the perovskite, which confirms that X-rays that are being absorbed at the first lat-
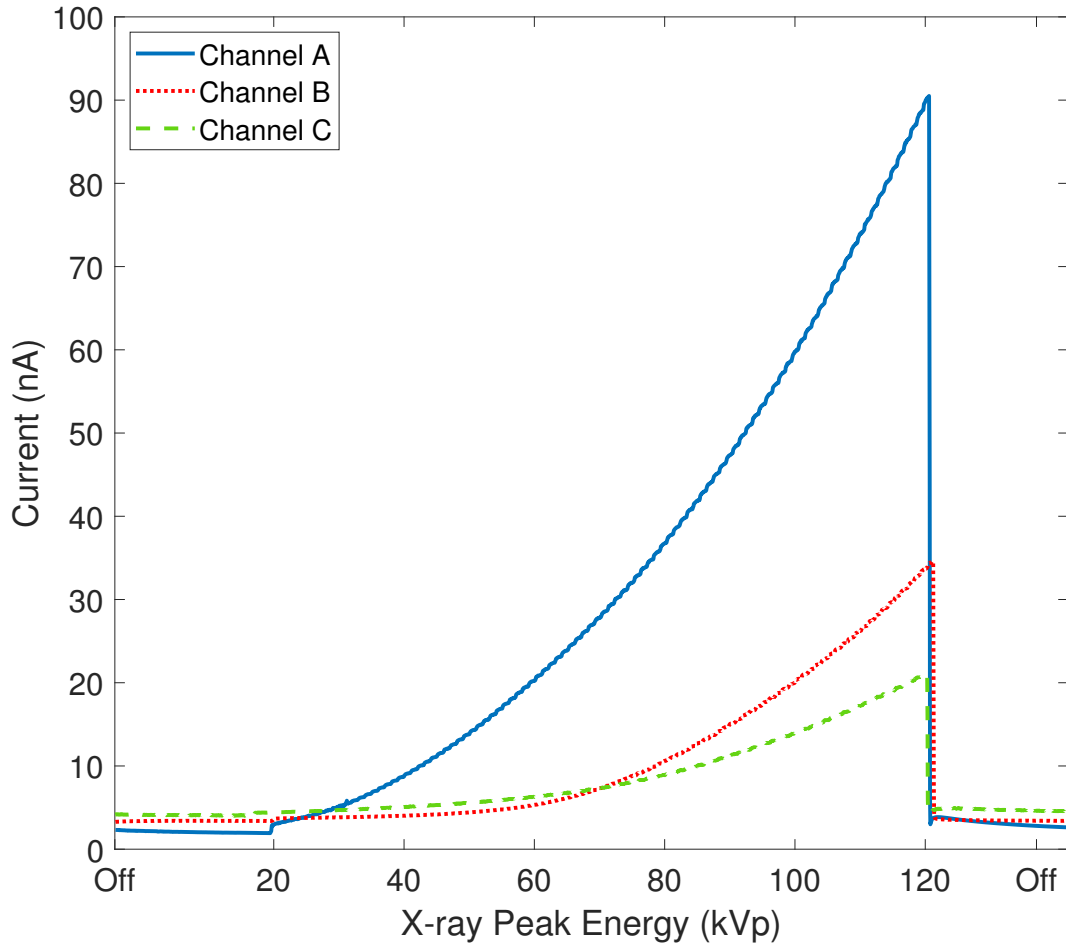
Figure 6.21: The photocurrent response observed in each channel of D8L5 exposed to an unfiltered but collimated beam, where X-rays are initially off, then started at 20 kVp increased to 120 kVp, and switched off again. The tube current was held at 7 mA.

eral pixel, A, are not contributing the photocurrent in the following lateral pixels, B and C. Also, that from the lowest kVp, channel A shows response, however, the deeper channels don't begin to increase sufficiently until reaching a higher kVp, indicating that greater energy is needed to penetrate deep enough to contribute to that readout current. Additionally, the dark current for each channel is greater the deeper within the perovskite. This is because, as each channel is longer than the previous, increasing length increases the charge capture area and thus the dark current, which simply confirms that the channels are indeed collecting over greater areas than their

predecessors.

All this together confirms that the device is functioning, at least basically, as predicted by the design. Ideally, the response current would be of closely matching magnitude between channels at these energies, however this would require channel A to be of $\sim 100\,\mu m$, which is too small for the probe station to reliably contact. As a result, the largest portion of the beam energy is absorbed within the first layer of $500\,\mu m$.

The more major interesting use of this device design is highlighted by analysis of the graphs in figure 6.22, where each channel of two separate lines are compared, while being exposed to X-rays under multiple filtration materials and thicknesses. This simulates the effects of various imaging or detection environments and helps to show how a device may respond to imaging complex mixtures of metals.

Beginning with analysis of what occurs in Channel A of L6 in figure 6.22a and 6.22a, at low energies there is a difference made to the response by even small filtration such as the $220\,\mu m$ of Aluminium. However, this filtration creates less contrast at higher energies, where it becomes almost indistinguishable. The thicker the filtration, the lower the response and notably the higher the energy required to noticeably increase the photocurrent, which in an X-ray image would correspond to areas of high and low contrast. For example, in channel A, at the maximum of $120\,kVp$, the $0.9\,mm$ of Steel produces a little less than half the unfiltered response, and the $1\,mm$ of Lead is close to 0 response relative to the maximum. These reactions are as would be expected from a standard pixel.
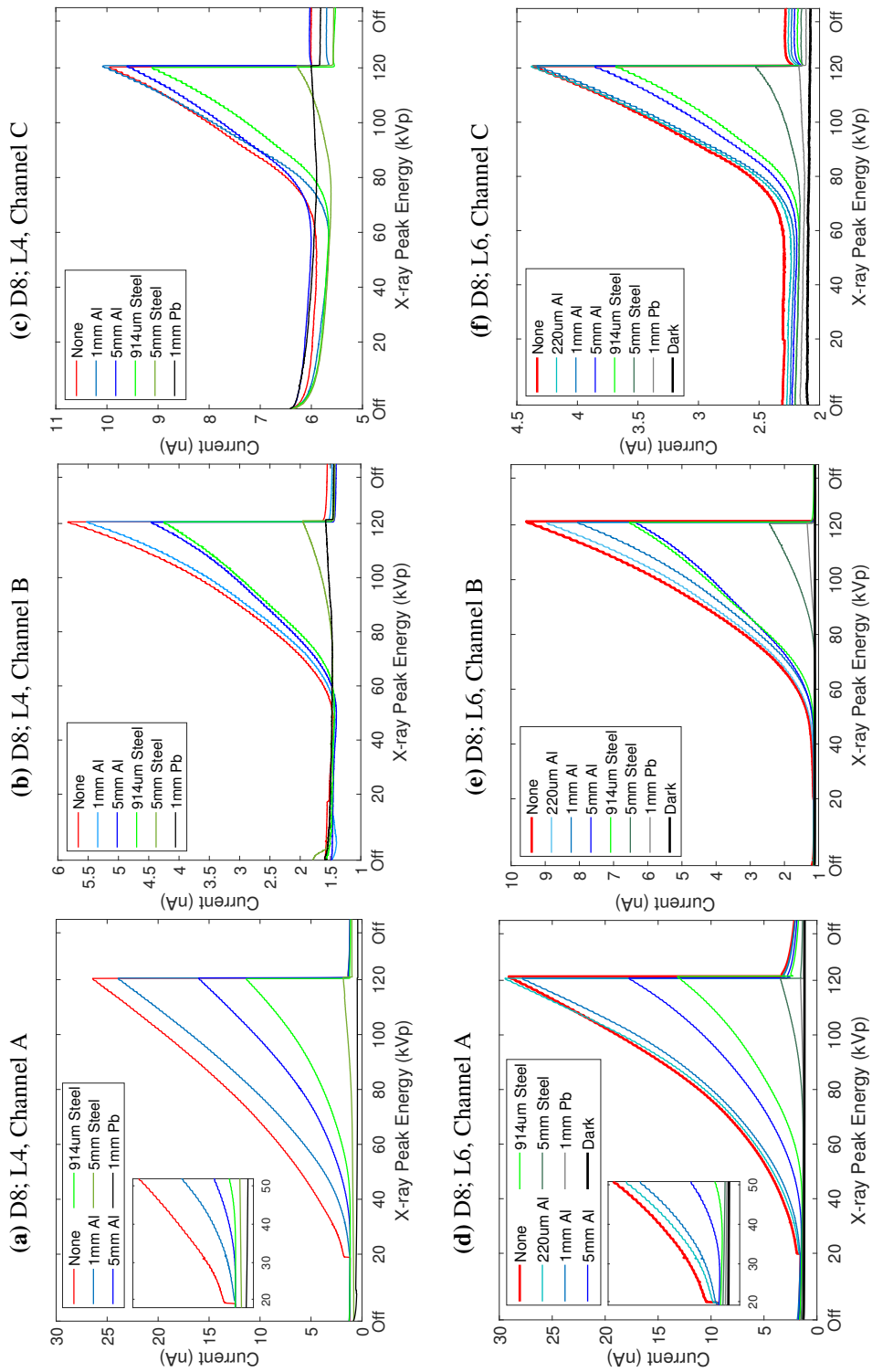
Figure 6.22: A set of graphs taken from two lines in device D8, L4 (a-c) and L6 (d-f), where X-rays are increased from 20–120 kVp, with filtrations of various materials and thicknesses applied to the 1 mm X-ray beam. a) and d) include an inset to highlight low energy contrast. A logarithmic plot variant can be found in appendices; figure 8.4.

Further into the device, in channel B, the response to X-rays does not begin to appear until around $50\,\mathrm{kVp}$. But more pointedly, there is a differing level of contrast between filtrations that were more effective in channel A and are less effective at channel B. For example, in channel B there is only a very small difference between the responses observed in the $5\,\mathrm{mm}$ of Al and $0.9\,\mathrm{mm}$ of Steel, but in channel A the contrast is much greater. Additionally, the response from the $5\,\mathrm{mm}$ of Steel is relatively more prominent in channel B.

Finally, in channel C, due to the strong perovskite self filtration subsequent charge extraction in channels A and B, it takes until 65–$70\,\mathrm{kVp}$ to generate signal in this channel. The lighter filtration, including the $1\,\mathrm{mm}$ of Steel produced much smaller decreases in the signal compared to previous channels and while the harder filtration shows greater contrast, where even the lead begins to display a resolvable response at high energy.

What needs to be considered is that the absolute photocurrent does decrease for each layer beyond the first, while the dark current is increasing so that the absolute response is diminished with greater filtration. However, the relative response is what can be measured, and with calibration against an unfiltered beam and with proper signal amplification, this design can distinguish differing energy dispersions as a result of the beam attenuation prior to entering the device to display a range of contrasts depending on the energy of the photons. As a result, this can essentially take 3 separate views of the same object in different energy modes simultaneously, giving general information of the energy of the photons being measured.

Table 6.3 compiles the responses of the channels to the X-ray beam at 3 select

Selected Energies (kVp)	Channel A			Channel B			Channel C		
	40	80	120	40	80	120	40	80	120
Unfiltered (nA)	3.27	11.21	29.03	1.21	3.2	9.54	2.3	2.57	4.37
Dark Current (nA)	1.2	1.19	1.17	1.11	1.11	1.11	2.1	2.09	2.08
Absolute Error (± nA)		0.15			0.02			0.06	
220 μm Al	0.83	0.94	1.01	0.6	0.92	0.931	0.7	0.9	1.00
1 mm Al	0.69	0.87	0.96	0.2	0.78	0.823	0.6	0.8	0.98
5 mm Al	0.24	0.50	0.60	0.3	0.68	0.619	0.5	0.6	0.77
0.9 mm Steel	0.10	0.32	0.43	0.3	0.66	0.644	-	0.5	0.70
5 mm Steel	-	0.03	0.08	-	0.03	0.157	-	-	0.19
1 mm Pb	-	-	0.01	-	-	0.026	-	-	-
Ratio Error (±)	0.10	0.02	0.01	0.3	0.01	0.003	0.4	0.2	0.04

Table 6.3: A table of the responses for each channel of D8L6 observed at 40, 80 and 120 kVp as a ratio between the unfiltered response and the dark current. Errors in the ratio were taken from the standard deviation of the dark currents observed in the devices, as this was the largest source of variation

energies along the scale under test. Ratios are taken between each filtered response and the unfiltered beam, after subtracting the dark current from each. The error in the measurement is considered to be the standard deviation of the dark currents observed at the beginning of each exposure, as this sometimes shifted dramatically, as seen in figure 6.22. Ratios are marked '−' if the response was too low to be considered existent within the range of error. Nonetheless, this set of ratios can be used to observe the magnitude of attenuation of multiple materials and help to identify them. The device here operated under non ideal conditions as the channels were not as well defined or divided as could be achieved and yet there is clear

contrast between each layers detection of photons corresponding to their energy.

6.6 X-ray Imaging Tests

X-ray imaging tests were performed to both observe the spread of photoelec-tron absorption and also to demonstrate the capability of the perovskite for imaging purposes in general. This was performed through translation of the sample by steps in x and y coordinates in a plane behind some sample, to aim to compile an image from the photocurrent reading at each location. It should be noted that frequently these images contain artefacts and areas of sharp noise that lower the overall fi-delity, this is due to the translation of the stage affecting the contact pressure of one or more test probes involved in the measurement process. The change in pressure can lead to sudden changes in connection quality that sharply increases or decreases the photocurrent, which leads to these artefacts. This should be considered an effect of the measurement system rather than the perovskite sample itself.

Initially, a pixel on D3 was tested by exposure to a well defined X-ray beam of $400\,\mu m$ diameter, the results for which are shown in figure 6.23. The bias voltage was varied from $2\,V$ up to $20\,V$ to observe the differences in charge collection based on position around the beam. The pixel was surrounded entirely by a guard ring, so the active area was close to the true size of the pixel.

The main observation of this data is how the most active region of response shrinks over the range of voltages applied, though not uniformly. Initially, the re-gion of response is wider than the beam $400\,\mu m$ by a large margin. As the voltage increases this region becomes much more localised and the highest response region
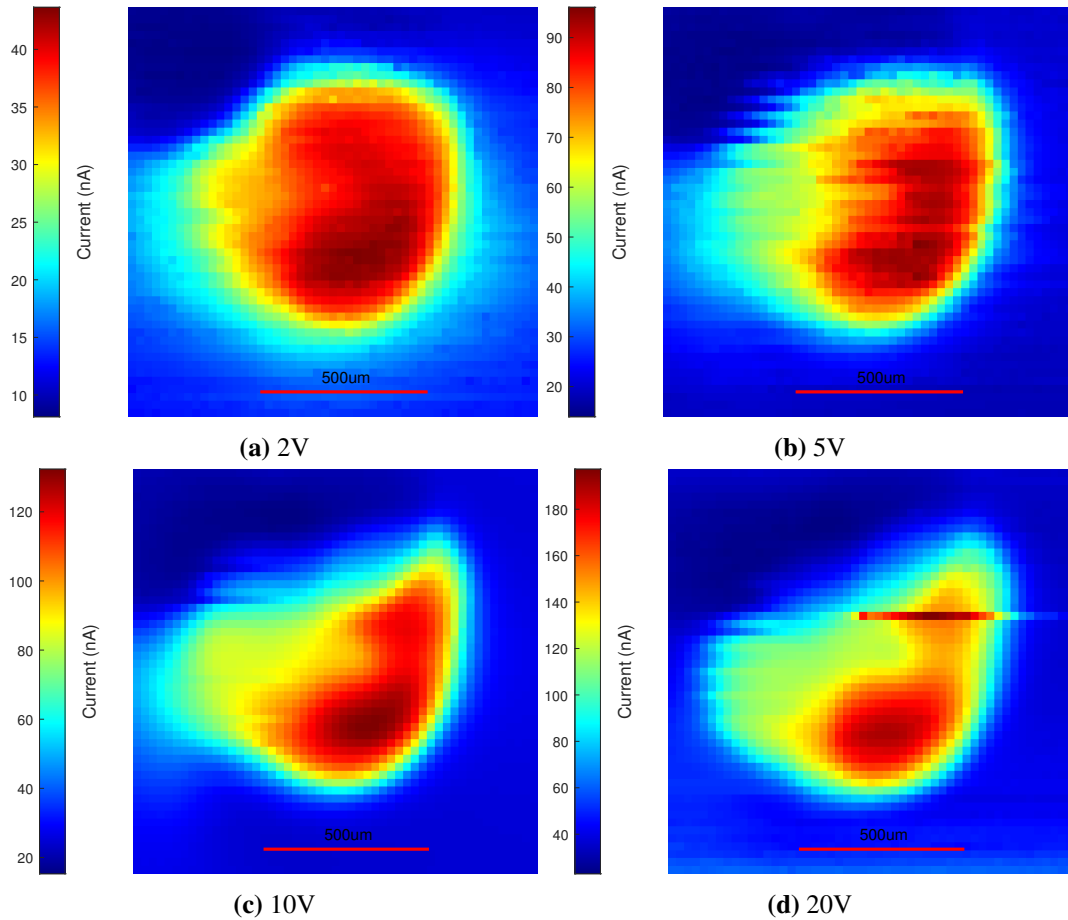
Figure 6.23: Scans of a 1 mm pinhole beam moving in steps of 25 μm over an area of 1.25x1.25mm using a 500 μm pixel biased at various voltages. Colourbars show the response current received in nA

is around 400 μm across. This suggests that there is a high degree of surface or near surface current generated by X-rays that makes its way to the electrode from the surrounding perovskite. As voltage increases, this continues to contribute to the signal, however, the depletion region also extends deeper into the material, meaning the majority source of charge carriers then come from within the perovskite, and thus the charge collection in this area is enhanced.

What this shows is that, in tandem with the bias curve data that displays no saturation current from X-ray absorption, at 20 V bias the depletion region is still very small compared to the thickness of the perovskite.

(a) Full image of the pinhole taken using a Flat Panel imaging system

(b) Image taken of the pinhole taken using a perovskite 500 µm pixel translated over 200x200 locations in 100 µm steps
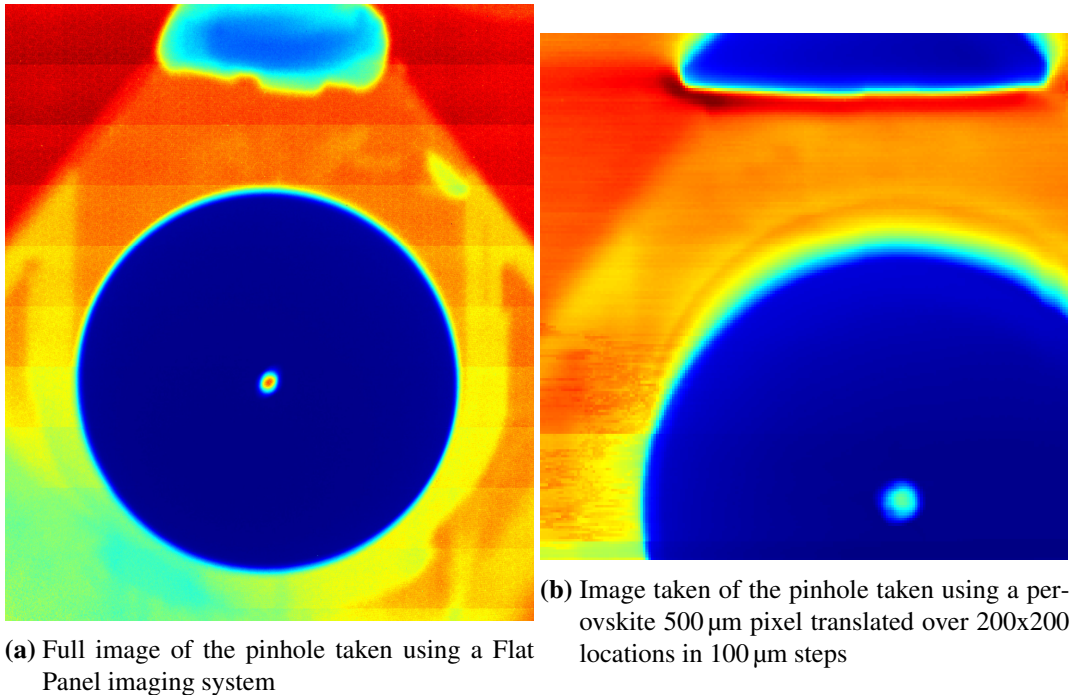
Figure 6.24: A comparison between an image taken of the tungsten pinhole (1 mm by a Flat Panel imaging system and the x-y translation of a perovskite 500 µm pixel

Device 6 offers an opportunity to test the behaviour of the perovskite in use with a pixel array, by connecting surrounding pixels and observing the distribution of charge when exposed to a known beam width. Figure 6.24 shows an image taken using a Flat Panel X-ray imaging system and an image taken by translating the perovskite pixel over a 1 mm pinhole window. Using the Flat Panel image the actual beam size can be determined accurately, with the only consideration being blurring due to detector effects however these are considered small when compared to the perovskites. The response of the perovskite pixels can then be compared in order observe how the signal from deposited photons is picked up and spreads within the perovskite.

At a distance of 196 mm from the beam focal spot and 50 mm from the pinhole, means that the pinhole's shadow increases in size by 1.17 times and thus a 500 µm

pixel width translates to 425 µm at the pinhole surface. Whereas, for the flat panel, which is set much further back, the pixel pitch of 55 µm is equivalent to 13.75 µm at the surface. Comparing these two images, it can be observed that there is a level of blurring noticeable in the perovskite image, which is to be expected from a large pixel width and by translating by only a fifth of its width with each step. However, the blurring appears more intense in the vertical direction, which implies that the pixel is absorbing charge from above and below its location out to a greater radius than laterally.
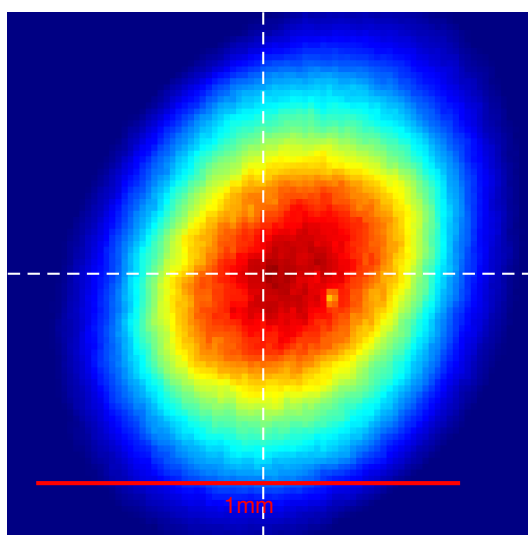
Figure 6.25: Close up of the image of the 1 mm pinhole window shown in figure 6.24a Flat Panel, where the white lines are the direction along which the FWHM is calculated in fig 6.27

A close-up of the beam spot in figure 6.24a is shown in figure 6.25, where the FWHM is between 630–720 µm. This can be considered the lower limit of spread for an image taken by the perovskite of this spot.

To investigate the spread of charge when exposed to this beam, pixels on device D6 were used to take an image of the beam and tested under 4 conditions;

– Isolated, only connecting the pixel of interest to be read out

– Partially isolated 1, grounding one neighbouring pixel as well as reading out the pixel of interest

– Partially isolated 2, grounding the opposing neighbouring pixel as well as reading out the pixel of interest

– Flanked, grounding both neighbouring pixels on either side of the pixel of interest

This would ideally manifest in decreasing the active area of the pixel of interest and thus narrow the area that the X-ray beam contributes signal in the image, creating a higher resolution approximation of the beam width.

(a) Isolated pixel

(b) Right pixel grounded

(c) Left pixel grounded

(d) Left and right pixels grounded
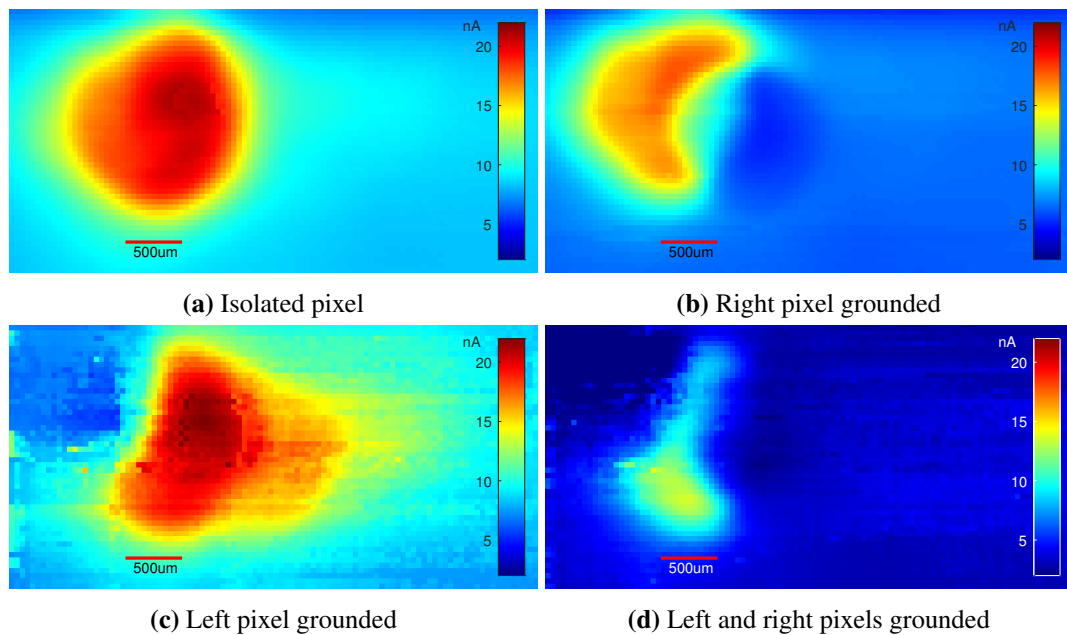
Figure 6.26: An example of the active area of a pixel reducing in size as the neighbouring contacts become connected to ground

The first test of this is shown in figure 6.26, where the pixels to the left and right are each connected at different points. Initially, in figure 6.26a, the Area of

Response (AOR) is large, 1370 μm across, much larger than the beam as shown in figure 6.25. As the right pixel is connected in figure 6.26b, the right side of the AOR decreases in intensity and in fact reduces below the background level of when the central pixel is entirely out of the beam, in the process reducing the horizontal width of the AOR. This trough of intensity suggests that as that photoelectrons under the right neighbouring pixel are immediately extracted, however photoelectrons beyond the neighbouring pixel are partially able to travel around this pixel to contribute to the read out current.

Connecting the opposing pixel, in figure 6.26c, leads to a similar, albeit noisy, effect, however, the AOR appears to shift partially to the right. This shift could be a result of the previous test, whereby the gold pixel surface may have been partially scratched away, leading to exposed surface channels in the perovskite to allow surface charge greater transport through to the pixel of interest.

Finally, in figure 6.26d, the AOR is reduced drastically by the flanking pixels both being grounded, such that most deposited charge is absorbed by the neighbours. The current outside of the AOR is also reduced, as the total active area shrinks, reducing the dark current. The shape of the AOR is not ideal, but it is clearly more vertically distributed as the locations above and below are still ungrounded.
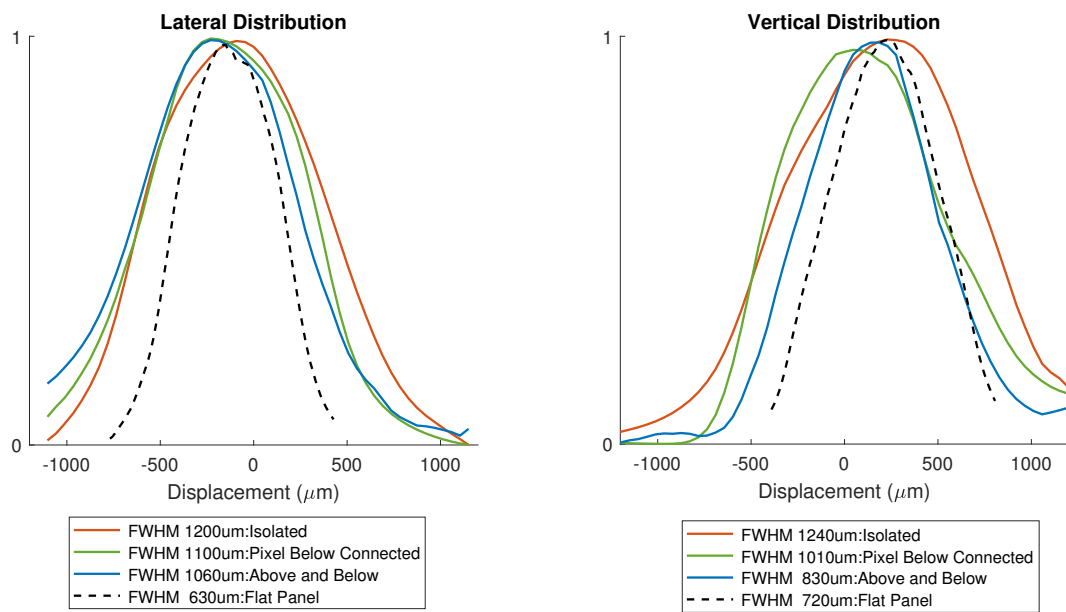
Figure 6.27: Two graphs of the peak shape for the images from figure 6.28, in the lateral and vertical directions, from which the FWHM is calculated. Fig 6.28b has been excluded as it is too noisy for a reliable measure.

(a) Isolated pixel

(b) Upper pixel grounded

(c) Lower pixel grounded

(d) Above and Below pixels grounded
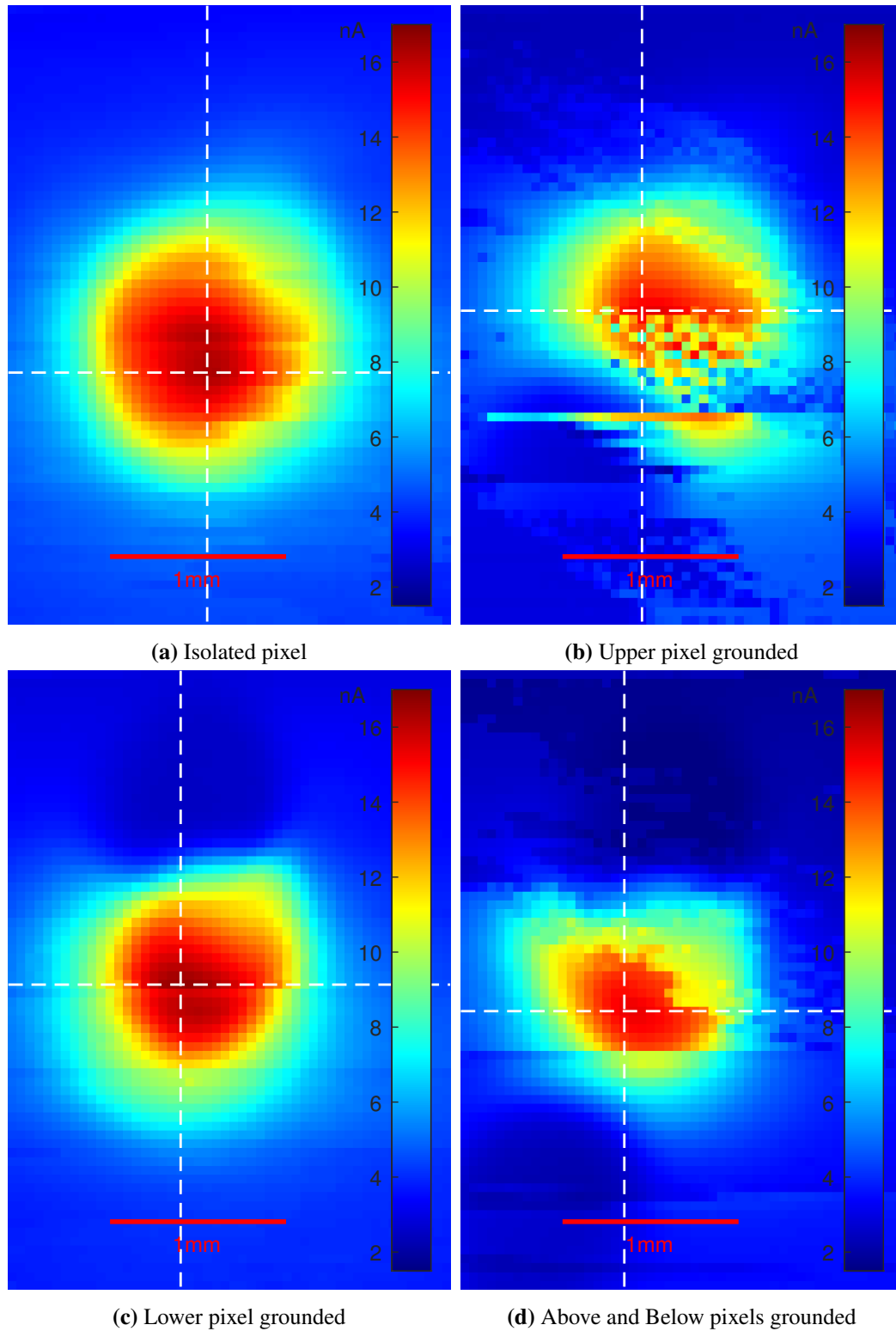
Figure 6.28: Another set of x-y translation images acquired across the beam emergent through a 1 mm pinhole window where the upper and lower pixels are connected or disconnected. White lines represent the data across which FWHM was calculated and shown in fig 6.27 and cross at the peak of response to X-rays.

Figure 6.28 shows another instance of this test, but connecting the vertical neighbours of the pixel of interest. The connection to the upper pixel does clearly lead to disconnection artefacts. Nonetheless, the effect on the AOR is clear through adding connections, with it becoming more focused with each contact added.

Lines have been drawn through the centre of the peak response in the images, which is taken as the data into figure 6.27. Here the peak shape of the images, along with the flat panel spot, are plotted and their FWHM given in the legend. The peak width only partially narrows laterally with more connections, but narrows much more in the vertical direction, as this is the direction in which the connections to the neighbouring pixels are made.

Though there are many differences between this imaging method than an actual pixel array, it serves as a simulation of the reality, whereby anticipations can be made of a functioning device. Here, certain pixels are translated through distances less than their full length, in order to observe the response 'in between' pixel locations in a standard array, which leads to blurring of images and low sharpness however improves visual fidelity. The limitation of $500\,\mu m$ pixels meant that acquiring images of resolution equal to the pixels theoretical pitch led to either far too few locations for a tangible image or far too large for the experimental system to cover.
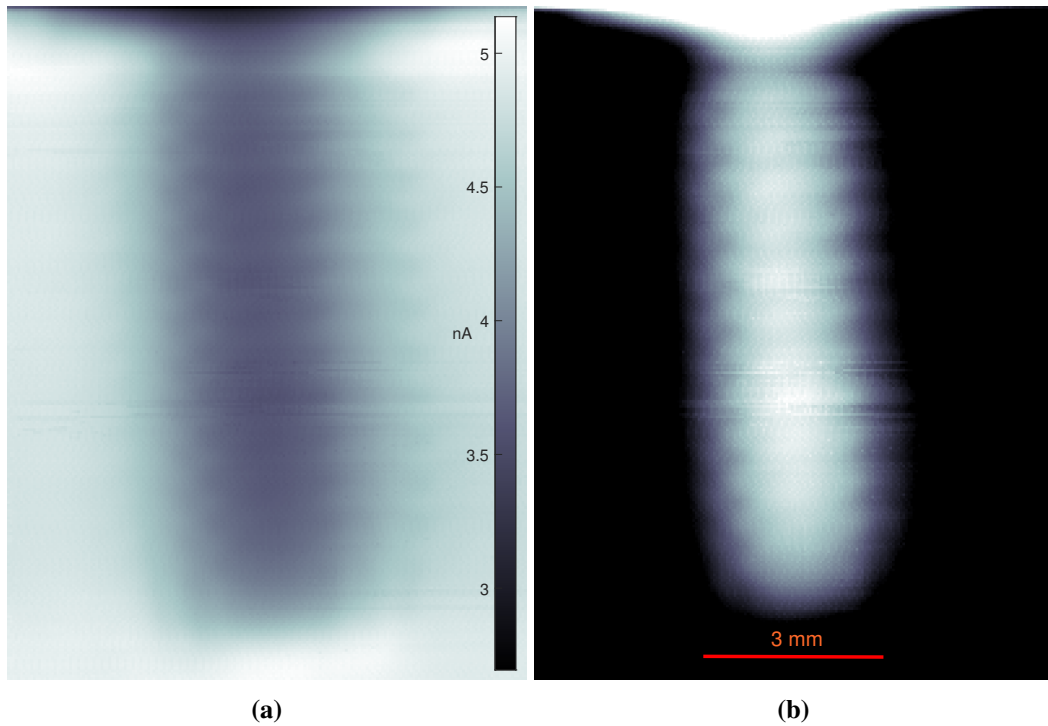
Figure 6.29: Two X-ray images taken of a nylon screw by the D6 array, X-rays are set at 45 kV p and 10 mA a) shows the image as recorded in nA and b) shows this inverted and with the contrast enhanced to highlight the details of the screw
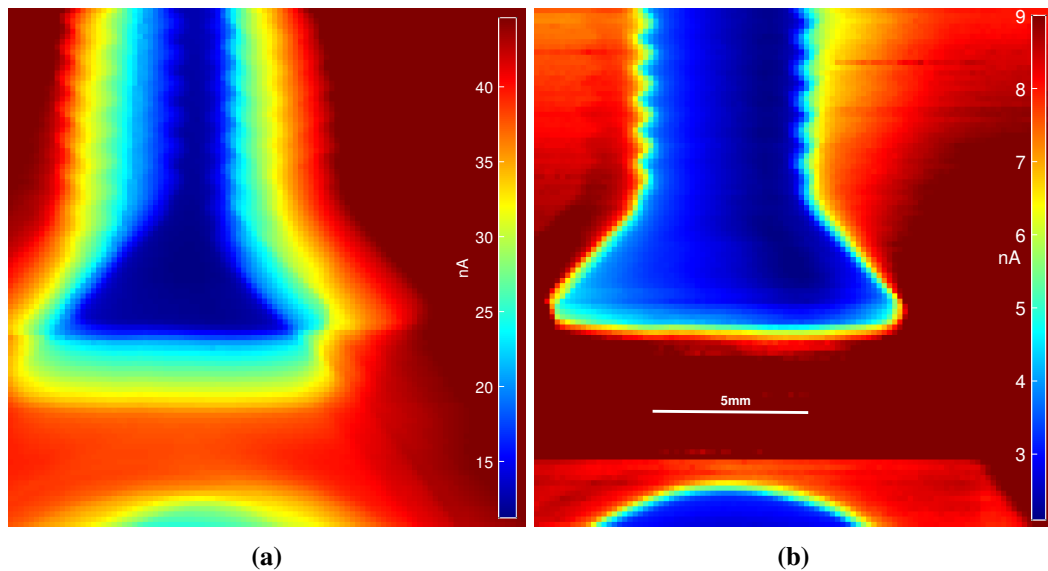
Figure 6.30: Two X-ray images taken of an M5 bolt using the same X-ray energy, 80 kV p and 5 mA, with a resolution of 200 μm pixel pitch. 6.30a is taken without guarding, while 6.30b is taken with guarding

The initial imaging test performed with device 6 and a M4 nylon screw is shown in figure 6.29. Here, there is large degree of blurring, particularly in the horizontal plane due to a lack of guarding on the horizontally neighbouring contacts. This blurring appears to manifest as multiple overlaid shadows on the detective area. In figure 6.29b the image is inverted and contrast enhanced to best resolve the nylon screw, in which it is possible to see the the thread of the screw body.

In figure 6.30 two separate attempts are shown to image a stainless steel M5 bolt with the same device, D9, both at the same resolution and X-ray energy. In figure 6.30a, the pixel in use is completely isolated, and so receives X-ray generated charge from a large portion of the perovskite. This is reflected in the large point spread function of the image and blurring of the bolt, leading to an intense Gaussian blur and the overall shape of the object is lost. In contrast, figure 6.30b is far more clear, where the point spread function is visibly only around a few hundred microns at the edge of the bolt, and details of the thread are resolvable through the centre of the bolt.

Figure 6.31: An X-ray image of nylon nuts joined by a brass screw, with a translation step of $100\,\mu m$, and X-ray energy at $45\,kVp$ and $10\,mA$

Figure 6.31 displays an image of two strongly contrasting objects, of a brass

screw joining two long nylon nuts. There are many distinguishable features of this image, such as the hollow cavity within the larger nylon nut, the gap separating the two nylon nuts, and very faintly a set of two threads meshing together where the brass screw is joined. All of these act as challenging features to resolve and proof of the detective capability of the device.
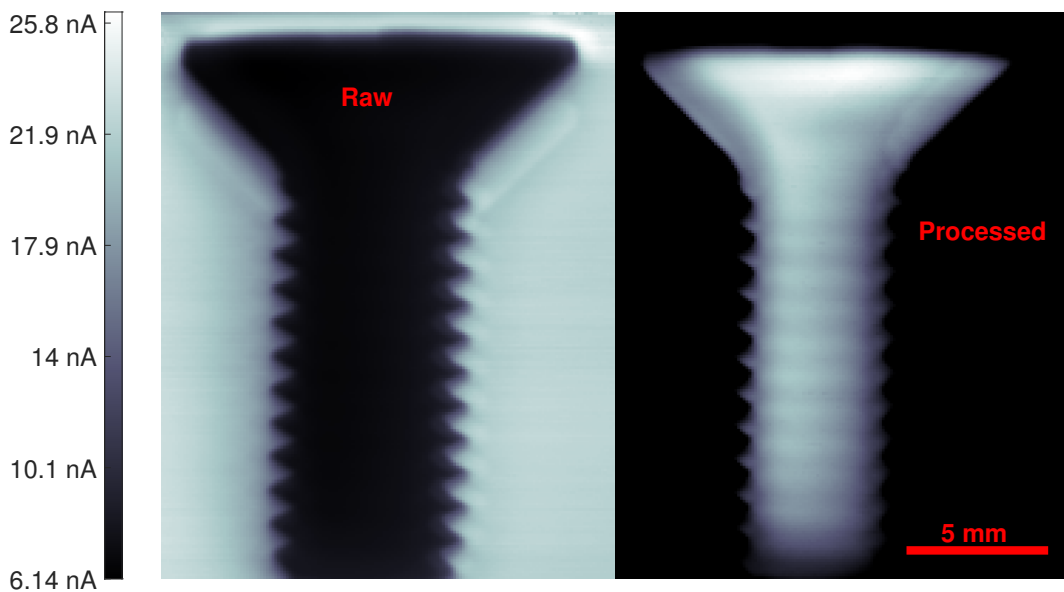
Figure 6.32: A 200x200 X-ray image of an M5 screw taken by Device 5 Pixel 5 which is a 500 μm square contact and translating by 100 μm for each pixel in the image, biased at 5V. The X-ray tube was operating at 80 kVp and 5 mA, acquired through translation in X-ray beam over 3 hours. The left image is raw data, while the right is inverted and with enhanced contrast

In figure 6.32 is shown the clearest image acquired of a sample by the perovskite devices, where the threads are well resolved. The thickness of the steel can also be interpreted from the beam attenuation, where the lightest part of the right image is at the thick head of the bolt.

There is notably a shadowing effect occurring, whereby a shadow edge of the bolt is visible as an overlay inside and outside of its perimeter. This is likely a result of charge bleeding in from around the pixel. In this particular pixel, it was

flanked by guards, but the above and below pixel were not connected, it is possible that surface charge naturally collected at the gold contact surfaces and was able to transport the short distance over to the pixel of interest to be read out.

6.7 Conclusions

In this chapter, the X-ray detection functionality and performance of the devices synthesised in chapter 4 were tested.

A rigorous testing regime was decided where the devices would be exposed to an unfiltered tungsten target X-ray source for $20\,s$ periods, with tube voltage ranging from $20\,kV$ up to $100\,kV$ and current at $10\,mA$, and then holding the tube at $100\,kV$ and ranging the current from $1\,mA$ up to $9\,mA$, within a $900\,s$ run time. This yielded measurements of the response of each device to varying levels of radiation dose rate and understanding how the photoresponse scaled with increasing energy and intensity. Measurements of the dark current were used in conjunction with these values to determine a ratio of dark current to photocurrent, which acted as the most stable value between devices for evaluating the radiation dose rate.

Current-Voltage (I-V) curves were also acquired for pixels on each device to observe the dark current and photocurrent over biases between -10 to $+10\,V$. This allowed inspection of diode like behaviour formed from using contacts of complementary work function (Au and Ag). This diode nature was observed in most pixel connections, with a gradual breakdown voltage being reached at -3 to $-6\,V$.

The general response of each device was highly variable even within samples, which is likely to be affected by the measurement method of a bespoke needle

probe station to contact the pixels with an unreliable level of pressure and control, in some cases scratching away contacts to reduce their effective area. Other cases involved delayed breakdown of the photocurrent such that the device resistance reduced many multiples beyond their natural state. However, devices functioned as expected for the most part and values were able to be extracted.

An experimental form of a channel based charge extraction was tested on one perovskite pellet, where photoelectrons were read out at different contacts depending upon the depth within the perovskite that they had been generated. This was used to infer an approximation of the energy of the photons that generated the photoelectrons. The data here was mostly proof-of-concept, as the device was unoptimised and lacking much of the design ideas introduced in chapter 4.

X-ray images were compiled through vertical and lateral translation of the pixels behind the X-ray beam and various objects. When exposed to a pinhole beam, the spread of photogenerated charge beyond the width of the initial radiation beam was visualised, while connecting to guarding contacts or being entirely isolated. Further to this, images acquired of objects displayed the ability of the perovskite to capture images even with pixel contacts as large as 500 µm.

Discussion and Conclusions

7.1   Discussion of Results

From a broad perspective, the full process of constructing an X-ray detecting device in the form of $CsPbBr_3$ perovskite was performed. Each step required further research to achieve the process efficiently and hence establish a working production and testing method.

Novel aspects of this research are seen in the use of pressed pellet perovskite devices, from $CsPbBr_3$, which utilises a cheap production method to form a functioning direct X-ray detection device. This leads to a scalable production method that can be used to create quick and cheap X-ray detectors, applicable to lower cost healthcare, ease of prototyping detective designs and faster manufacture procedures.

The issue of greatest concern would be the rather low $\mu\tau$-product, resulting most likely from a low mobility in the pressed pellet devices as there is high density of grain boundaries impeding charge flow. This is not unexpected of such device manufacturing methodology, however it severely limits their performance if it is not possible to improve the efficiency. This could be improved through increasing of the pressing pressure to improve inter grain contact or mitigated through thinning

of device channels.

A point can be made about the device stability however, which is frequently a problem arising in the previous research[30, 61, 54]. These devices were only tested after a waiting period of 300 days post growth and pressing. There are unfortunately no tests from when they were first synthesised, however, the devices showing a good response to radiation exposure after that time period makes a statement of either their long term stability or higher initial sensitivity. As either their response would have initially been much higher and then decayed, or that not much decay had occurred in that time period at all, or perhaps a mixture of both.

Improvements can be made however, and the more specific problems with the process also need to be considered and then future work addressed.

In chapter 4, the furnace melt method for single crystal synthesis was attempted in order to create a second set of $CsPbBr_3$ devices made from single crystals that would then serve as useful contrasts against the pressed pellet devices. This would have been particularly useful for highlighting advantages and disadvantages between the two forms of perovskite samples. However, the furnace melting process did not achieve high enough quality to be testable.

One issue to be considered with this, is the vacuum sealing of the ampoules, done through industrial vacuum pumping of the quartz tube before being sealed off by blow torch at around 1700 °C. Firstly, the vacuum quality could not be measured, with the pump nominally reaching a pressure of around 100 Pa. The pump also disturbed the perovskite powder sending some to the end of the tube about to be sealed off. Thus, upon sealing at such a high temperature, some amount of $CsPbBr_3$

was clearly seared onto the inner walls of the ampoule. This could have led to multiple confounding compounds introduced into the powder or atmosphere of the ampoule.

Another problem is likely due to the furnace limitations, as at its slowest cooling rate, the resultant samples still featured many grain boundaries and a low density, indicating that the sample was cooled too quickly. This could be avoided by a much more controlled apparatus, especially able to cool much slower at specifically the melting point of $CsPbBr_3$ (570 °C) to assist crystal formation and the two phase transitions at 110 °C and 80 °C to reduce stress upon the bulk of the crystal. Further to that, making use of the Bridgman growth methodology would also help to avoid imperfect crystal synthesis.

In chapter 6 many results were acquired as best as could be achieved. A compromise was involved with device 8 of the final samples, i.e. the channelled device. The device was designed to have variable length channels that would ideally lead to an even distribution of charge between each contact for a given X-ray energy and also guarding between channels to help simulate an isolated channel of perovskite. However, the contact deposition blurred the edges and hence merged the contacts between one another, so they had to be manually cut away with a scalpel, which reduced channel dimension accuracy and resolution.

One point to note is that the devices tested here were under a much larger dose rate than is usually reported in literature[12, 75], as the X-ray source had a high power output. However, this research has shown that increasing dose rates correlates with diminishing increases in the photocurrent, which in the case of this work,

likely led to decreased sensitivity values over what could have been achieved had the devices been tested at lower dose rates. Indeed, in figure 6.10, device response ratio, R, that is independent of dose and active area, is greatest at the lowest dose rates. This indicates that there is a level of photocurrent saturation from increased dose in perovskite devices and that greater sensitivity is achieved at dose rates in the μGy range, as opposed to the mGy range used here.

The needle test bed was a solution to a temporary problem that would have otherwise left the research with no final results, but it is not an ideal solution. The manual nature of its application led to unknown pressures applied by the needle onto the sample, which created an unknown value of contact resistance and had clear impact upon the photocurrent readout, to the degree that repeatability of results was very much in doubt. Furthermore, the needles application also led to degradation of the contacts during connection and disconnection, reducing the effective area of pixels and leading to further loss of repeatability. This ultimately led to a state where pixels could only be experimented on for a single set of exposures, and reapplication would lead to entirely different values. It could be at least concluded that there being reasonable agreement between measurements was a testament to the devices responses through this unpredictability.

7.2 Future Work

There are many opportunities to further explore the use of $CsPbBr_3$ in X-ray detection, for the purposes of response optimisation and application specific requirements or otherwise.

The pressed pellet $CsPbBr_3$ was the most interesting of the results obtained here, and full analysis of the physical processes involved in this synthesis, as well as the contact deposition and connection are all equally intriguing.

The testable variables that may contribute to vast changes in the performance will be listed here in chronological order from synthesis to readout and discussed:

a. Solution growth controls

b. Pressing process, pressure, temperature and evacuation

c. Production scaling

d. Scanning Electron Microscopy (SEM), Transmission Electron Microscopy (TEM) and X-ray Diffraction (XRD) Analysis

e. Device thickness and pixel dimensions

f. Contact Materials, Charge Blocking/Transport Layers and Hermetic Sealing

g. Time Resolved Response

h. Radiation Hardness

i. Alternative Radiation Sensitivity

7.2.1 Solution Growth Controls

In the literature [51, 52, 55, 59] there are multiple methods for synthesising $CsPbBr_3$ and related compounds. [61] describes optimisation for the mixing molar ratios of the precursor compounds to avoid compounds such as Cs_4PbBr_6 or

$PbBr_2 \cdot 2[(CH_3)_2SO]$ forming. Much of this must be taken into account for future experiments to ensure the highest quality of crystals.

The equipment for growth in chapter 3 could be considered mundane and restrictive given the simplicity of the instrumentation. This could be improved upon with a more dedicated processing set up. For example, DCM evaporate could be pumped into the growth atmosphere from outside, thereby allowing control over the growth rate through the atmospheric density of DCM. This could also be optimised through growth in vacuum or nitrous atmosphere to ensure a lack of water vapour in the air and prevent dissolving crystallites.

7.2.2 Pressing pressure, temperature and evacuation

The crystallites, prior to pressing, were ground with mortar and pestle, which is a rather uncontrolled and sporadic method of processing, generating unknown grain sizes in the resulting fragments. A suggested control for these grain sizes would be to follow the grinding with filtration through sieves of a variety of sizes to separate the grains by their upper and lower size limits. Pressing perovskites together grouped by their grain size would increase the homogeneity of the pellets and so improve the packing density and interconnectivity.

One of the major considerations to analyse would be the methodology involved in the pressing technique. In the methods discussed in chapter 3, the pressing method remained the same throughout, using the same materials and values.

Changing the pressure employed upon the perovskite to explore the changes in material characteristics would greatly help to understand how this mechanism works

to create a functioning active channel and also ideally find a maximum viable pressure level. The pressure utilised here was limited by the tolerance of the pressing dye. Hypothetically, the greater the pressure, the greater the packing density and internal contact within the crystallite will be, which would increase performance twofold, through higher X-ray attenuation and greater carrier mobility.

One consideration however, is that, since the surface of the material has such interesting transport properties, along with an incomplete packing density, essentially leads to internal surfaces. Perhaps, better packing might decrease the response through changing the material structure by reducing the density of internal surfaces.

Employing temperature control during compression would also be useful as the lattice structure of $CsPbBr_3$ is known to go through two phase transitions at 87 °C and 121 °C, which causes internal stress and forms cracks and discontinuities in the material. Using cryogenic temperatures for this or a slower pressing differential would likely avoid high temperature fluctuations during the process to discourage these transitions.

Improvement in the materials used for pressing, would avoid surface malformations and improve smoothness. For example, the steel sandwiching plates could have been repolished after each pressing to remove contaminants and etches gained from the pressing, along with also hardening to reduce malformation under the pressure. This improvement in smoothness overall should also increase the quality of the contacts laid down. In this methodology, contacts were of the order of 100 nm thick, so disturbances and cracks in the surface of the perovskite pellet of that very small magnitude would disturb connectivity and thus performance of the contacts.

In order to test for this, surface roughness tests would give an insight into the level of disturbance that would be encountered and the performance of the pressing method for flattening the pellet.

Finally, connecting active vacuum pumping to the pressing vessel would help to remove impurities by reducing the presence of trapped gasses within fissures, further increasing the pressing efficiency and internal continuity. This would also help to remove loose perovskite fragments and improve temperature control as compressed gas pockets can increase localised temperature fluctuations more so than the crystallites.

7.2.3 Production Scaling

In order to prepare these devices for a greater mass production, larger growth batch synthesis must also be tested and optimised. This could be either through many small growths at a large scale, or large singular containers. The former suffers from an increased workload to the process, whereas the latter is vulnerable to deficiencies in batches spoiling all of the solution and growth process. Optimal production methods would start from the former and move towards the latter as reliability increases, while further improvements could be made from dedicated synthesis containers and employing strict repeatable techniques.

7.2.4 SEM, TEM and X-ray Fluorescence (XRF) Analysis

Following on from altering the pressing pressure and materials along with the grain sizing, electron microscopy could offer great opportunities to study the direct effects of these changes. This would form a useful feedback loop for informing the

best mechanisms to use for processing and pressing.

TEM would be ideal for analysing grain sizes after pressing and the general changes that occur with variation in the production methods. This also can further inform what characteristics affect the device performance.

XRF is a useful analysis tool for observing the exact chemical composition of compounds upon the surface of and within the perovskite, to better understand how well the growth technique is synthesising a purified sample, and look for contaminants that may be detrimental to operation. This can also show the homogeneity of the material and understand any local clusters of contaminants.

7.2.5   Device and Channel Thickness

The thickness of the active channel of $CsPbBr_3$ is fundamental to it's operation as a direct X-ray detector. Here, the optimal thickness was considered to be ˜1 mm as this led to the absorption of the majority of X-ray photons in the 1–100 keV range. However, this sacrificed charge collection efficiency as the charges had a high chance for reabsorption before they were collected at the electrodes. This high attenuation efficiency was thus counteracted by the lack of charge collection, and so further research should aim to balance these two factors such that they are equally optimised.

Varying the device thickness over a logarithmic range (e.g. 10 μm, 30 μm, 100 μm, 300 μm) is a suitable start for determining a sweet spot for device thickness to increase the charge collection efficiency while not sacrificing many of the X-ray generated charge carriers.

7.2.6   Contact Materials and Charge Blocking/Transport Layers

One frequently reported issue with contact materials used to functionalise many perovskite devices is reaction and degradation between the contact materials and the active channel. Silver contacts [76] have shown various levels of instability with $MAPbBr_3/I_3$, with the structure spreading outwards across the surface and downwards into the perovskite, in turn changing the properties of the surrounding material and decreasing the readout efficiency. Similar behaviour was observed visually in the $CsPbBr_3$ in this work. Some researchers [77] have found gold contacts form various compounds with $CsPbBr_3$ at the surface that leads to similar changes as with the silver. Both of these effects appear exacerbated by increasing bias voltage placed upon the contact.

An asset in resolving this issue while also improving the overall functionality would be to include charge blocking and transport layers, that specifically allow through either holes or electrons to the readout contact while resisting the other. This would decrease the dark current by blocking some of the charge carriers generated near the readout interface and also increase the response by controlling the direction of flow of charge carriers. These are synthesised from a p-type or n-type compound and deposited in a thin layer of a few tens of nm before contacts are deposited and so would act as a buffer layer to block reactions taking place between contact materials and the perovskite. Of course, this may only shift the problem to reactions from these control layers with the perovskite, however, there is much current research in determining non-reactive, conductive compounds to use for this

purpose.

Another issue that faces much of current perovskite research is the general reaction to air. Although no strong ambient air based degradation was observed within this study, it has been reported for much of the related compounds. It is also known that water and similar polar molecules react with $CsPbBr_3$ to break down the perovskite structure, which could contact the material in gaseous form from the surrounding atmosphere. To combat this effect, a hermetic sealing layer atop the completed perovskite device could be used, which would ideally be thin, as not to interrupt X-ray sensitivity, non-reactive with the perovskite or other added compounds, electrically insulating, and optically opaque to also reduce visual light noise.

7.2.7   Temporally Resolved Response Time

In the course of this project it was not possible to generate meaningful sources of data for the response times for the devices, thus the $\mu\tau$-product could only be estimated from use of the Hecht equation[70] using charge collection efficiency. Further research, using devices with known thicknesses of the active channel and well understood contact dimensions would be very beneficial to understanding the actual nature of the charge carriers within these pressed pellets. Time resolved measurements can be used to directly measure the mobility of the sample through the rise time and fall time of a signal when exposed to a known X-ray beam. Combining this with both a variation in the kVp of the X-ray tube and also mono energetic X-ray sources such as ^{241}Am and ^{99m}Tc, can together help to determine an estimate of

the time to absorb photo-electrons/holes based on penetration within the material.

7.2.8 Radiation Hardness

The results obtained in this work did not resolve over a long time period for many samples and as such the long term effects of radiation on the perovskite samples and electrical contacts were not able to be observed. Future work would be required to determine if there are such effects and the extent of modification it may cause in a $CsPbBr_3$ direct detector. Some short term effects could include localised trap states formed by high energy radiation that inhibit charge carrier flow but over time reform back towards the original structure, while long term effects are more likely lattice site modifications from radiation induced dislocations of atoms. Short term and long term effects must be tested for and quantified in order for a reliable X-ray detector to be built, to assist in protection or mitigation against these effects or to otherwise predict system degradation.

7.2.9 Alternative Radiation Sensitivity

The use of $CsPbBr_3$ as a direct radiation detector is purely through the generation of charge carriers becoming elevated in energy from the valence to conduction band of the semiconductor. This imparting of energy can be achieved by other processes than gamma photons, such as alpha particles, beta particles, high energy protons and even potentially neutrons. If their effect is known and understood, and steps are taken to optimise the device design, this material could also serve as a detector for these radioactive particles.

Neutron imaging is an example of a field that is gaining popularity with recent

advances[78], as neutrons much more reliably pass through heavy metals than X-rays, but are attenuated by atoms such as hydrogen and lithium, which allows them to show contrast in an entirely new set of parameters. Functionalising perovskites for neutron detection would involve mixing in nuclei with high neutron interaction cross-sections, such as Boron-10 or Lithium-6, with the main components, whereby the neutron interactions with these elements through neutron capture would generate ionising particles that then energise the free electrons required for detection.

7.3   Research Output and Conclusions

What has broadly been achieved is the realisation of $CsPbBr_3$ as an X-ray detecting device. The functionality of powdered pressed pellet $CsPbBr_3$ has been demonstrated, where no significant change in the material bandgap has eventuated from the processing methods. Additionally, device responses were all measured after 300 days of air exposure, and such performance is very useful for applications.

The novel application of pressed powder perovskite to X-ray detection has been achieved, and the advantages and disadvantages discussed. This project lays the groundwork for the exploitation of the unique properties of $CsPbBr_3$ for X-ray detection and imaging, upon which much can be built, which has also been discussed.

The channelled devices were a novel design and were shown to function as intended through a proof of concept test, and that further work can be carried out to explore their use and application. An ideal next step would be to use the channelled device for an x-y translation based image acquisition to observe the differing levels

of contrast in context, using a sample with large variations in radiation attenuating properties.

The simulations in tandem with experimental dose measurement highlighted the difficulty in accurately predicting a bremsstrahlung X-ray spectrum and how small deviations of a model from reality lead to large uncertainties when evaluating electronic devices with this model. Care can be taken to improve this through rigorously standardised methodology and good understanding of the X-ray generation mechanisms, to truly find a direct relation between simulation and the real environment.

Single crystals were attempted to be synthesised through vacuum sealing and slow cooling, however, contaminants along with a fast cooling rate, were considered to be the cause of bad structural integrity and a large concentration of grain boundaries. This lead to unsuitable samples for X-ray sensitivity tests, which could be improved upon in future work.

$\mu\tau$-products were found to be low for pressed pellet devices, which is explained by the multi-granular structure that hinders free flow of charge throughout the bulk of the material. As a result, it is expected that only charge near the surface contacts is expected to contribute to the photocurrent. Here, the level of X-ray penetration is minimal, so the majority of the charge carriers collected here are expected to originate from low energy X-rays, except in the case of full penetration through the perovskite material, where charge carriers can be read out when generated near the back contact also.

Key advantages to this device synthesis include the ease and low cost of pro-

duction, scalability and tailored pellet dimensions for bespoke operation purposes. There is potential for high stability under ambient conditions, though this was not thoroughly tested enough to conclude on. Disadvantages include low charge mobility, leading to a low efficiency for charge collection from deposited radiation, and instability at higher voltages from contact degradation. Further research is required on achieving higher pressing pressure, making use of charge transport layers and decreasing contaminants in production, all in the interest of increasing the charge mobility.

Bibliography

[1] Wilhelm Röntgen. Ueber eine neue Art von Strahlen. *Würzburg : Verlag der Stahel'schen k. Hof- u. Universitäts -Buch- u. Kunsthandlung*, Vorläufige Mitteilung:137–147, 1895.

[2] B.G. Lowe. *Semiconductor X-Ray Detectors / B.G. Lowe, R.A. Sareen.* Sensors Series. CRC Press, Taylor & Francis Group, Boca Raton, 2014.

[3] T. Takahashi and S. Watanabe. Recent progress in CdTe and CdZnTe detectors. *IEEE Transactions on Nuclear Science*, 48(4):950–959, August 2001.

[4] Christopher C. Scott, Shiva Abbaszadeh, Sina Ghanbarzadeh, Gary Allan, Michael Farrier, Ian A. Cunningham, and Karim S. Karim. Amorphous selenium direct detection CMOS digital x-ray imager with 25 micron pixel pitch. In *Medical Imaging 2014: Physics of Medical Imaging*, volume 9033, page 90331G. International Society for Optics and Photonics, March 2014.

[5] Gustav Rose. Perowskit. *Ann. Phys*, 48:558, January 1839.

[6] Chr Kn Møller. Crystal Structure and Photoconductivity of Cæsium Plumbohalides. *Nature*, 182(4647):1436–1436, November 1958.

[7] Hans-Rudolf Wenk and Andrei Bulakh. *Minerals: Their Constitution and Origin*. Cambridge University Press, April 2004.

[8] Takamitsu Yamanaka, Noriyuki Hirai, and Yutaka Komatsu. Structure change of Ca1–xSrxTiO3 perovskite with composition and pressure. *American Mineralogist*, 87(8-9):1183–1189, August 2002.

[9] Kristin Persson. Materials Data on CsPbBr3 (SG:62) by Materials Project, 2014.

[10] J. A. Bearden. X-Ray Wavelengths. *Reviews of Modern Physics*, 39(1):78–124, January 1967.

[11] Jun Kang and Lin-Wang Wang. High Defect Tolerance in Lead Halide Perovskite CsPbBr $_3$. *The Journal of Physical Chemistry Letters*, 8(2):489–493, January 2017.

[12] Sergii Yakunin, Mykhailo Sytnyk, Dominik Kriegner, Shreetu Shrestha, Moses Richter, Gebhard J. Matt, Hamed Azimi, Christoph J. Brabec, Julian Stangl, Maksym V. Kovalenko, and Wolfgang Heiss. Detection of X-ray photons by solution-processed lead halide perovskites. *Nature Photonics*, 9(7):444–449, July 2015.

[13] Parthiban Ramasamy, Da-Hye Lim, Bumjin Kim, Seung-Ho Lee, Min-Sang Lee, and Jong-Soo Lee. All-inorganic cesium lead halide perovskite nanocrystals for photodetector applications. *Chemical Communications*, 52(10):2067–2070, 2016.

[14] Adam H. Slavney, Te Hu, Aaron M. Lindenberg, and Hemamala I. Karunadasa. A Bismuth-Halide Double Perovskite with Long Carrier Recombination Lifetime for Photovoltaic Applications. *Journal of the American Chemical Society*, 138(7):2138–2141, February 2016.

[15] Qidong Tai, Kai-Chi Tang, and Feng Yan. Recent progress of inorganic perovskite solar cells. *Energy & Environmental Science*, 12(8):2375–2405, August 2019.

[16] Sergii Yakunin, Dmitry N. Dirin, Yevhen Shynkarenko, Viktoriia Morad, Ihor Cherniukh, Olga Nazarenko, Dominik Kreil, Thomas Nauser, and Maksym V. Kovalenko. Detection of gamma photons using solution-grown single crystals of hybrid lead halide perovskites. *Nature Photonics*, 10(9):585–589, September 2016.

[17] Shreetu Shrestha, René Fischer, Gebhard J. Matt, Patrick Feldner, Thilo Michel, Andres Osvet, Ievgen Levchuk, Benoit Merle, Saeedeh Golkar, Haiwei Chen, Sandro F. Tedde, Oliver Schmidt, Rainer Hock, Manfred Rührig, Mathias Göken, Wolfgang Heiss, Gisela Anton, and Christoph J. Brabec. High-performance direct conversion X-ray detectors based on sintered hybrid lead triiodide perovskite wafers. *Nature Photonics*, 11(7):436–440, July 2017.

[18] Yihui He, Weijun Ke, Grant C. B. Alexander, Kyle M. McCall, Daniel G. Chica, Zhifu Liu, Ido Hadar, Constantinos C. Stoumpos, Bruce W. Wessels, and Mercouri G. Kanatzidis. Resolving the Energy of γ-Ray Photons with MAPbI3 Single Crystals. *ACS Photonics*, 5(10):4132–4138, October 2018.

[19] Haotong Wei and Jinsong Huang. Halide lead perovskites for ionizing radiation detection. *Nature Communications*, 10, March 2019.

[20] Yong Churl Kim, Kwang Hee Kim, Dae-Yong Son, Dong-Nyuk Jeong, Ja-Young Seo, Yeong Suk Choi, In Taek Han, Sang Yoon Lee, and Nam-Gyu Park. Printable organometallic perovskite enables large-area, low-dose X-ray imaging. *Nature*, 550(7674):87–91, October 2017.

[21] M. D. Birowosuto, D. Cortecchia, W. Drozdowski, K. Brylew, W. Lachmanski, A. Bruno, and C. Soci. X-ray Scintillation in Lead Halide Perovskite Crystals. *Scientific Reports*, 6:srep37254, November 2016.

[22] Yu Han, Steffen Meyer, Yasmina Dkhissi, Karl Weber, Jennifer M. Pringle, Udo Bach, Leone Spiccia, and Yi-Bing Cheng. Degradation observations of encapsulated planar CH3NH3PbI3 perovskite solar cells at high temperatures and humidity. *Journal of Materials Chemistry A*, 3(15):8139–8147, March 2015.

[23] Rui Wang, Muhammad Mujahid, Yu Duan, Zhao-Kui Wang, Jingjing Xue, and Yang Yang. A Review of Perovskites Solar Cell Stability. *Advanced Functional Materials*, 0(0):1808843, January 2019.

[24] G. Grancini, C. Roldán-Carmona, I. Zimmermann, E. Mosconi, X. Lee, D. Martineau, S. Narbey, F. Oswald, F. De Angelis, M. Graetzel, and Mohammad Khaja Nazeeruddin. One-Year stable perovskite solar cells by 2D/3D interface engineering. *Nature Communications*, 8:15684, June 2017.

[25] Zubair Ahmad, Fakhra Aziz, and Hewa Yaseen Abdullah. Study on the stability of the mixed (MAPbI3 and MAPbBr3) perovskite solar cells using dopant-free HTL. *Organic Electronics*, 76:105453, January 2020.

[26] Lucie McGovern, Moritz H. Futscher, Loreta A. Muscarella, and Bruno Ehrler. Understanding the Stability of MAPbBr3 versus MAPbI3: Suppression of Methylammonium Migration and Reduction of Halide Migration. *The Journal of Physical Chemistry Letters*, 11(17):7127–7132, September 2020.

[27] Gerardo Gordillo, Oscar G. Torres, Maria Camila Abella, Julian C. Peña, and Ophyr Virguez. Improving the stability of MAPbI3 films by using a new synthesis route. *Journal of Materials Research and Technology*, 9(6):13759–13769, November 2020.

[28] Loredana Protesescu, Sergii Yakunin, Maryna I. Bodnarchuk, Franziska Krieg, Riccarda Caputo, Christopher H. Hendon, Ruo Xi Yang, Aron Walsh, and Maksym V. Kovalenko. Nanocrystals of Cesium Lead Halide Perovskites (CsPbX3, X = Cl, Br, and I): Novel Optoelectronic Materials Showing Bright Emission with Wide Color Gamut. *Nano Letters*, 15(6):3692–3696, June 2015.

[29] Michael Kulbak, David Cahen, and Gary Hodes. How Important Is the Organic Part of Lead Halide Perovskite Photovoltaic Cells? Efficient CsPbBr3 Cells. *The Journal of Physical Chemistry Letters*, 6(13):2452–2456, July 2015.

[30] Michael Kulbak, Satyajit Gupta, Nir Kedem, Igal Levine, Tatyana Bendikov, Gary Hodes, and David Cahen. Cesium Enhances Long-Term Stability of Lead Bromide Perovskite-Based Solar Cells. *The Journal of Physical Chemistry Letters*, 7(1):167–172, January 2016.

[31] Byungkyun Kang and Koushik Biswas. Exploring Polaronic, Excitonic Structures and Luminescence in Cs4PbBr6/CsPbBr3. *The Journal of Physical Chemistry Letters*, 9(4):830–836, February 2018.

[32] Yihui He, Zhifu Liu, Kyle M. McCall, Wenwen Lin, Duck Young Chung, Bruce W. Wessels, and Mercouri G. Kanatzidis. Perovskite CsPbBr3 single crystal detector for alpha-particle spectroscopy. *Nuclear Instruments and Methods in Physics Research Section A: Accelerators, Spectrometers, Detectors and Associated Equipment*, 922:217–221, April 2019.

[33] D. W. Rogers, B. A. Faddegon, G. X. Ding, C. M. Ma, J. We, and T. R. Mackie. BEAM: A Monte Carlo code to simulate radiotherapy treatment units. *Medical Physics*, 22(5):503–524, May 1995.

[34] Michael K. Fix, Harald Keller, Peter Rüegsegger, and Ernst J. Born. Simple beam models for Monte Carlo photon beam dose calculations in radiotherapy. *Medical Physics*, 27(12):2739–2747, December 2000.

[35] G. Barca, F. Castrovillari, S. Chauvie, D. Cuce, F. Foppiano, G. Ghiso, S. Guatelli, E. Lamanna, M. C. Lopes, L. Peralta, M. G. Pia, P. Rodrigues, A. Trindade, and M. Veltri. A powerful simulation tool for medical physics ap-

plications: Geant4. *Nuclear Physics B - Proceedings Supplements*, 125:80–84, September 2003.

[36] David J. Eaton, Graham Bass, Paul Booker, John Byrne, Simon Duane, John Frame, Mark Grattan, Russell AS Thomas, Natalie Thorp, and Andrew Nisbet. IPEM code of practice for high-energy photon therapy dosimetry based on the NPL absorbed dose calibration service. *Physics in Medicine & Biology*, 65(19):195006, September 2020.

[37] Robin Hill, Brendan Healy, Lois Holloway, Zdenka Kuncic, David Thwaites, and Clive Baldock. Advances in kilovoltage x-ray beam dosimetry. *Physics in Medicine and Biology*, 59(6):R183–R231, February 2014.

[38] A. F McKinlay and England) Hospital Physicists' Association (London. *Thermoluminescence Dosimetry*. Bristol : Hilger in collaboration with the Hospital Physicists' Association, 1981.

[39] A. S. Pradhan. Thermoluminescence Dosimetry and its Applications. *Radiation Protection Dosimetry*, 1(3):153–167, January 1981.

[40] G. Poludniowski, G. Landry, F. DeBlois, P. M. Evans, and F. Verhaegen. SpekCalc : A program to calculate photon spectra from tungsten anode x-ray tubes. *Physics in Medicine and Biology*, 54(19):N433, 2009.

[41] Andrew M. Hernandez and John M. Boone. Tungsten anode spectral model using interpolating cubic splines: Unfiltered x-ray spectra from 20 kV to 640 kV. *Medical Physics*, 41(4):042101, April 2014.

[42] S. Agostinelli, J. Allison, K. Amako, J. Apostolakis, H. Araujo, P. Arce, M. Asai, D. Axen, S. Banerjee, and G. Barrand et al. Geant4—a simulation toolkit. *Nuclear Instruments and Methods in Physics Research Section A: Accelerators, Spectrometers, Detectors and Associated Equipment*, 506(3):250–303, July 2003.

[43] Metrix. X-ray Generators — X-Ray Generators. https://metrixndt.com/generators/, 2014.

[44] R. H. Redus, J. A. Pantazis, T. J. Pantazis, A. C. Huber, and B. J. Cross. Characterization of CdTe Detectors for Quantitative X-ray Spectroscopy. *IEEE Transactions on Nuclear Science*, 56(4):2524–2532, August 2009.

[45] Saint-Gobain. CDF Radiation Monitoring. http://cdf-radmon.fnal.gov/dosimetry/, August 2002.

[46] FLUKE BIOMEDICAL. 10100AT TRIAD TnT Field Service Kit - Operators Manual, February 2005.

[47] A. Mohammadi, M. Baba, H. Ohuchi, Y. Kaga, and F. Yamada. On the Use of a Thick Carbon Target in the 90° Compton Spectroscopy for the Measurement of Diagnostic X-rays. *Journal of Nuclear Science and Technology*, 45(sup5):333–336, June 2008.

[48] A. Miceli, R. Thierry, M. Bettuzzi, A. Flisch, J. Hofmann, U. Sennhauser, and F. Casali. Comparison of simulated and measured spectra of an industrial 450 kV X-ray tube. *Nuclear Instruments and Methods in Physics Research*

Section A: Accelerators, Spectrometers, Detectors and Associated Equipment, 580(1):123–126, September 2007.

[49] M. Moralles, C. C. Guimarães, and E. Okuno. Response of thermoluminescent dosimeters to photons simulated with the Monte Carlo method. *Nuclear Instruments and Methods in Physics Research Section A: Accelerators, Spectrometers, Detectors and Associated Equipment*, 545(1–2):261–268, June 2005.

[50] Ernesto Mainegra-Hing and Iwan Kawrakow. Efficient x-ray tube simulations. *Medical Physics*, 33(8):2683–2690, August 2006.

[51] Sandeep Arya, Prerna Mahajan, Ramashanker Gupta, Ritu Srivastava, Naveen kumar Tailor, Soumitra Satapathi, R. Radhakrishnan Sumathi, Ram Datt, and Vinay Gupta. A comprehensive review on synthesis and applications of single crystal perovskite halides. *Progress in Solid State Chemistry*, 60:100286, December 2020.

[52] Constantinos C. Stoumpos, Christos D. Malliakas, John A. Peters, Zhifu Liu, Maria Sebastian, Jino Im, Thomas C. Chasapis, Arief C. Wibowo, Duck Young Chung, Arthur J. Freeman, Bruce W. Wessels, and Mercouri G. Kanatzidis. Crystal Growth of the Perovskite Semiconductor $CsPbBr_3$: A New Material for High-Energy Radiation Detection. *Crystal Growth & Design*, 13(7):2722–2727, July 2013.

[53] Yihui He, Liviu Matei, Hee Joon Jung, Kyle M. McCall, Michelle Chen,

Constantinos C. Stoumpos, Zhifu Liu, John A. Peters, Duck Young Chung, Bruce W. Wessels, Michael R. Wasielewski, Vinayak P. Dravid, Arnold Burger, and Mercouri G. Kanatzidis. High spectral resolution of gamma-rays at room temperature by perovskite CsPbBr 3 single crystals. *Nature Communications*, 9(1):1609, April 2018.

[54] Peng Zhang, Guodong Zhang, Lin Liu, Dianxing Ju, Longzhen Zhang, Kui Cheng, and Xutang Tao. Anisotropic Optoelectronic Properties of Melt-Grown Bulk CsPbBr3 Single Crystal. *The Journal of Physical Chemistry Letters*, 9(17):5040–5046, September 2018.

[55] Dmitry N. Dirin, Ihor Cherniukh, Sergii Yakunin, Yevhen Shynkarenko, and Maksym V. Kovalenko. Solution-Grown CsPbBr3 Perovskite Single Crystals for Photon Detection. *Chemistry of Materials*, 28(23):8470–8474, December 2016.

[56] Qifeng Han, Sang-Hoon Bae, Pengyu Sun, Yao-Tsung Hsieh, Yang (Michael) Yang, You Seung Rim, Hongxiang Zhao, Qi Chen, Wangzhou Shi, Gang Li, and Yang Yang. Single Crystal Formamidinium Lead Iodide (FAPbI3): Insight into the Structural, Optical, and Electrical Properties. *Advanced Materials*, 28(11):2253–2258, 2016.

[57] Makhsud I. Saidaminov, Md Azimul Haque, Jawaher Almutlaq, Smritakshi Sarmah, Xiao-He Miao, Raihana Begum, Ayan A. Zhumekenov, Ibrahim Dursun, Namchul Cho, Banavoth Murali, Omar F. Mohammed, Tom Wu, and Osman M. Bakr. Inorganic Lead Halide Perovskite Single Crystals: Phase-

Selective Low-Temperature Growth, Carrier Transport Properties, and Self-Powered Photodetection. *Advanced Optical Materials*, 5(2):1600704, 2017.

[58] Yevgeny Rakita, Nir Kedem, Satyajit Gupta, Aditya Sadhanala, Vyacheslav Kalchenko, Marcus L. Böhm, Michael Kulbak, Richard H. Friend, David Cahen, and Gary Hodes. Low-Temperature Solution-Grown CsPbBr3 Single Crystals and Their Characterization. *Crystal Growth & Design*, 16(10):5717–5725, October 2016.

[59] Dong Shi, Valerio Adinolfi, Riccardo Comin, Mingjian Yuan, Erkki Alarousu, Andrei Buin, Yin Chen, Sjoerd Hoogland, Alexander Rothenberger, Khabiboulakh Katsiev, Yaroslav Losovyj, Xin Zhang, Peter A. Dowben, Omar F. Mohammed, Edward H. Sargent, and Osman M. Bakr. Low trap-state density and long carrier diffusion in organolead trihalide perovskite single crystals. *Science*, 347(6221):519–522, January 2015.

[60] Xiaoliang Miao, Ting Qiu, Shufang Zhang, He Ma, Yanqiang Hu, Fan Bai, and Zhuangchun Wu. Air-stable CsPb 1-x Bi x Br 3 ($0 \leq x \ll 1$) perovskite crystals: Optoelectronic and photostriction properties. *Journal of Materials Chemistry C*, 5(20):4931–4939, 2017.

[61] Hongjian Zhang, Xin Liu, Jiangpeng Dong, Hui Yu, Ce Zhou, Binbin Zhang, Yadong Xu, and Wanqi Jie. Centimeter-Sized Inorganic Lead Halide Perovskite CsPbBr3 Crystals Grown by an Improved Solution Method. *Crystal Growth & Design*, 17(12):6426–6431, December 2017.

[62] Anthony D. Baranyi, Mario Onyszchuk, Yvon Le Page, and Gabrielle Donnay. The crystal and molecular structure of lead(II)bromide-bis-dimethylsulphoxide, PbBr2•2[(CH3)2SO]. *Canadian Journal of Chemistry*, 55(5):849–855, March 1977.

[63] Yihui He, Oleg Y. Kontsevoi, Constantinos C. Stoumpos, Giancarlo G. Trimarchi, Saiful M. Islam, Zhifu Liu, Svetlana S. Kostina, Sanjib Das, Joon-Il Kim, Wenwen Lin, Bruce W. Wessels, and Mercouri G. Kanatzidis. Defect Antiperovskite Compounds Hg3Q2I2 (Q = S, Se, and Te) for Room-Temperature Hard Radiation Detection. *Journal of the American Chemical Society*, 139(23):7939–7951, June 2017.

[64] Eric W. Weisstein. Gaussian Function. https://mathworld.wolfram.com/GaussianFunction.html, 2016.

[65] Olga A. Lozhkina, Anna A. Murashkina, Vladimir V. Shilovskikh, Yury V. Kapitonov, Vladimir K. Ryabchuk, Alexei V. Emeline, and Tsutomu Miyasaka. Invalidity of Band-Gap Engineering Concept for Bi $^{3+}$ Heterovalent Doping in CsPbBr $_3$ Halide Perovskite. *The Journal of Physical Chemistry Letters*, 9(18):5408–5411, September 2018.

[66] Iman Moeini, Mohammad Ahmadpour, Amir Mosavi, Naif Alharbi, and Nima E. Gorji. Modeling the time-dependent characteristics of perovskite solar cells. *Solar Energy*, 170:969–973, August 2018.

[67] W. M. H. Sachtler, G. J. H. Dorgelo, and A. A. Holscher. The work function of gold. *Surface Science*, 5(2):221–229, October 1966.

[68] A. W. Dweydari and C. H. B. Mee. Work function measurements on (100) and (110) surfaces of silver. *physica status solidi (a)*, 27(1):223–230, 1975.

[69] Youngho Kang and Seungwu Han. Intrinsic Carrier Mobility of Cesium Lead Halide Perovskites. *Physical Review Applied*, 10(4):044013, October 2018.

[70] Karl Hecht. Zum Mechanismus des lichtelektrischen Primärstromes in isolierenden Kristallen. *Zeitschrift für Physik*, 77(3):235–245, March 1932.

[71] A. E. Bolotnikov, G. S. Camarda, E. Chen, R. Gul, V. Dedic, G. De Geronimo, J. Fried, A. Hossain, J. M. MacKenzie, L. Ocampo, P. Sellin, S. Taherion, E. Vernon, G. Yang, U. El-Hanany, and R. B. James. Use of the drift-time method to measure the electron lifetime in long-drift-length CdZnTe detectors. *Journal of Applied Physics*, 120(10):104507, September 2016.

[72] Lodovico. Digital Radiography DIY, February 2018.

[73] Amlan Datta, Piotr Becla, and Shariar Motakef. Visualization of TlBr ionic transport mechanism by the Accelerated Device Degradation technique. *Nuclear Instruments and Methods in Physics Research Section A: Accelerators, Spectrometers, Detectors and Associated Equipment*, 784:37–43, June 2015.

[74] Haotong Wei, Yanjun Fang, Padhraic Mulligan, William Chuirazzi, Hong-Hua Fang, Congcong Wang, Benjamin R. Ecker, Yongli Gao, Maria Antonietta Loi, Lei Cao, and Jinsong Huang. Sensitive X-ray detectors made of

methylammonium lead tribromide perovskite single crystals. *Nature Photonics*, 10(5):333–339, May 2016.

[75] X. Geng, Q. Feng, R. Zhao, T. Hirtz, G. Dun, Z. Yan, J. Ren, H. Zhang, R. Liang, H. Tian, D. Xie, Y. Yang, and T. Ren. High-Quality Single Crystal Perovskite for Highly Sensitive X-Ray Detector. *IEEE Electron Device Letters*, 41(2):256–259, February 2020.

[76] Jiangwei Li, Qingshun Dong, Nan Li, and Liduo Wang. Direct Evidence of Ion Diffusion for the Silver-Electrode-Induced Thermal Degradation of Inverted Perovskite Solar Cells. *Advanced Energy Materials*, 7(14):1602922, 2017.

[77] G. Divitini, S. Cacovich, F. Matteocci, L. Cinà, A. Di Carlo, and C. Ducati. In situ observation of heat-induced degradation of perovskite solar cells. *Nature Energy*, 1(2):1–6, January 2016.

[78] Nikolay Kardjilov, Ingo Manke, Robin Woracek, André Hilger, and John Banhart. Advances in neutron imaging. *Materials Today*, 21(6):652–672, July 2018.

Appendix

Included here in the appendix are figures that are not necessary to the argument of the thesis but included for reference.

Figure 8.1, 8.2 and 8.3 show the design specification of the evaporation mask used for initial perovskite devices. This was before a more efficient and readily disposable mask design was created that superseded this design. It is included for reference on recreating this pixel architecture.

Figure 8.4 shows the same data as in figure 6.22, in chapter 6, but on a logarithmic scale to help highlight the distinction between photocurrent observed under vastly differing levels of filtration.
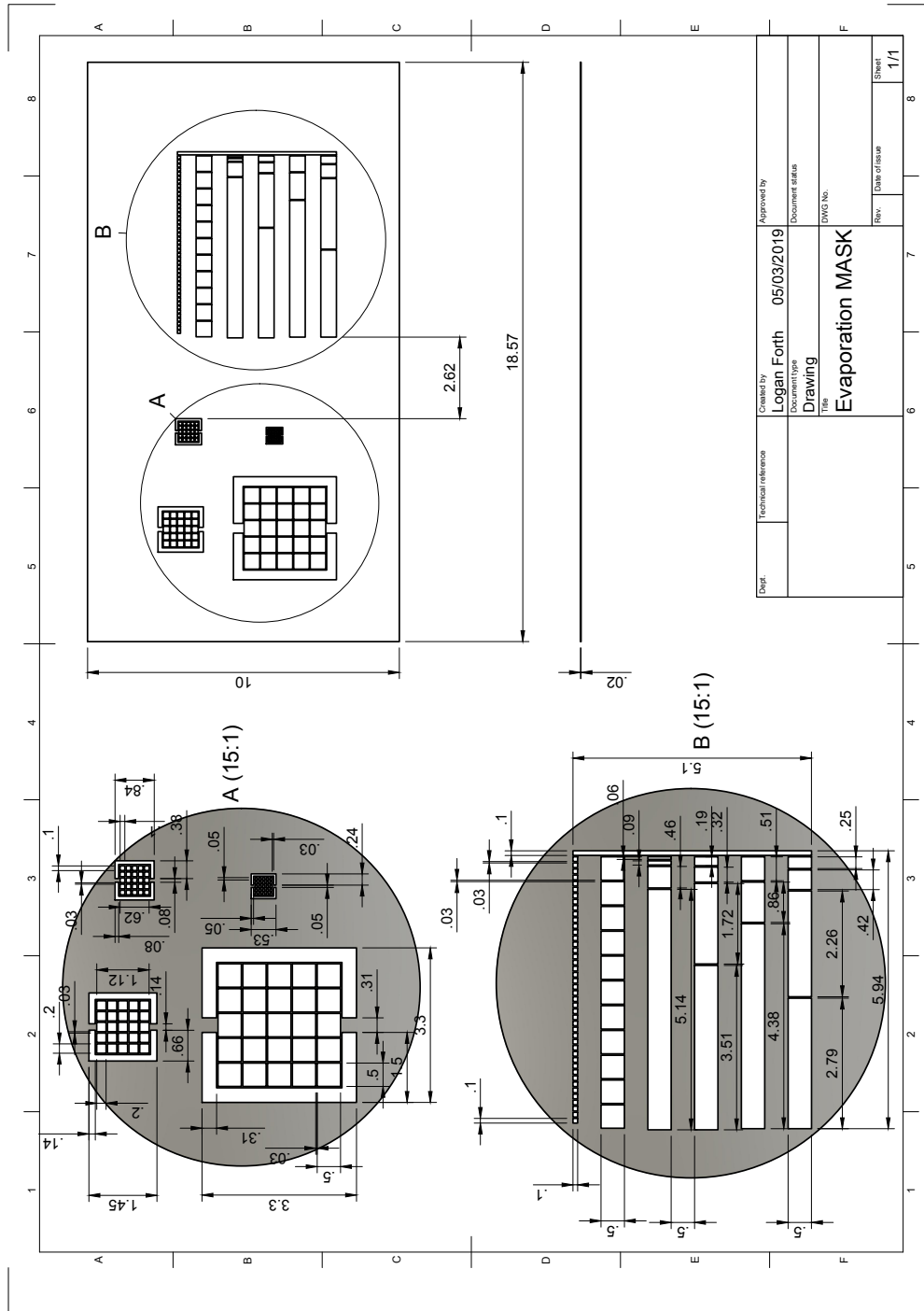
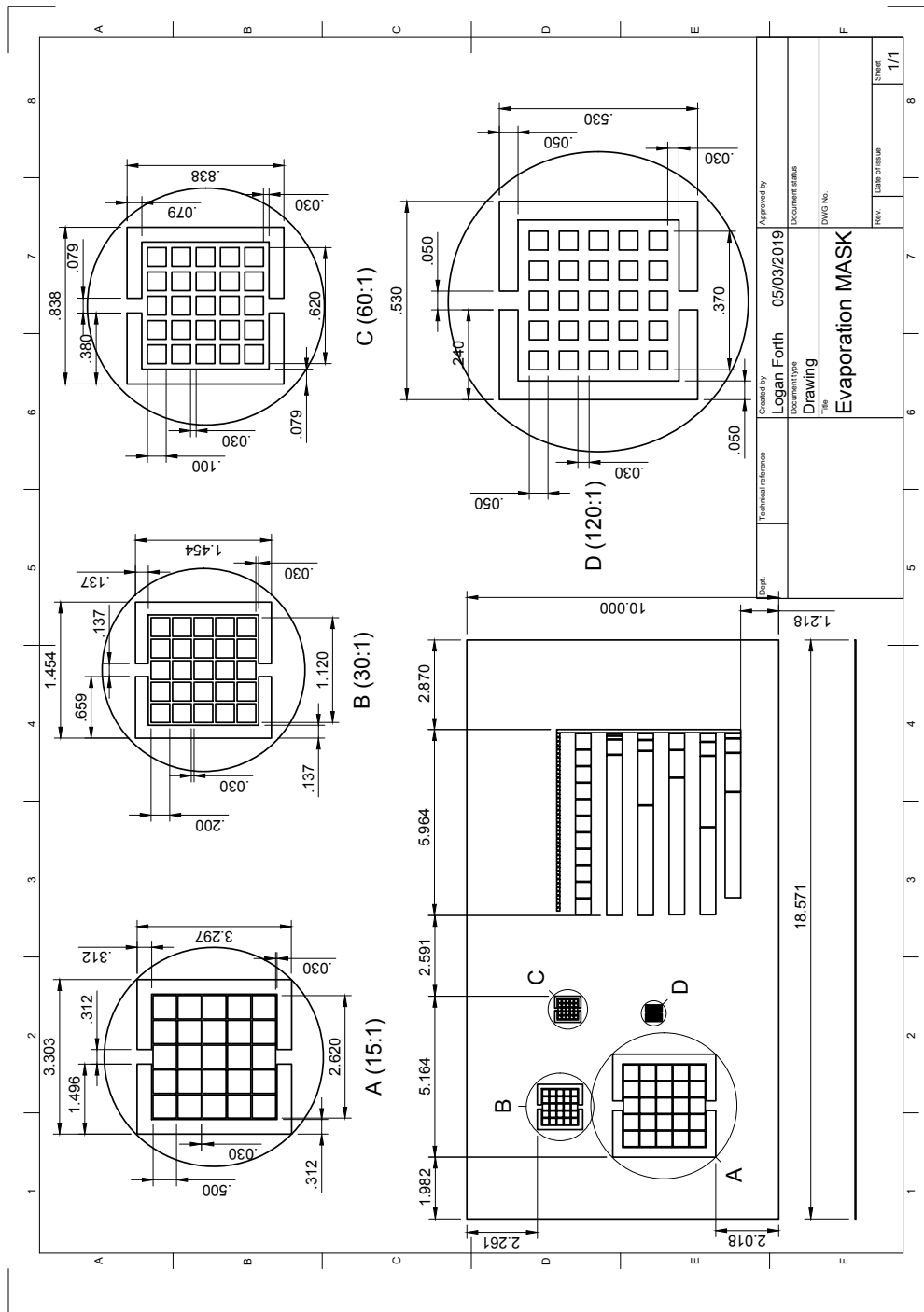**Figure 8.1:** The engineering drawing for the overview of the mask

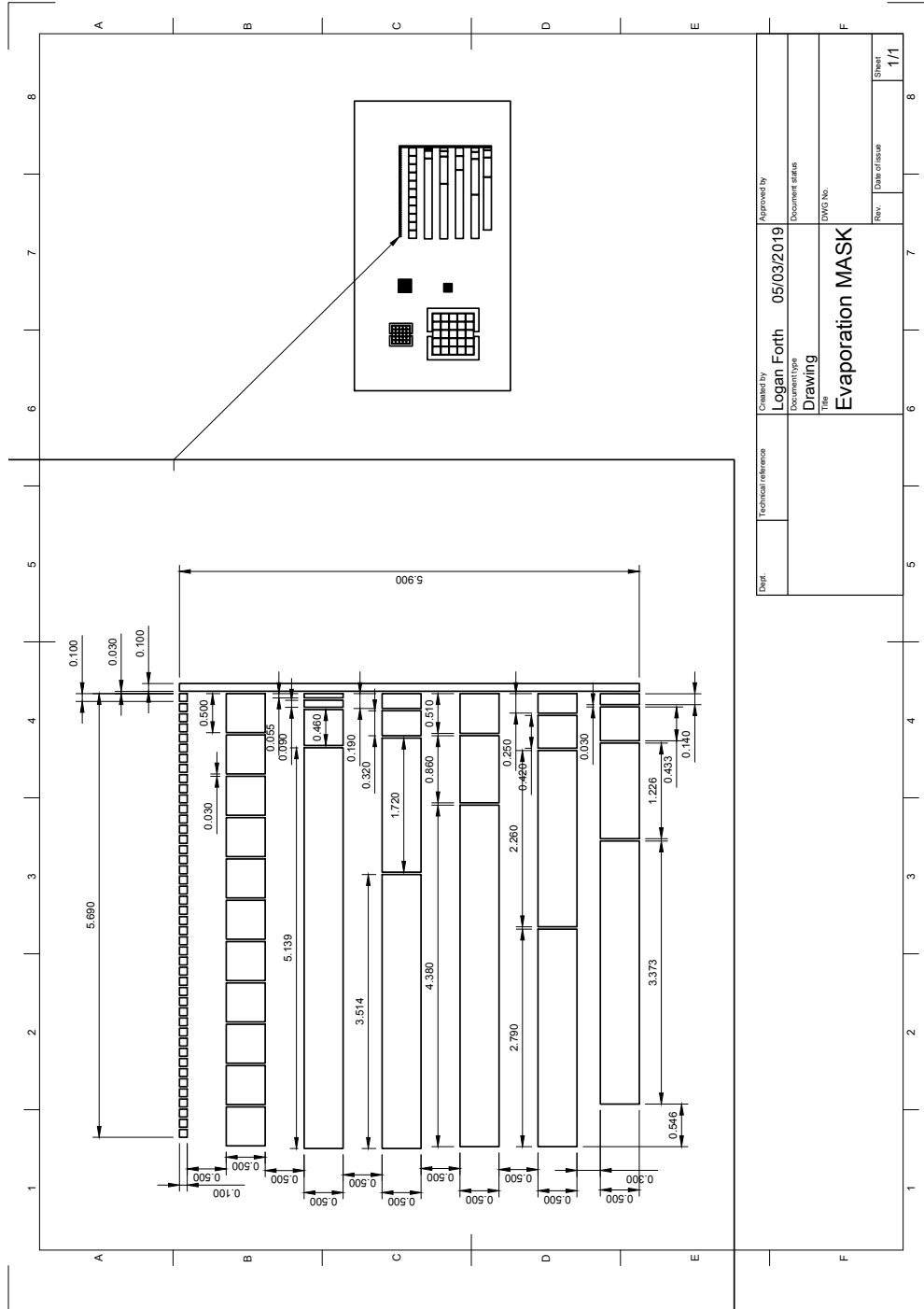**Figure 8.2:** Engineering drawing of the left pixel mask

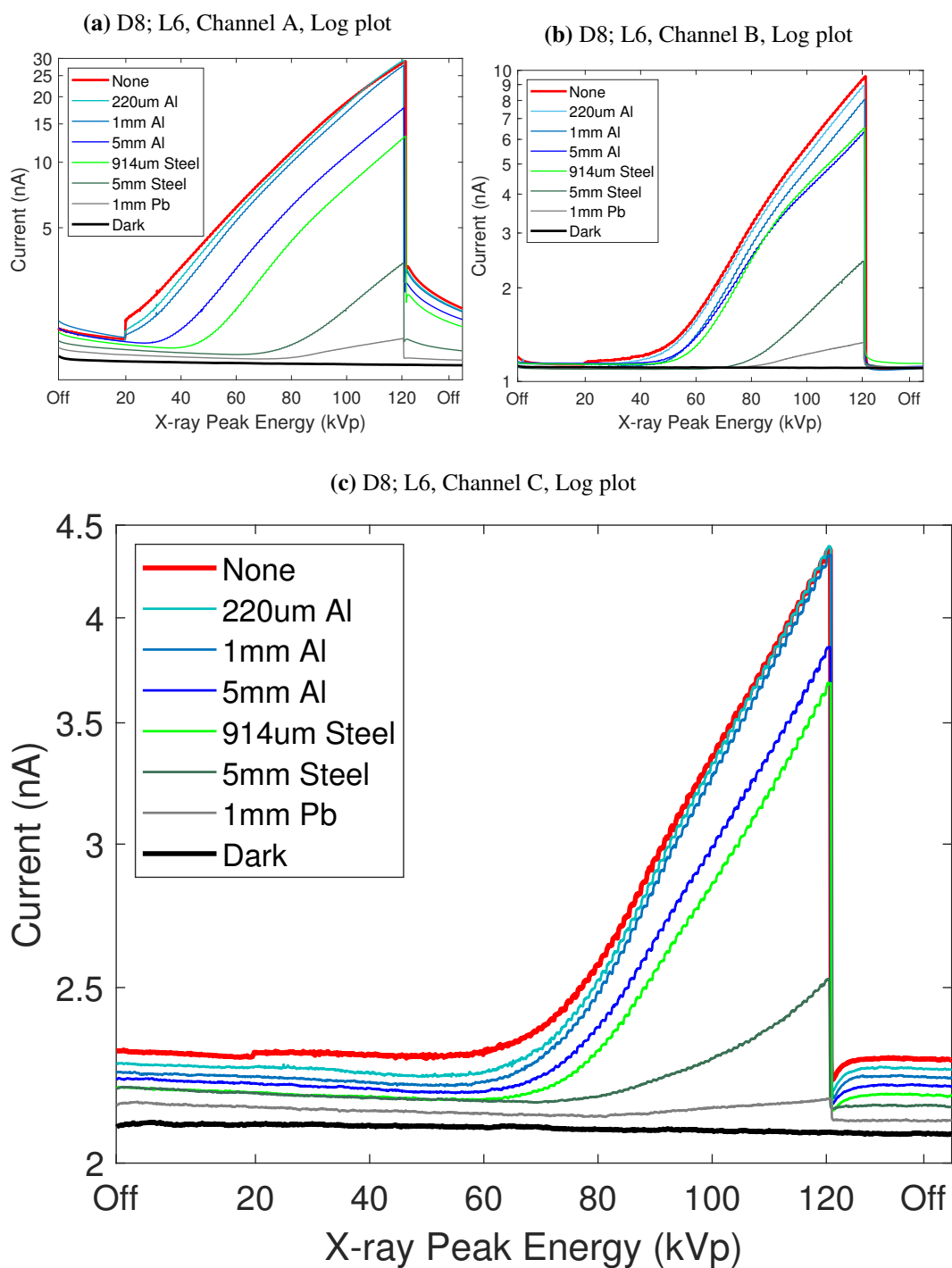**Figure 8.3:** Engineering drawing of the right channel mask

(a) D8; L6, Channel A, Log plot

(b) D8; L6, Channel B, Log plot

(c) D8; L6, Channel C, Log plot

Figure 8.4: Logarithmic plot of the graphs figs. 6.22d to 6.22f